Membrane Fouling During Hollow Fiber Ultrafiltration of Protein Solutions: Computational Fluid Modeling and Physicochemical Properties

by

Amin Reza Rajabzadeh

A thesis
presented to the University of Waterloo
in fulfillment of the thesis requirement for the degree of
Doctor of Philosophy
in
Chemical Engineering

Waterloo, Ontario, Canada, 2010

I hereby declare that I am the sole author of this thesis. This is a true copy of the thesis, including any required final revisions, as accepted by my examiners.

I understand that my thesis may be made electronically available to the public.

Abstract

Hollow fiber ultrafiltration is a viable low cost alternative technology for the concentration or separation of protein solutions. However, membrane fouling and solute build up in the vicinity of the membrane surface decrease the performance of the process by lowering the permeate flux. Major efforts have been devoted to study membrane fouling and design more efficient ultrafiltration membrane systems. The complexity of membrane fouling, however, has limited the progress to better understand and predict the occurrence of fouling. This work was motivated by the desire to develop a microscopic Computational Fluid Dynamics (CFD) model to capture the complexity of the membrane fouling during hollow fiber ultrafiltration of protein solutions.

A CFD model was developed to investigate the transient permeate flux and protein concentration and the spatial fouling behavior during the concentration of electroacidified (pH 6) and non-electroacidified (pH 9) soy protein extracts by membrane ultrafiltration. Electroacidification of the soy protein to pH 6 was found to decrease the permeate flux during UF which resulted in longer filtration time. Lower electrostatic repulsion forces between the proteins at pH 6 (near the protein isoelectric point) resulted in a tighter protein accumulation on the membrane surface suggested to be responsible for the lower permeate flux observed in the UF of the electroacidified soy protein extract. A new transient two-component fouling resistance model based on the local pressure difference, permeate velocity and protein concentration was implemented in the resistance-in-series flux model to describe the dynamics of the reversible and irreversible fouling during the filtration and the effect of pH on the membrane fouling. Good agreement between the experimental data and the model predictions was observed.

Mathematical modeling was performed to estimate the osmotic pressure and diffusion coefficient of the proteins bovine serum albumin (BSA) and soy glycinin, one of the major storage proteins in soy, as a function of protein concentration, pH, and ionic strength. Osmotic pressure and diffusion coefficient of proteins play vital roles in membrane filtration processes because they control the distribution of particles in the vicinity of the membrane surface, often influencing the permeation rate. Therefore, understanding the behavior of these properties is of great importance in addressing questions about membrane fouling. An artificial neural network was developed to

analyze the estimated data in order to find a simple relation for osmotic pressure as a function of protein concentration, pH, and ionic strength. For both proteins, the osmotic pressure increased as pH diverged from the protein isoelectric point. Increasing the ionic strength, however, reversed the effect by shielding charges and thereby decreasing the osmotic pressure. Osmotic pressure of glycinin was found lower than that of BSA. Depending on how much pH was far from the isoelectric point of the protein, osmotic pressure of BSA could be up to three times more than the glycinin's. Two different trends for diffusion coefficient at specified pH and ionic strength were observed for both proteins; diffusion coefficient values that decreased with protein concentration and diffusion coefficient values that passed through a maximum.

A rigorous CFD model based on a description of protein interactions was developed to predict membrane fouling during ultrafiltration of BSA. BSA UF was performed in a total recycle operation mode in order to maintain a constant feed concentration. To establish a more comprehensive model and thereby alleviate the shortcomings of previous filtration models in literature, this model considered three major phenomena causing the permeate flux decline during BSA ultrafiltration: osmotic pressure, concentration polarization, and protein adsorption on the membrane surface. A novel mathematical approach was introduced to predict the concentration polarization resistance on the membrane. The resistance was estimated based on the concentration and thickness profile of the polarization layer on the membrane obtained from the solution of the equation of motion and continuity equation at a previous time step. Permeate flux was updated at each time step according to the osmotic pressure, concentration polarization resistance, and protein adsorption resistance. This model had the ability to show how microscopic phenomena such as protein interactions can affect the macroscopic behaviors such as permeate flux and provided detailed information about the local characteristics on the membrane. The model estimation was finally validated against experimental permeate flux data and good agreement was observed.

Acknowledgments

I would like to express my deep gratitude and appreciation to my supervisors, Professor Christine Moresoli and Professor Bernard Marcos, for their valuable guidance, support and encouragement in my academic life.

I would also like to thank Professor Luc Fillaudeau, Professor Gordon Stubley, Professor Xianshe Feng, and Professor Marios Ioannidis for serving as my committee members and for providing me with constructive comments for this thesis.

My warmest thank you goes to all the people from my lab, Sarah, Rachel, Kela, Sonja, Jana, Seungmi, Rmila, Yasaman, Rand, Jamie, and Mary, my friends, Nima, Mousa, Elahe, Mohammad Reza, Navid, Pouria, Emeline, Atena, Omid Reza, Sohrab, Samira, Saloumeh, Majid, Bahram, Mazda, Bahador, Keyvan, Hamid, Iman, Saeid, and colleagues for their advice, comments and moral support.

I appreciate the National Sciences and Engineering Research of Canada for the financial support and Agriculture and Agri-Food Canada for providing me the soy protein extracts.

Last, but not least, I would like to express my deepest gratitude and love to my family for their love and constant encouragement throughout my life.

Table of Contents

List of Figures

List of Tables

Nomenclature

a	effective hard sphere protein radius (m)
a_{dry}	dry protein radius (m)
a_{Hyd}	protein hydrodynamic radius (m)
A_h	effective area occupied by protein at hypothetical plane (m^2)
ANN	artificial neural network
B_1	first virial coefficient ($Pa.m^3.kg^{-1}$)
B_2	second virial coefficient ($Pa.(m^3.kg^{-1})^2$)
B_3	third virial coefficient ($Pa.(m^3.kg^{-1})^3$)
C	protein concentration (kg. m^{-3})
C_b	bulk concentration (kg. m^{-3})
C_F	feed tank protein concentration (kg. m^{-3})
C_g	gel concentration (kg. m^{-3})
C_w	protein concentration at membrane surface (kg. m^{-3})
d	distance to OHP (m)
d_p	mean pore diameter (m)
D	diffusion coefficient ($m^2.s^{-1}$)
D_1	hydration force constant coefficient (m)
D_2	hydration force constant coefficient (m)
D_B	dilute limit Brownian diffusion coefficient ($m^2.s^{-1}$)
D_p	interparticle distance (m)
e	elementary charge (1.6×10^{-19} C)
F_1	hydration force constant coefficient ($J.m^{-2}$)
F_2	hydration force constant coefficient ($J.m^{-2}$)
F_{ATT}	attraction force (N)
F_{ELEC}	electrostatic force (N)
F_{HYD}	hydration force (N)
G	Gibbs free energy (J)
H	Hamaker constant (J)
H^+	hydrogen ion
K	Boltzmann constant (1.38×10^{-23} J .K^{-1})
K_D	hydrodynamic hindrance factor
K_L	mass transfer coefficient ($m.s^{-1}$)
k_{ad}	adsorption adjustable parameter ($m^2.kg^{-1}$)
k_R	reversible constant coefficient ($kg.s.m^{-2}$)

k_I irreversible constant coefficient (kg.s.m^{-3})

$k(\phi)$ hydrodynamic interaction coefficient

L fiber length (m)

M_w molecular weight (g.mol^{-1})

n number of fibers in the ultrafiltration module

n_i molar concentration of component i (mol.m^{-3})

n^0 ion number concentration in bulk (m^{-3})

N_A Avogadro number (6.02×10^{23} mol^{-1})

OHP outer Helmholtz plane

P pressure (Pa)

P_{in} inlet pressure (Pa)

P_{atm} atmospheric pressure (Pa)

P_{ENT} entropy pressure (Pa)

P_{out} outlet pressure (Pa)

pI isoelectric point

ΔP local trans-membrane pressure (Pa)

Q_F feed tank volumetric rate (m^3.s^{-1})

Q_{hf} outlet hollow fiber volumetric rate (m^3.s^{-1})

Q_{per} permeate volumetric rate (m^3.s^{-1})

r radial coordinate (m)

r_{cell} radius of a volume equivalent sphere for a hexagon (m)

R fiber radius (m)

R^0 gas constant (J.mol^{-1}.k^{-1})

R_c cake layer resistance (m^{-1})

R_{cp} concentration polarization resistance (m^{-1})

R_{ad} resistance due to protein adsorption (m^{-1})

R_G global resistance (m^{-1})

R_i individual resistance component (m^{-1})

R_I irreversible resistance (m^{-1})

$R_{I\,initial}$ initial irreversible resistance (m^{-1})

$R_{I\,ss}$ steady state irreversible resistance (m^{-1})

R_m clean membrane resistance (m^{-1})

R_R reversible resistance (m^{-1})

$R_{R\,initial}$ initial reversible resistance (m^{-1})

S entropy energy (J.K^{-1})

S_β outer cell surface (m^2)

$S(\phi)$ osmotic compressibility factor

t	time (s)
T	temperature (293 K)
TMP	average trans-membrane pressure (Pa)
V	volume (m^3)
V_A	van der Waals energy (J)
VCR	volume concentration ratio
V_F	feed tank volume (m^3)
V_{per}	permeate volumetric rate ($m^3.s^{-1}$)
v_r	radial velocity ($m.s^{-1}$)
v_w	permeate velocity ($m.s^{-1}$)
v_z	axial velocity ($m.s^{-1}$)
$v_{z,max}$	maximum axial velocity ($m.s^{-1}$)
v	specific volume of pure protein ($m^3.kg^{-1}$)
$\overline{v_1}$	specific volume of solvent (water) ($m^3.kg^{-1}$)
$\overline{v_2}$	specific volume of protein solution ($m^3.kg^{-1}$)
v_h	molecular volume of dehydrated protein (m^3)
x	spatial coordinate (m)
X	dependant variable in entropy equation
Δx	length of pores (m)
Y	dependant variable in entropy equation
z	axial coordinate (m)
Z	Valency of NaCl
Z_{AB}	number of surface charge from ionization of amino acids
Z_T	total number of surface charge
Z^+	positive charge
Z^-	negative charge
α	specific resistance (m^{-2})
α^0	viscosity model constant ($m^3.kg^{-1}$)
β	initial reversible fouling model constant (m^{-1})
λ	initial reversible fouling model constant (Pa^{-1})
μ	viscosity of the solution (Pa.s)
μ^0	viscosity of water (Pa.s)
$\hat{\mu}_i$	chemical potential of component i ($J.mol^{-1}$)
ρ	density of water ($kg.m^{-3}$)
ε	porosity
ε_m	surface porosity of membrane
ε_0	vacuum permittivity (8.854×10^{-12} $C.V^{-1}.m^{-1}$)

ε_{r3} relative dielectric constant of water (80)

π osmotic pressure (Pa)

ϕ volume fraction

δ thickness of concentration boundary layer (m)

δ_1 grams of bound water per gram of protein

τ_I irreversible apparent time constant (s)

σ_0 surface charge density ($C.m^{-2}$)

σ_d charge density at OHP($C.m^{-2}$)

ψ electrostatic potential (V)

ψ_0 electrostatic potential at protein surface (V)

ψ_d electrostatic potential at OHP (V)

Chapter1

Introduction

1.1 Research motivation and objectives

Ultrafiltration membrane technology is widely used in various chemical and biochemical processes. The process is effective for protein concentration and purification and for the separation of the bioproducts. The characteristics of ultrafiltration process include cost effectiveness and minimized physical damage and denaturation of biomolecules. The efficiency of the process, however, decreases during the filtration due to the solute build-up and solute adsorption on the membrane surface and inside the membrane pores, the extent of which is controlled by the hydrodynamic parameters and the physicochemical properties of the solution and the membrane.

The overall impetus for this work arose from the needs to understand the insights on the mechanisms of membrane fouling during the ultrafiltration of protein solutions. A rigorous model was needed to cover the complexity of the process, and hence to provide a comprehensive description about the membrane fouling and permeate flux decline during the ultrafiltration. Computational Fluid Dynamics (CFD) is an attractive tool for this purpose that provides spatial and transient information about the fouling behavior during the filtration process.

The objectives of this work were to:

A) Investigate the effects of electroacidification pretreatment of soy protein extract and hydrodynamic parameters on the membrane fouling during a hollow fiber ultrafiltration process: CFD model development and experimental validation.
B) Develop a multi-scale model in order to quantify the effects of ionic strength, pH, and protein concentration on the transport properties, such as diffusion coefficient and the thermodynamic properties, such as osmotic pressure of the protein.

C) Investigate the effects of pH, ionic strength, and hydrodynamic parameters on the permeate flux during a hollow fiber ultrafiltration process: development of a rigorous microscopic CFD model based on a description of protein interactions and experimental validation

1.2 Thesis organization

This thesis consists of three main chapters proceeded by an introduction (chapter 1) and background information (chapter 2) and followed by principle outcomes and recommendations of the work (chapter 6).

Chapter 2 provides brief background information about ultrafiltration, membrane fouling, permeate flux models, characteristics of proteins, Computational Fluid Dynamics, and DLVO theory. In Chapter 3, concentration process of electroacidified and non-electroacidified soy protein extract in a hollow fiber ultrafiltration system is described. This chapter discusses the development of a CFD model to predict the effect of electroacidification pretreatment of soy protein extracts as well as the hydrodynamic parameters on the membrane fouling and the permeate flux. Introduction sections in Chapters 3-5 compliment the background information in Chapter 2. Multi-scale modeling of osmotic pressure and diffusion coefficient of protein solutions is discussed in detail in Chapter 4. Effects of protein concentration, pH, and ionic strength on the diffusion coefficient and the osmotic pressure of BSA and soy glycinin are investigated. This chapter also describes the development of an Artificial Neural Network (ANN) to relate the osmotic pressure of the protein to the pertinent parameters. Chapter 5 investigates the hollow fiber ultrafiltration of BSA in a total recycle operation mode. This chapter describes the theoretical development of the multi-scale CFD model and the experimental verifications. Principle outcomes of this work and future works are summarized in Chapter 6.

Chapter 2

Background

2.1 Soy proteins

Soy bean with roughly 40% protein (dry basis) is considered to be a great source of non-animal protein which contains significant amount of essential amino acids needed for human body. Based on the protein content, soy proteins are categorized as soy flour (60% protein), soy protein extracts (70% protein), and soy protein isolates (90%). Soy protein isolate is widely used as functional or nutritional ingredient in a wide variety of food products, mainly in baked foods, breakfast cereals, noodles, soups and in some meat products. Soy protein isolate is sold in the health food section or the pharmacy within regular supermarkets. Soy protein isolate can be purchased as flavored or plain soy protein shake powder. Soy food market has significantly increased during the last 10 years. US soy food market for example increased by 29% from 1999 to 2001 [1]. Per capita soy protein consumption in Canada and the U.S. in 2001 was reported 0.68g/day and 0.32g/day, respectively; the world average was reported 2.36 g/day. It is predicted that per capita soy protein consumption in Canada increases from 0.68g/day at 2001 to 3g/day at 2020. If per capita protein consumption is translated into demand for soybean assuming 40% protein as basis, around 20,000 MT and 30,000 MT soybeans are required in Canada and US, respectively. The total market value of this opportunity is $1.7M and $2.5M for Canada and US. [1].

Soy protein isolates (SPI) is traditionally prepared from defatted soy flakes through a series of steps including aqueous extractions, centrifugation, isoelectric precipitation, washing, neutralization, and drying. A disadvantage of the traditional method is the protein denaturation that results in poor protein solubility and poor functional properties of the final product. An alternative for the production of SPI is a membrane ultrafiltration process. Membrane ultrafiltration is a mild process that produces SPI with improved solubility and functional properties [2,3]. An alternative process to produce SPI with a low amount of minerals is the combination of electroacidification and membrane ultrafiltration. Electroacidification pretreatment of the soy protein, a mild pH adjustment method, enhances the mineral removal of the soy protein extracts during the ultrafiltration [4,5]. However, at the same time, the ultrafiltration permeate flux decreases drastically due to the membrane fouling and protein deposition on the membrane. Figure 2.11 depicts the production process of the soy protein isolates from defatted soy flakes.

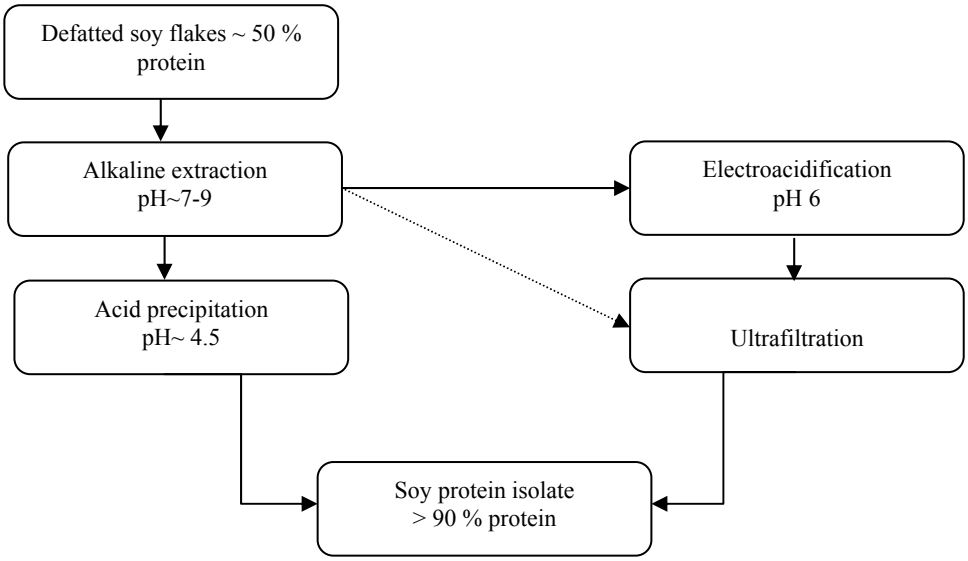

Figure 2.1 Production process of soy protein isolate

2.2 Membrane ultrafiltration

Membrane ultrafiltration is a pressure driven operation, the pressure provides a driving potential to force the solvent to permeate through the membrane. Ultrafiltration membrane is typically rated by the membrane pore size or by molecular weight cutoff, a convenient value giving the molecular weight of a hypothetical solute that the membrane will just retain (Table 2.1) [6]. Some of the major applications of membrane ultrafiltration in biotechnology are purification of proteins and nucleic acids, concentration of macromolecules, desalting, and virus removal from therapeutic products [6].

Ultrafiltration membranes can be operated in a dead-end or a cross-flow mode (Figure 2.2). Dead-end system is used only for small-scale and laboratory applications. Most medium and large scale filtration processes are carried out in the cross-flow mode. The main advantage of the cross-flow operation is the minimization of the accumulation of solutes near the membrane surface. The cross-flow arrangement also facilitates recirculation of retentate stream to the feed tank followed by its mixing with fresh feed. The most common cross-flow modules are flat sheet tangential flow, tubular membrane, spiral wound membrane, and hollow fiber. The hollow fiber membrane module is a cost effective and highly practical cross-flow module. The hollow fiber module allows a high membrane surface area to volume ratio. The module usually consists of a

bundle of fibers with a diameter range of 0.25 to 2.5 mm which can be set up either in a U-shape or in a straight-through configuration. Hollow fiber membranes are typically made of polymers therefore they cannot be used for corrosive substances or at high temperature operating condition. A simplified sketch of a hollow fiber module is illustrated in Figure 2.3.

Table 2.1 Characteristics of membrane processes [7]

Process	MWCO/Pore size	Retentate	Permeate
Conventional filtration	>10μm	Large particles	Small/suspended particles, water
Microfiltration (MF)	0.1 to 10 μm	Suspended particles	Dissolved solutes, water
Ultrafiltration (UF)	0.005 to 0.1 μm	Large molecules	Small molecules, water
Nanofiltration (NF)	0.0005 to 0.005 μm	Small molecules, divalent salts, dissociated acids	Monovalent ions, undissociated acids, water
Reverse osmosis (RO)	<0.5 nm 50 to 200 Daltons	All solutes	Water

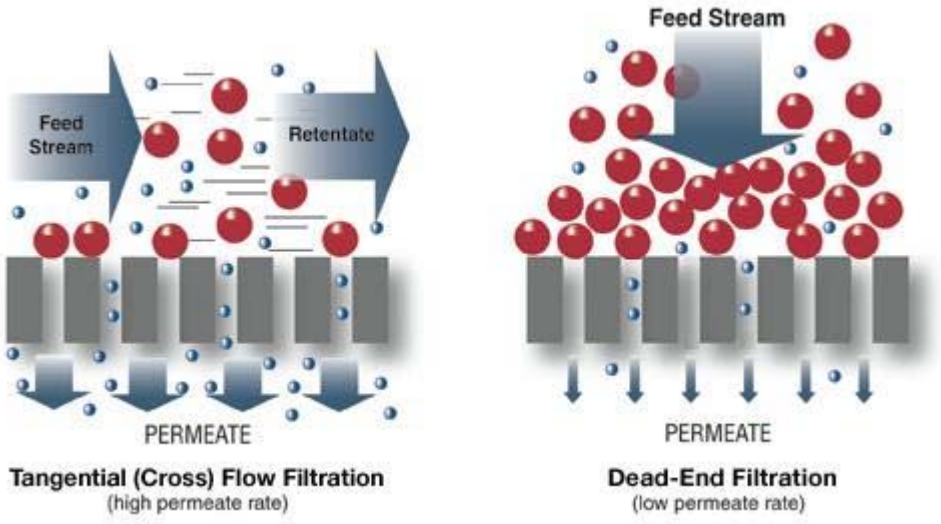

Figure 2.2 Schematic diagrams of the cross-flow mode (left) and the dead-end mode (right) (adapted from [8])

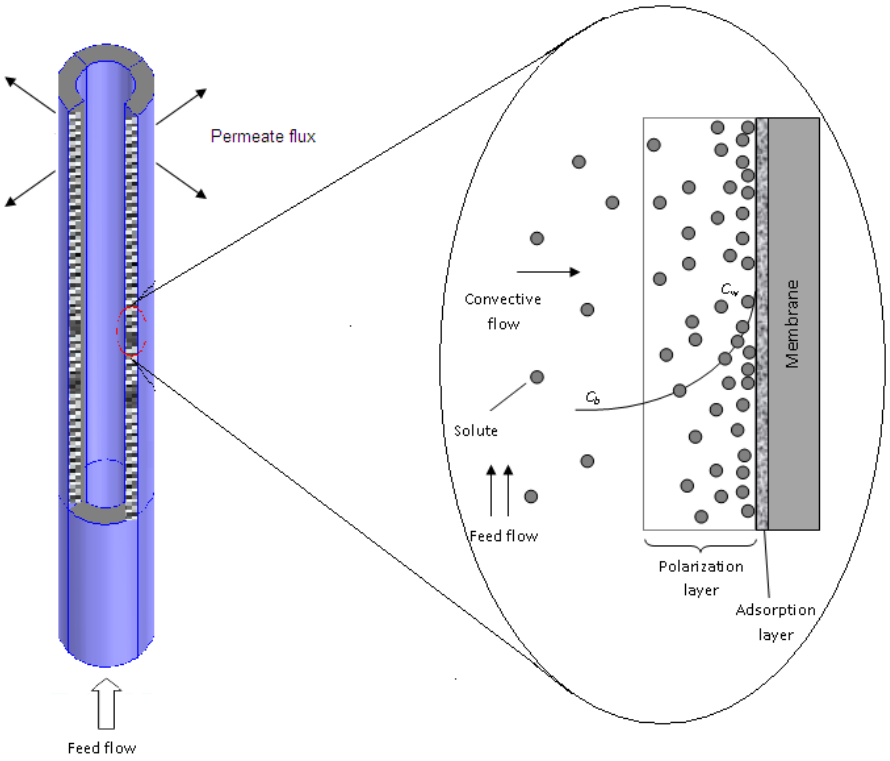

Figure 2.3 Schematic cross section of a hollow fiber membrane [8]

2.3 Membrane fouling

Fouling is a process caused by the deposition of suspended or dissolved solutes on the membrane surface, on the membrane pores, or within the membrane pores resulting in a decrease in the performance of the membrane. There are four mechanistic models typically used to describe the membrane fouling; complete blocking, standard blocking, intermediate blocking, and cake (Figure 2.4) [9]. Complete blocking assumes that particles seal off pore entrances and prevent flow. Standard blocking assumes that particles accumulate inside the membranes pores. Intermediate blocking is similar to complete blocking but assumes that a portion of the particles block the pores and the rest accumulate on top of other deposited particles. Cake occurs when particles accumulate on the top of the membrane surface [7,9-11]. The nature and extent of membrane fouling depends on the physico-chemical nature of the membrane and the solution as well as the operating conditions. Membrane fouling can also be categorized as concentration polarization, gel (cake) layer, and membrane adsorption.

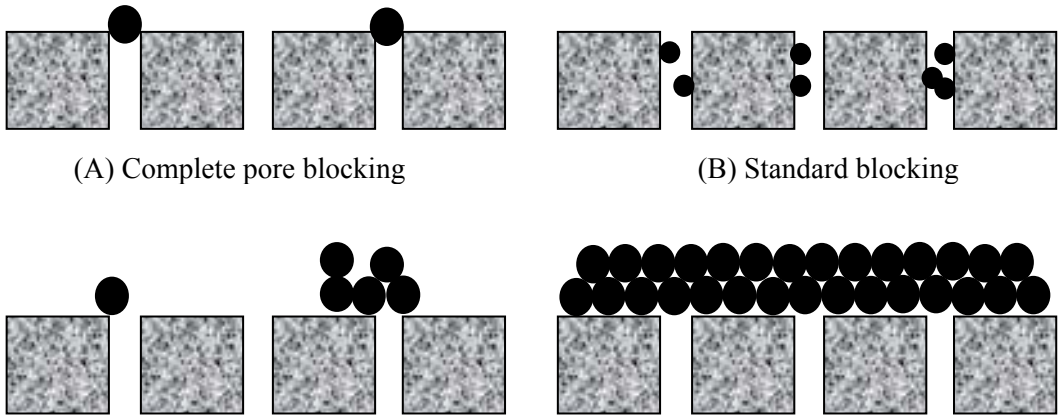

Figure 2.4 Schematic drawing of the fouling mechanisms, adapted from [12]

2.3.1 Concentration polarization and gel layer

Concentration polarization layer is the primary reason for the permeate flux decline at the beginning of any filtration operation [13]. Concentration polarization is a result of solutes brought to the membrane by convective flux and their back transport to the bulk by diffusion. The thickness and the concentration profile of the concentration polarization layer are controlled by the magnitude of the convection and the diffusion terms. Depending on the type of solute, concentration polarization layer could be viscous and gelatinous which results in a further resistance to the permeate flux, in addition to that of the membrane itself. As was described in detail by Bacchin et al. [14], a gel layer formed when the solute concentration in the polarization layer reached a critical value. Both the concentration polarization layer and the gel layer when presents were considered as the reversible membrane fouling [15].

2.3.2 Membrane adsorption

Another reason for the permeate flux decline during the filtration process is solute adsorption on the membrane surface or inside the membrane pores. A clear distinction between concentration polarization resistance and solute adsorption resistance is that the former is governed predominantly by solute-solute interactions while the latter depends mainly on solute-membrane interactions.

According to Howell and Le [16] protein adsorption is formed in a monolayer followed by further protein deposition due to hydrophobic interaction and intermolecular disulphide bonding. The monolayer adsorption is usually represented by Langmuir or Freundlich equations [15]. The equations describe the amount of solutes statically adsorbed on the membrane surface or inside the membrane pores as a function of bulk concentration.

2.4 Models for flux prediction

Like other processes, modeling of membrane separation processes requires quantitative expressions to relate solution properties and model hydrodynamic to the separation performance. Different models have been proposed to describe the permeate flux through the membranes: pore flow model, mass transfer model (film theory), shear induced model, osmotic pressure model, and resistance-in-series model [7,17].

2.4.1 Pore flow model

Hagen-Poiseuille equation (equation 2.1) is generally used to estimate the permeate flux through the membrane pores with uniform radius perpendicular to the face of the membrane. Several assumptions such as laminar flow in the pores, constant density, steady-state condition, and Newtonian fluid have been made in deriving equation 2.1. Neither the concentration polarization nor the solute adsorption on the membrane was considered in this model.

$$v_w = \frac{\varepsilon_m d_p^2 \Delta P}{32 \Delta x \mu} \tag{2.1}$$

where v_w is the permeate flux; d_p is the mean pore diameter; ΔP is the applied trans-membrane pressure (TMP); μ is the viscosity of the fluid permeating through the membrane; Δx is the length of the pore (membrane thickness); ε_m is the surface porosity of the membrane.

2.4.2 Film theory

One of the widely used theories for modeling the membrane permeate flux is the film theory. During membrane filtration (Figure 2.5), the convection flux of the solute normal to the membrane is balanced by the back diffusion (equation 2.2).

$$v_w C = D\frac{dC}{dx} \tag{2.2a}$$

where C and D are the solute concentration and diffusion coefficient, respectively. At steady state, equation 2.2 can be integrated over the boundary layer (δ) (Figure 2.5) to give

$$v_w = \frac{D}{\delta}\ln\left(\frac{C_g}{C_b}\right) = K_L \ln\left(\frac{C_g}{C_b}\right) \tag{2.2b}$$

where K_L is the mass transfer coefficient , C_b is the solute bulk concentration , and C_g is the gel concentration, i.e., the concentration at which the solute loses its solubility in the solution. Since no pressure dependent term is introduced in the film theory model, this model is valid only in the pressure independent region [7]. The model also assumes that the diffusion coefficient of the solute is concentration independent. Literature indicates that equation 2.2b underpredicts the experimental permeate flux, sometimes by several orders of magnitude [7,18,19]. The discrepancy between the predicted and experimental flux named as the flux paradox is most noticeable with colloidal feed solutions at high transmembrane pressures and low axial velocities [7]. When the transmembrane pressure is low, the polarized layer is removed with a high shear rate and results in a better prediction of equation 2.2b; the reason of which is not clear yet. The film theory model is a good approximation only when the boundary layer is thin and uniform (turbulent flows). Another reason for predicted permeate flux (equation 2.2b) being lower than the experimental results is that the back diffusion from the membrane surface to the bulk is greater than expected. The back diffusion of the solutes from the membrane surface is controlled by forces other than or in addition to the concentration gradient. At high axial velocity for example, separation of the boundary layer from the membrane surface occurs to form a “wake”.

Therefore, the solute migration to the bulk is controlled by two contributions from the laminar boundary layer and from the wake. This phenomenon is named as tubular pinch effects [7]. As was stated earlier, this phenomenon exists only at high axial velocities (turbulent flow).

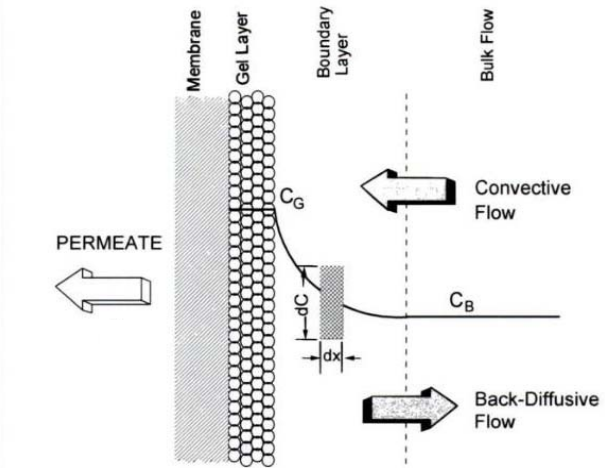

Figure 2.5 Schematic of film theory for the ultrafiltration of colloidal and macromolecular solutes [7]

2.4.3 Shear induced model

Shear induced model has been developed based on the film theory model. At steady state, rate of convection of solute normal to the membrane is balanced by solute back transport in which the back transport is not only due to the Brownian diffusion, but also due to the shear rate gradient. It is worth mentioning here that shear induced diffusion becomes less important as solutes decrease in size [15,20]. Shear induced model is assumed to be independent of interparticle interactions (colloidal forces).

2.4.4 Darcy model

Darcy model is a simple proportional relation between the permeate flux, the trans-membrane pressure, the fluid viscosity, and resistance of the membrane; the reciprocal resistance is also known as the permeability. This model assumes that membrane is the only resistance to the permeate flux and no fouling occurs during the filtration.

$$v_w = \frac{\Delta P}{\mu R_m} \tag{2.3}$$

2.4.5 Osmotic pressure model

Osmotic pressure is a key parameter in membrane filtration processes. Osmotic pressure arises when two solutions of different concentrations are separated by a semi-permeable membrane. During protein ultrafiltration process for example, permeable solvent passes through the membrane because of the trans-membrane pressure resulting in a solution with higher concentration of protein on the feed side of the membrane than that of the permeate side. Permeable solvent tends to migrate back from the permeate side to the feed side of the membrane due to the chemical potential difference. The pressure required to oppose the back migration of the solvent is known as the osmotic pressure [17]. Therefore, TMP confronts a back pressure, osmotic pressure, during the filtration which lowers the efficiency of the filtration process. In the osmotic pressure model, it is assumed that the decrease in permeate flux is due to an increase in the osmotic pressure.

$$v_w = \frac{\Delta P - \pi}{\mu R_m} \tag{2.4}$$

where R_m and π are the membrane's intrinsic resistance and the osmotic pressure, respectively. Osmotic pressure depends on the physicochemical properties of the solute affected by pH and ionic strength of the solution. Bowen et al. developed a method to calculate the osmotic pressure of colloidal dispersion considering particle-particle interactions (see chapter 4 for detail) [21-25]. Extensive studies have been performed to model the permeate flux during the filtration process applying the osmotic pressure model [26-29].

2.4.6 Resistance-in-series model

According to the resistance-in-series model (equation 2.5), the permeate flux decline is due to the combination of various resistances, e.g., resistance of the membrane (R_m), resistance of the concentration polarization layer (R_{cp}), resistance of the cake layer (R_c), and resistance of the adsorption layer (R_{ad}). A number of studies have been performed using the resistance-in-series

model to estimate the permeate flux during the ultrafiltration process confirming the suitability of the model when osmotic pressure is negligible [30-33].

$$v_w = \frac{\Delta P}{\mu \sum R_i} = \frac{\Delta P}{\mu\left(R_m + R_{cp} + R_c + R_{ad}\right)} \tag{2.5}$$

2.5 Deryaguin-Landau-Verwey-Overbeek (DLVO) theory

Charged particles in a solution are surrounded by ions of opposite charge. The acquisition of the surface charge by the particles affects the distribution of the ions in solution. The arrangement of the electric charges on the particles together with the balancing charge in the solution is known as the electrical double layer (EDL). The electrical double layer of particles starts to overlap when particles approach one another. As a result, a repulsive force is formed between the particles which acts as an energy barrier, preventing the particles from agglomeration. If the electrostatic repulsive forces are weak (e.g., due to low surface charge) compared to the kinetic energy of the colliding particles, the particles agglomerates due to van der Waals attractive forces.

DLVO theory is an effective framework to describe the stability of the colloidal dispersions based on the calculation of the total interaction energy between colloid particles. The classical DLVO model is based on the interactions due to overlapping of electrical double layers and London-van der Waals forces. The model considers a linear combination of London-van der Waals attractive and electrostatic repulsive repulsion energies. The theory estimates the interaction energy as a function of distance separating particles (D_p) [34]. It was observed that the classical DLVO theory fails to accurately describe colloidal interaction between particles. Therefore, the classical model was later extended by including the contribution of other interactions such as hydration forces, named extended DLVO theory [35].

$$V_T(D_p) = V_{ATT}(D_p) + V_{ELEC}(D_p) + V_{HYD}(D_p) \tag{2.6}$$

V_T, V_{ATT}, V_{ELEC}, and V_{HYD} stand for the total, London-van der Waals, electrostatic and hydration energies as a function of distance separating the particles (D_p). Electrostatic repulsion energy, V_{ELEC}, between particles is calculated considering the neighboring particles using a Wigner and Seitz cell model and will be discussed in detail in chapter 4[22]. Hamaker [36] introduced a simple procedure for calculating these attractive forces considering quantum mechanics. According to quantum mechanics, London-van der Waals energy between any two atoms is proportional to $\frac{H}{(D_p+2a)^6}$ in which H, is the Hamaker constant dependent on the polarizability of the atoms. The total attraction energy is obtained by considering this attraction energy between an atom and a nearby surface and by integrating this equation over the volume of each atom. The origin of hydration energy, V_{HYD}, is believed to be electron acceptor-electron donor interactions, often referred to as polar interactions. Polar interactions orient water molecules adsorbed on the surface of particles, and thus the stability of the colloidal system is conferred by those hydrated water molecules that force two particles apart at contact. Such polar forces could be comparable to the van der Waals attractive or electrostatic repulsive, energies at close range.

2.6 Computational fluid dynamics (CFD) modeling and membrane filtration

Aqueous protein solutions are well known for their complex physical behavior. The diffusion coefficient of the protein, the viscosity of the solution, and the osmotic pressure depend on the protein concentration, pH and ionic strength of the solution. For this reason and also because the protein concentration changes locally on the membrane surface, simplified models such as film theory model are not sufficient to describe the complexity of the fouling phenomena. Therefore, robust techniques are needed to obtain more applicable models to membrane systems. Computational fluid dynamics (CFD) modeling can provide such a technique and is able to estimate the local concentration and velocity characteristics.

CFD is based on numerically solving the governing equations of fluid dynamics-the continuity, momentum, and energy equations. During membrane filtration without chemical reaction, minimal heat transfer occurs. Therefore, the governing equations reduce to the continuity and momentum equations. CFD modeling is of great interest when analytical solutions are nearly impossible to obtain due to the complexity of the geometry or the physics of the system. CFD

modeling is initiated by defining the geometry (physical bounds) of the problem. The geometry occupied by the fluid is divided into uniform or non uniform discrete cells (mesh). The governing equations and the boundary conditions (specifying the fluid behavior and properties at the boundaries of the problem) are then applied to the geometry. The governing equations are discretized over the discrete cells applying different discretization methods (finite element method, finite volume method and etc). Discritization produces a system of ordinary differential equations (ODE) for unsteady problems and algebraic equations for steady problems. Implicit or semi-implicit methods are generally used to integrate the ODEs producing a set of nonlinear algebraic equations. Iterative or direct methods are then applied to solve these sets of algebraic equations.

During the last decade, a number of studies have illustrated the use of CFD modeling for solving the complete set of continuity and momentum equations for membrane filtration [27,37-41]. The advantages of CFD modeling for the understanding of the filtration process have been presented by Ghidossi et al. [42]. CFD models can provide a rigorous and detailed analysis of the local and transient conditions for the permeate velocity, the solute concentration and the fouling with a reduced number of assumptions. For example, estimates of the transient and local permeate flux and fouling behavior were obtained without requiring assumptions on the polarization layer thickness by Marcos et al. [41]. The conditions at the membrane surface were described by a dynamic resistance-in-series model, based on the experimental permeate flux profile for the concentration of soy protein extracts by cross-flow ultrafiltration [41]. The model, validated with experimental permeate flux and protein concentration data, predicted axial variations of the protein concentration at the membrane surface with a maximum occurring before the end of the filter. The existence and importance of axial variations of the permeate velocity and solute concentration during membrane ultrafiltration of dextran solutions was also reported by Ma et al. [26] using a finite element model for solving the equations of motion and continuity. The permeate velocity at the membrane surface was represented by the osmotic pressure model expressed in terms of dextran concentration. The concentration dependency of the viscosity was also shown to be a critical factor for the prediction of a limiting flux, the pressure independent flux, for the concentration of dextran solutions. The approach proposed by Ma et al. [26] assumes the existence of limiting flux and steady-state conditions. Schausberger et al. [43]

developed a transient finite volume code and solved the mass, momentum and species conservation equations for the cross-flow ultrafiltration of BSA with total BSA retention. The model incorporated detailed osmotic pressure, viscosity and diffusion coefficient representation for BSA. The fouling was described with a modified Darcy's law and a resistance-in-series model with an irreversible surface adsorption fouling reaction. A one adjustable parameter model was developed. Good agreement with the model and experimental data was obtained for the permeate flux and different pH and feed velocity conditions. The agreement was not so good for the effect of protein concentration and the concentration polarization and fouling.

Chapter 3*

Fouling Behavior of Electroacidified Soy Protein Extracts during cross-Flow Ultrafiltration Using Dynamic Reversible-Irreversible Fouling Resistance and CFD Modeling

* Adapted from A.R. Rajabzadeh, C. Moresoli, and B. Marcos. Fouling Behavior of Electroacidified Soy Protein Extracts During Cross-Flow Ultrafiltration Using Dynamic Reversible-Irreversible Fouling Resistances and CFD Modeling. J.Membr.Sci., 361 (2010) 191.

Overview

The transient membrane fouling during the concentration by cross-flow ultrafiltration of soy protein extracts subjected to electroacidification is examined by combining experimentation with Computational Fluid Dynamics (CFD) modeling. Transient reversible (water removal) and irreversible (chemical removal) membrane fouling resistances, permeate flux, and protein concentration were obtained experimentally. A detailed fouling resistance model to describe the reversible and the irreversible fouling resistances was developed in terms of the microscopic local transient and spatial pressure difference, permeate velocity and protein concentration and initial fouling resistance conditions. This fouling resistance model is used in a boundary condition for the permeate velocity when solving the momentum and protein concentration continuity equations with CFD. The model estimates agree with experimentally measured permeate flux, protein concentration and transient irreversible and reversible fouling resistances. In particular, the model estimated accurately the transient reversible and irreversible fouling resistances, a limitation of most previously published models. The model shows considerable axial variation of the reversible fouling resistance and the protein concentration at the membrane surface which supports the inadequacy of the film theory and the assumptions for constant properties. In contrast, the irreversible fouling resistance remains relatively constant with axial position suggesting protein adsorption.

3.1 Introduction

Membrane ultrafiltration (UF) is a pressure driven operation where liquid and solutes smaller than the membrane pores permeate through the membrane while solutes larger than the membrane pores are retained. The accumulation of solutes near the membrane surface or within the membrane pores constitutes membrane fouling. Major efforts have been devoted to study fouling and design more efficient ultrafiltration membrane systems. However, the complexity of fouling has limited the progress to better understand and predict the occurrence of fouling. Modeling studies represent an attractive alternative to obtain information on the contribution of the feed properties and the operating conditions to membrane fouling. In particular, mathematical microscopic methods constitute an attractive approach for the investigation of fouling mechanisms near the membrane surface. These methods are based on numerically solving the equations of motion and continuity with additional relationships describing fouling. Analytical solutions are nearly impossible to obtain due to the complexity of these equations. Some approximated solutions can be used to solve the equation of motion [44,45] and can be combined with a complete numerical solution of the continuity equation. In some cases, the microscopic model considers a spatial or transient fouling model in the boundary condition to determine the local permeate velocity and the convection-diffusion equation for species material balance. For instance, Yeh et al. [30] combined a simplified steady state momentum equation with a resistance-in-series model where the gel layer resistance is proportional to the local trans-membrane pressure to describe dextran ultrafiltration. Tu et al. [46] used simplified partial differential equations for the continuity equation and computed the transient permeate velocity at the wall from a resistance-in-series model representing internal pore fouling, concentration polarization and gel layer mechanisms. The dynamics of the different resistances were represented by ordinary differential equations with power law relationship for the resistances in terms of concentrations and pressure. To describe a hollow-fiber UF configuration, Secchi et al. [31] used the resistance-in-series model as a boundary condition of the continuity equation. The resistance-in-series model consisted of the intrinsic membrane resistance and an adsorption resistance with a Langmuir form for the solutes retained at the membrane surface. When the approximated relations for the equations of motion and continuity are not sufficient, in house or commercial computational fluid dynamics (CFD) codes are required. Extensive studies have

illustrated the use of CFD modeling for solving the complete set of continuity and momentum equations for membrane filtration [27,37-41].

Soy protein ingredients are contained in a wide variety of processed food products. A number of studies describe the advantages of membrane UF for the production of soy protein ingredients with improved protein yields and functional properties [7,47,48]. The membrane pore size is generally selected to enable the removal of carbohydrates and minerals by permeation through the membrane while retaining and concentrating the major soy proteins. Recent work has shown that the combination of electroacidification and UF represents an attractive approach for the concentration of soy protein extracts [4,5,48,49]. The electroacidification of the soy protein extract to pH 6 enhances the magnesium, calcium, and phytic acid removal compared with the non-electroacidified soy protein extract at pH 9. However, electroacidification decreases the permeate flux during UF which results in longer filtration time. The ionic strength and the pH are known to affect the strength and the nature of protein-protein and membrane-protein interactions. Lower electrostatic repulsion forces between the proteins at conditions near their isoelectric point results in a tighter protein accumulation on the membrane surface suggested to be responsible for the lower permeate flux observed in the UF of the electroacidified soy protein extract [4,5,48,49].

The modeling of soy protein UF has generally combined simple macroscopic models and empirical observations to describe fouling and process observations. This approach is unable to provide information on the local behavior of the filtration. Krishna Kumar et al. [47] modeled the permeate flux with the film theory mass transfer model and a resistance-in-series model to compare the performance of tubular and spiral modules for soy protein concentrates in a total recycle mode at steady-state. The total fouling resistance was represented by the sum of a concentration polarization resistance (proportional to the pressure) and a solute membrane interactions resistance. Constant and global resistances were estimated from steady-state filtration data. Furukawa et al. [50] modeled the UF of soy sauce lees considering fouling caused by the cake formation and limited by the hydraulic lift velocity. They rearranged this resistance-in-series model to introduce reversible and irreversible resistances. The reversible resistance is defined to be proportional to permeate volume. The irreversible resistance is assumed to change

from a pure water membrane resistance to the total irreversible resistance observed at the initial stage of the filtration. The total irreversible resistance is assumed to remain constant during the filtration. The use of the reversible and the irreversible resistance concept is attractive because these resistances can be easily estimated experimentally and provide some explanation of the fouling mechanisms.

The present work was motivated by the desire to understand the fouling observed during the concentration of electroacidified soy protein extract in a hollow fiber ultrafiltration system. The model considers only the proteins and does not take into account the carbohydrates and the minerals contained in the soy protein extract. It is assumed that all the low molecular weight components, carbohydrates and minerals, permeate freely through the membrane pores such that the proteins are the only membrane foulant. This assumption is based on the experimental observations reported by Skorepova [49] where the proteins represented at least 93% of the total solids deposited on the membrane during the ultrafiltration of non-electroacidified and electroacidified soy protein extracts. The transient fouling resistances constitute a boundary condition (Darcy's law and resistance-in-series model) when solving the momentum and protein concentration continuity equations. In the current study, we have selected a formulation that allows easily accessible experimental estimation of the fouling resistances. The global fouling resistance consists of the membrane resistance, the reversible fouling resistance (water removal) and the irreversible fouling resistance (chemical removal). A new transient fouling resistance model based on the initial fouling resistance conditions, local permeate flux, pressure difference and protein concentration, was developed to describe the reversible and irreversible fouling resistance components. The viscosity of the soy protein extracts was considered as a function of protein concentration and pH to represent the electroacidification effect. The model was calibrated with experimental transient permeate flux and protein concentration data. Different patterns of initial and transient irreversible and reversible fouling resistances according to the pH of the soy protein solution were experimentally observed and simulated by the model. In contrast to the classical numerical modeling approach, this study takes advantage of CFD modeling tools to combine the hydrodynamics and the solute transport with the fouling behavior for a hollow fiber membrane ultrafiltration system and feed tank and obtain estimates of the spatial and transient protein concentration and velocity profiles inside the fiber by solving the equation of

motion coupled with the continuity equation for the soy protein. The model, validated with independent experimental data, showed the effect of two operating parameters, feed velocity and trans-membrane pressure, on the spatial and transient permeate velocity and protein concentration profiles. Estimates of the spatial and transient reversible and irreversible fouling resistances were also obtained and served to better understand the concentration operation and the effect of electroacidification during the ultrafiltration of soy protein extracts.

3.2 Modeling

3.2.1 Computational geometry

The system that was modeled consisted of a feed tank and a membrane hollow fiber module (Figure 3.1). During the filtration, the feed solution was pumped through the module and the retentate was returned to the feed tank while the permeate was collected. The hollow fiber membrane module contained 50 fibers with a 5.0×10^{-4} m radius and 0.3 m length. Every fiber was assumed identical and only one fiber was modeled. Figure 3.2 presents the major hydrodynamic characteristics of a fiber.

3.2.2 Governing equations of the hollow fiber

The governing equations, the equations for conservation of mass, protein concentration and momentum, in 2D-cylindrical coordinates are mathematically given in equations 3.1-3.3 (no variation in θ direction) [41,51]. The Reynolds number is smaller than 1500 so that the flow is laminar. The equations solved are:

$$\nabla.\boldsymbol{u} = \frac{\mathbf{1}}{\boldsymbol{r}}\frac{\partial}{\partial r}(rv_r) + \frac{\mathbf{1}}{\boldsymbol{r}}\frac{\partial v_\theta}{\partial \theta} + \frac{\partial v_z}{\partial z} = 0 \tag{3.1}$$

$$\frac{\partial C}{\partial t} + v_z\frac{\partial C}{\partial z} + v_r\frac{\partial C}{\partial r} = \frac{1}{r}\frac{\partial}{\partial r}\left(Dr\frac{\partial C}{\partial r}\right) + \frac{\partial}{\partial z}\left(D\frac{\partial C}{\partial z}\right) \tag{3.2}$$

$$\rho\frac{\partial \boldsymbol{u}}{\partial t} + \rho\boldsymbol{u}.\nabla\boldsymbol{u} = \nabla.\left(-PI + \mu(\nabla\boldsymbol{u} + (\nabla\boldsymbol{u})^{\boldsymbol{T}})\right) + \boldsymbol{F} \tag{3.3}$$

In the previous equations, **u** is the velocity vector, v_z, v_r , and v_θ are the velocity components in the z, r, and θ directions, respectively, ρ is the fluid density, P is the pressure, μ is the fluid viscosity, C is the protein concentration and D is the average protein diffusion coefficient. The density and the diffusion coefficient are assumed constant during the filtration; the viscosity varies during the filtration and depends on the protein concentration and electroacidification conditions (see section 3.2.5).

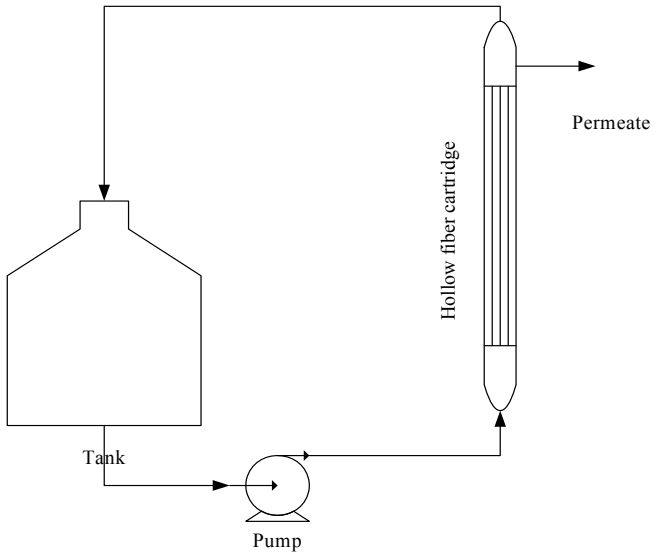

Figure 3.1 Computational geometry consisting of the feed tank and the ultrafiltration hollow fiber module

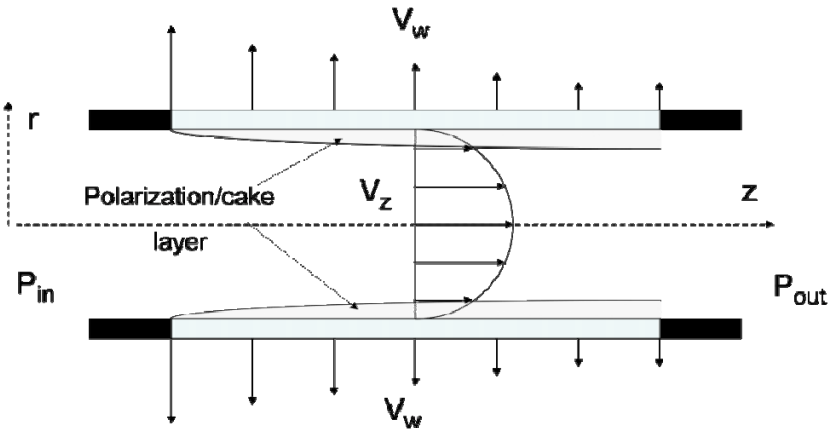

Figure 3.2 Simplified representation of the hydrodynamics in the hollow fiber

3.2.3 Initial and Boundary conditions of the fiber

At the inlet of the fiber, the flow is assumed to be fully developed and a parabolic flow is specified. It was assumed that entrance effect on fluid flow was negligible since the fiber radius was very small. The length that the flow becomes fully developed was calculated to be less than 10% of the fiber length. The maximum velocity ($v_{z,max}$) of the inlet parabolic flow is computed from the feed flowrate and the dimension of the fiber. The outlet pressure (P_{out}) is related to the trans-membrane pressure TMP and the total pressure drop in the fiber. Furthermore, the protein concentration at the inlet of the fiber is taken to be the concentration in the feed tank.

$$at\ z = 0,\ v_z = v_{z,\max}(1-(\frac{r}{R})^2),\ v_r = 0, C = C_F(t) \tag{3.4a}$$

$$at\ z = L, P = P_{out},\ \frac{\partial C}{\partial z} = 0 \tag{3.4b}$$

The outlet boundary condition, P_{out}, is a common boundary condition in fluid dynamics as recently used [43]. The fiber is axisymmetric therefore:

$$at\ r = 0,\ \frac{\partial v_z}{\partial r} = 0,\ v_r = 0,\ \frac{\partial C}{\partial r} = 0 \tag{3.4c}$$

A no slip boundary condition is defined at the membrane surface [52].

$$at\ r = R,\ v_z = 0,\ v_r = v_w \tag{3.4d}$$

Where v_W (z,t) is the permeate velocity. It is assumed that soy proteins are totally rejected by the 100 kDa membrane (verified previously where the protein content in the permeate was approximately 2 wt% and approximately 90 wt% in the retentate for cross-flow ultrafiltration concentration operation with a similar system and operating conditions [48]). The average particle size of the electroacidified and non-electroacidified soy protein extracts examined in this study was estimated previously, 220 nm and 707 nm respectively [4]. We also assumed that the

protein adsorbed on the membrane surface (irreversible fouling) is negligible compared to the magnitude of the protein concentration at the wall.

$$at\ r = R,\ \ v_w C\ - D\frac{\partial C}{\partial r} = 0 \tag{3.4e}$$

$$at\ t = 0, v_z = v_{z,\max}(1-(\frac{r}{R})^2), v_r = 0, C = C_F, P = P_{out} \tag{3.4f}$$

3.2.4 Governing equations for the feed tank

The feed tank is modeled as a well mixed continuous stirred tank. The change in the feed volume is obtained by writing a mass balance over the feed tank.

$$\frac{dV_F}{dt} = Q_{hf} - Q_F = -Q_{Per} \tag{3.5}$$

No protein accumulation in the pipe between the feed tank and the hollow fiber module is assumed. With the well mixed assumption, the transient protein concentration is uniform in the feed tank. The time change in the protein concentration is therefore represented by equation 3.6 and the permeate flux is obtained by integrating the local permeate velocity at the membrane surface according to equation 3.7:

$$\frac{dC_F}{dt} = \frac{Q_{Per}.C_F}{V_F} \tag{3.6}$$

$$Q_{per}(t) = (2n\pi R)\int_0^L v_W(z,t)dz \tag{3.7}$$

3.2.5 Physical properties of the solution

The density of the soy protein solution is assumed constant during the filtration. The effect of the soy protein concentration on the viscosity of the solution, however, is considered in the model.

$$\mu = \mu^0 \times \left(1 + \alpha^0 C\right) \tag{3.8}$$

where μ^0 is the water viscosity at 25°C, α^0 is an empirical coefficient specific to the electroacidification conditions estimated experimentally by Skorepova [49], and can be found in Table 3.1. A constant diffusion coefficient independent of protein concentration was assumed as an initial approach. The estimated average diffusion coefficient of 5×10^{-11} $m^2.s^{-1}$ was obtained from the literature for the non-electroacidified soy protein extract [53]. This value was used as a reference value to roughly estimate the diffusion coefficient for the electroacidified soy protein extract using Stokes-Einstein equation. Skorepova [49] reported that the average size of the electroacidified soy protein is 2-3 times larger than for the non-electroacidified soy protein extract. An average diffusion coefficient of 2.5×10^{-11} $m^2.s^{-1}$ was used for the electroacidified soy protein extract.

Table 3.1 Physical properties of the soy protein extracts

Model Parameters	Non-electroacidified soy protein extract	Electroacidified soy protein extract
α^0 ($m^3.kg^{-1}$)	0.0432	0.0196
D ($m^2.s^{-1}$)	5×10^{-11}	2.5×10^{-11}
ρ ($kg.m^{-3}$)	997	997

3.2.6 Permeate flux modeling

The local permeate velocity at the membrane surface (v_w $(z,t)_{r=R}$), the boundary condition for the equation of motion, was represented by Darcy's law (equation 3.9) and the resistance-in-series model (equation 3.10).

$$v_w(z,t) = \frac{\Delta P(z,t)}{\mu^0 . R_G} \tag{3.9}$$

$$R_G = R_m + R_R + R_I \quad (3.10)$$

ΔP(z,t) is the local transient pressure difference between the pressure P(z,t) inside the membrane fiber and the pressure outside the membrane fiber at a given position z along the fiber; ΔP(z,t) varies along the membrane and during the filtration process. The pressure outside the membrane fiber is atmospheric pressure. The operating trans-membrane pressure (TMP) is the average value of $\Delta P(z,t)$ estimated at the entrance and at the exit of the fiber.

In this study, we have selected a hydrodynamic approach to represent Darcy's law and the behavior of the retained components at the membrane surface. This approach includes the local transient pressure difference and sequential fouling resistances because these terms can be estimated experimentally, are directly related to the operation of the ultrafiltration process and have shown to represent accurately the concentration of soy protein extracts by ultrafiltration under similar operating trans-membrane pressure and concentrations [47]. In our hydrodynamic approach, the contribution of the osmotic pressure is implicitly described by the sequential fouling resistances.

The global fouling resistance R_G, as per equation 3.10, contains the clean membrane resistance R_m, the reversible fouling resistance R_R and the irreversible fouling resistance R_I. The reversible fouling was considered surface fouling that can be removed by water. The irreversible fouling was considered to occur either on the membrane surface or inside the membrane pores and is chemically attached to the membrane. Since the soy protein extracts consist of a mixture of proteins with different molecular size, standard blocking and pore blocking could occur during the filtration. These individual mechanisms were not distinguished in this study and were grouped as irreversible fouling.

Numerous models have been presented to describe the dynamics of resistance for the resistance–in-series approach. For example, Ho and Zydney [54] proposed a combined pore blockage and cake formation model to describe protein ultrafiltration. The cake formation represents the rate of protein deposit which is assumed to be proportional to the convective transport of protein. A different approach was proposed by Kilduff et al. [55] where the rate of cake formation contains

a convective transport term and a back transport term for the fouling of organic matter during nanofiltration operations. Tu et al. [46] proposed a power law approach to relate polarization, pore blocking and gel layer resistances to the major parameters and obtained the rate of formation by derivation of the power law for the fouling of organic matter during nanofiltration operations. These models were developed for a macroscopic analysis and do not consider the local variations of the wall concentration and the permeate velocity. The model proposed in this study considers the local spatial variation of the fouling resistances and their validation with experimental fouling measurements, that is to say the reversible fouling and irreversible fouling components that are related to the major fouling mechanisms (polarization, cake formation, and adsorption). The contribution of the reversible and the irreversible fouling resistances for the microfiltration and ultrafiltration of biological suspensions and the influence of operating parameters on the resistances was previously analyzed by Choi et al. [56]. Li et al. [57] have associated the reversible fouling resistance component to the polarization resistance and the cake resistance and the irreversible fouling resistance component to internal fouling for the ceramic filtration of soy sauce. These two previous studies were limited to steady-state conditions and did not present transient variation of the fouling resistances.

The local and spatial variation of the reversible and irreversible the fouling resistance components in the proposed model was developed as follows. The reversible fouling component was assumed to consist predominantly of the polarization resistance and increases due to the cake growth and its associated resistance (Li et al. [57], Choi et al. [56]). Due to the rapid formation of the polarization layer [58,59], the initial reversible resistance $R_{R\ initial}$ was considered to be the resistance of the initial polarization layer.

Experimental results, reported in the next sections, indicated that the initial reversible resistance, $R_{R\ initial}$, increased with increasing TMP and the relationship between $R_{R\ initial}$ and TMP was linear within the range of 27.5 kPa and 55 kPa. A similar relationship between polarization resistance and TMP was shown appropriate for the ultrafiltration of soy protein extracts (Kumar et al. [47]) and the ultrafiltration of soy sauce (Li et al. [57]) and Tu et al. [46] for filtration of organic matter. We combined these experimental results of the initial reversible resistance with the prior knowledge that polarization layer depends on axial position. Instead of TMP, the local pressure

drop at a given position along the fiber at t=0 ($\Delta P(z,0)$) was considered in the representation of the initial reversible fouling resistance:

$$R_R(t=0)=R_{R\ initial}=\beta\ (1+\lambda\times \Delta P(z,0)\ ) \tag{3.11}$$

The parameters β and λ (Table 3.2) were obtained experimentally (see section 3.3.3. for details). The transient reversible resistance also depends on the axial position since the dynamics of the reversible resistance where the predominant mechanism is cake formation. During the phase of cake formation, the increase of the cake resistance depends on the permeate velocity and protein concentration [50]. In the proposed model, the reversible resistance rate was assumed proportional to the local permeate velocity, $v_w(z,t)$, and the local protein concentration at the membrane surface at a given position along the fiber, $C_w(z,t)$.

$$\frac{dR_R(z,t)}{dt}=\frac{v_w(z,t)C_w(z,t)}{k_R} \tag{3.12}$$

The parameter k_R was obtained by minimizing the error between the prediction and the experimental data for the permeate flux and the protein concentration at TMP = 34.5 kPa. Experimental results obtained at TMP = 41.5 kPa for the non-electroacidified soy protein extract served for the model validation.

The irreversible resistance refers to the protein adsorption and depends primarily on the physicochemical properties of the membrane and the soy protein extracts (ionic strength, pH) rather than the hydrodynamics of the process [13]. The irreversible steady-state resistance, $R_{I,ss}$, corresponds to the situation where after a given time, no experimental variation was detected and was considered as steady-state. Previous studies for BSA indicate that the protein adsorption on the membrane surface reaches a plateau with time. Matthiasson [60] filtered BSA solutions with a dead-end membrane system and observed that the adsorption of BSA had already reached a plateau after 10 minutes. Turker and Hubble [61] investigated BSA adsorption on hollow fiber membrane surface and observed an equilibrium after 20 minutes. Based on these observations, the dynamics of the irreversible fouling resistance were assumed to be first-order (equation 3.13)

with an apparent time constant τ_I that depends on the protein concentration at the membrane surface and the initial condition given by equation 3.14.

$$\tau_I \frac{dR_I}{dt} = (R_{I,ss} - R_I) \quad , \quad \tau_I = \frac{k_I}{C_w(z,t)} \tag{3.13}$$

$$R_I(t=0) = R_{I\,initial} \tag{3.14}$$

The initial and steady-state irreversible fouling resistances, $R_{I\ initial}$ and $R_{I,ss}$, were measured experimentally (section 3.3.3) and were directly used in the computational model. The time constant parameters k_I was obtained as for k_R. Figure 3.3 illustrates a summary of the model developed in the current study.

Table 3.2 Model parameters

	Non-electroacidified soy protein extract	Electroacidified soy protein extract
k_R (kg.m^{-1})	1.8×10^{-12}	0.8×10^{-12}
k_I (kg.s.m^{-3})	1.4×10^{5}	2.0×10^{5}
$R_{I\,ss}$ (m^{-1})	2.0×10^{12}	4.2×10^{12}
*R_m (m^{-1})	1.5×10^{12}	1.5×10^{12}
$R_{I\,initial}$ (m-1)	5.8×10^{11}	1.3×10^{12}
β (m-1)	1.5×10^{12}	0.8×10^{12}
λ (Pa-1)	2.5×10^{-5}	5.7×10^{-5}
C_F (kg.m-3)	10	10

*Membrane resistance was 1.5×10^{12} m^{-1} unless stated

3.2.7 Mesh geometry

Non-uniform triangular [37,39,41] and quadrilateral mesh elements [62] with different resolution were adopted with the mesh density being higher near the membrane surface (Figure 3.4). The specified maximum size of element and the growth rate of the elements controlled the automatic meshing on the membrane boundary (exponential growth rate). Different mesh resolutions, 1247, 1773, 2021, and 2405, were considered to identify the mesh dependency of the model. Protein concentration along the radius of the fiber at the half length of the fiber (z = 0.15 m) was plotted

for each mesh resolution and percent error at each element was calculated with equation 3.15. The mesh refinement was stopped when a 0.1% average error was reached. In order to investigate the effect of mesh type on the result, simulations were carried out with both triangular mesh and quadrilateral mesh. The mesh refinement was stopped at the mesh resolution of 2021 because the average error of 0.1% was reached. The results obtained from the model with 2021 triangular elements were compared with those of the 2010 quadrilateral mesh elements and only 0.16% average error was observed.

$$Error(\%) = \left|\frac{Protein\ Concentration_{smaller\ mesh\ size} - Protein\ Concentration_{larger\ mesh\ size}}{Protein\ Concentration_{smaller\ mesh\ size}}\right| \times 100 \qquad (3.15)$$

Finally, a triangular mesh with the resolution of 2021 with 15 cells along the symmetry line, 17 cells across the half of the channel, and 146 cells for the membrane was chosen for this work because it turned out that some functions were not available in COMSOL Multiphysics when quadrilateral mesh is selected.

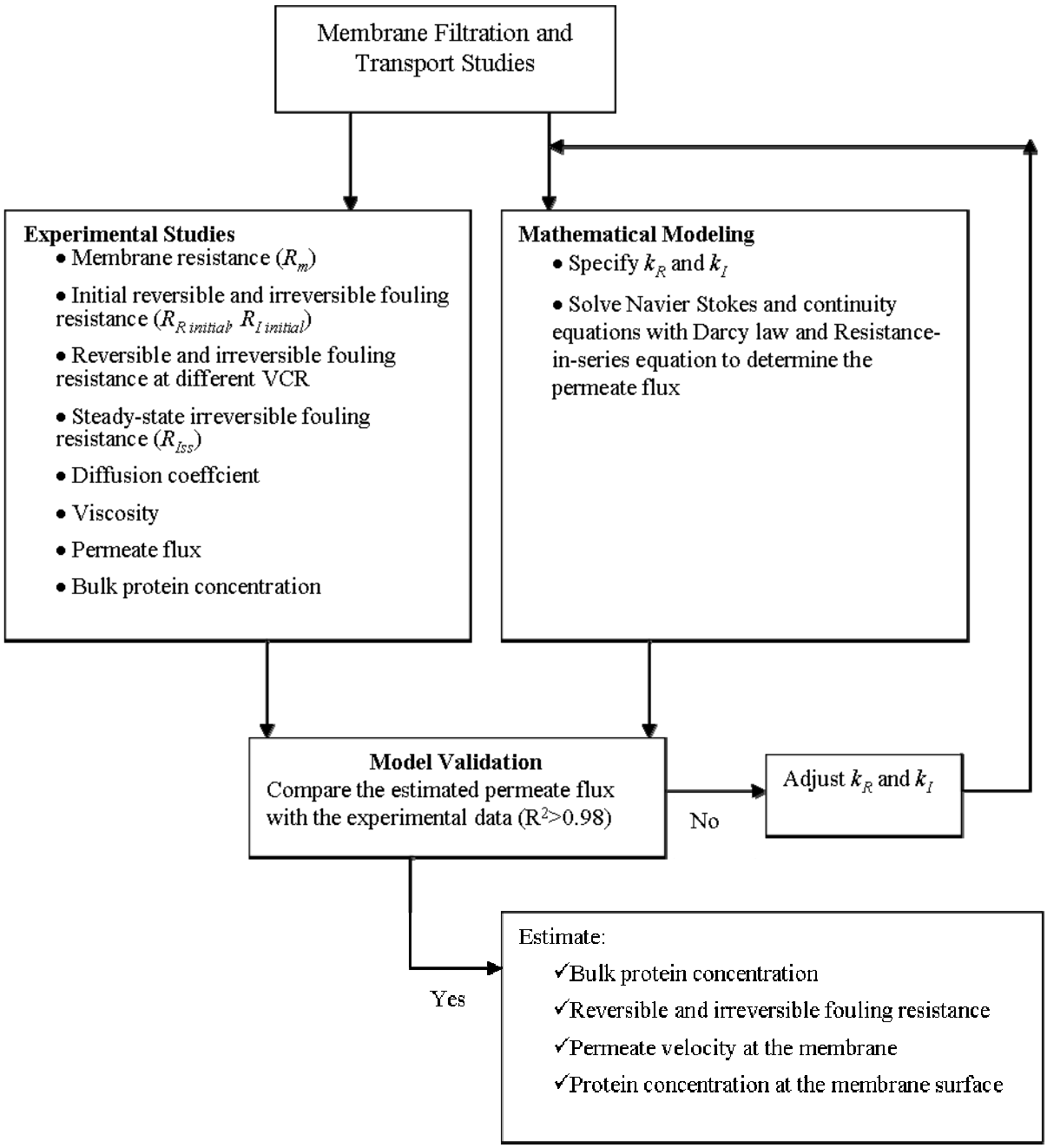

Figure 3.3 Methodology for model development and validation

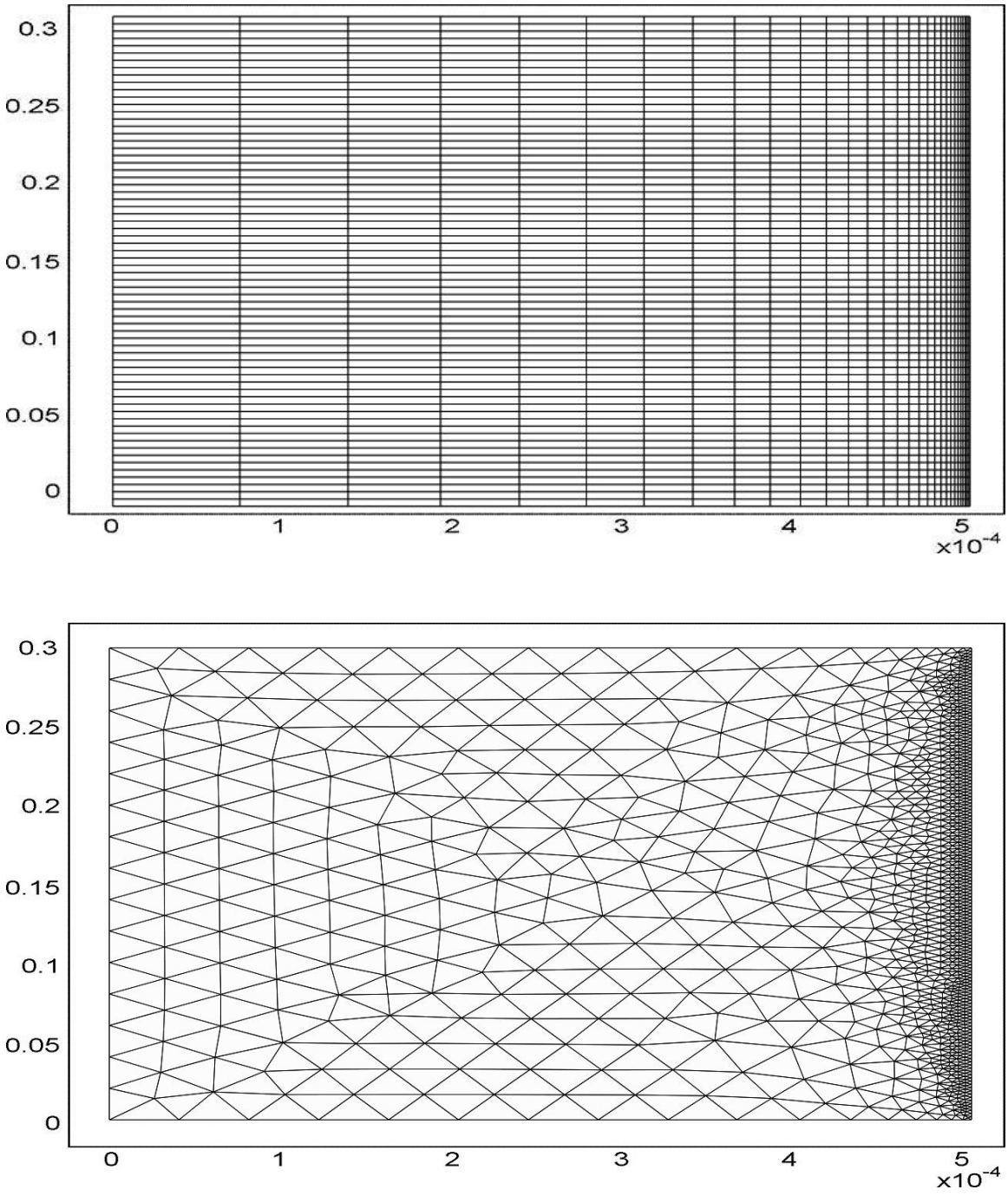

Figure 3.4 Quadrilateral (top) and triangular (bottom) mesh of a hollow fiber

3.2.8 Numerical solution

CFD tools use finite element method or finite volume method. For membrane filtration, the two methods have been used. For instance, Subramani et al. [37], Huang and Morrissey [39] and Ma et al. [26] used finite element methods to simulate the velocity and the concentration in the membrane system. The momentum equation is not difficult to be solved under laminar conditions. The diffusion convection equation (protein concentration in this study) may present potential difficulties for the finite element method and the finite volume method. The large concentration gradient near the membrane and the large Peclet number in the same region cause challenges for the accuracy and the artificial diffusion. The use of specific numerical schemes (UPwind Petrov Galerkine) and a fine meshing addressed these issues; these features are available in COMSOL and were used in this study. The commercially available finite element code, COMSOL Multiphysics (version 3.5), was used to solve the governing equations. According to the finite element principles, COMSOL Multiphysics converts the partial differential equations of the model (strong form) to the weak form by multiplying the model equations with a test function, followed by integration which involves integration by parts of the flux term at the boundary. After the finite element discretization, a set of differential algebraic equations was obtained and solved by a variable step-size backward differentiation formula (BDF). The BDF is a family of implicit methods for the numerical integration of differential equations. The BDF order is variable and ranges between 1 and 5, a smaller value results in a more stable numerical scheme. Decreasing the order to 2 often gave better results, because the higher-order algorithms were only stable when the time step was small, while the order-2 algorithm was unconditionally stable. The direct solver, UMFPACK, was used to solve the resulting linear system. UMFPACK solves linear systems with the nonsymmetric-pattern multifrontal method and direct LU factorization of the sparse matrix. The ordinary differential equations describing the resistance dynamics were introduced with the weak formulation (related to the mathematical weak form) on the boundary of the domain. The ordinary differential equations describing the tank dynamics were solved with a Runge Kutta method provided by COMSOL. For the cylindrical geometry investigated in this study, a validation was performed with the approximated analytical solution (Yuan's solution) for the equation of motion and a porous wall. Very good agreement was obtained (data not shown) demonstrating that the CFD numerical tool is adequate. A Pentium 2.13 GHz with 2 GB of Ram was used for the numerical

tests. The simulations were assumed to converge when the weighted absolute residual norm was less than 10^{-5}.

3.3 Experimental

3.3.1 Materials and methods

Electroacidified and non-electroacidified soy protein extracts, containing approximately 60 % (w/w) protein, 30 % (w/w) carbohydrates, and 10 % (w/w) ash, were provided by Agriculture and Agri-Food Canada (Saint-Hyacinthe, QC, Canada). A 2% (w/w) soy protein extract solution was prepared by mixing a preweighed amount of SPE powder with Nanopure water (resistivity > 17.5 MΩ-cm) and was stirred at room temperature for 1h to allow rehydration. The suspension was then centrifuged at 10000 RPM for 17 min at 23˚C using a Beckman Coulter L7-35 ultracentrifuge (Mississauga, ON, Canada) to remove any insoluble components. The supernatant was used as the feed solution for the ultrafiltration concentration experiments. The initial protein concentration in the feed solution was 10 $g.L^{-1}$ for all experiments. pH and ionic strength (±0.001, S80 SevenMulti^{TM} pH meter, Mettler Toledo, OH, USA) of the solution were 6 and 0.01M for the electroacidified soy protein extract and 9 and 0.014M for non-electroacidified soy protein extract, respectively.

3.3.2 Experimental setup

The details of the experimental set-up are given in Figure 3.5. Briefly summarized, an asymmetric polysulfone hollow fiber membrane module (GE Healthcare, Baie D'Urfe, QC, Canada) with a nominal molecular weight cutoff (MWCO) of 100 kDa was used in this work (membrane intrinsic resistance=1.5×10^{12} m^{-1}). The module was 30 cm in length with an approximate shell diameter of 2 cm contained 50 fibers of 1mm inner diameter. The membrane surface area was approximately 420 cm^2. The feed was pumped with a progressing cavity pump (Moyno Inc, Springfield, OH), and the flow rate was measured by a flowmeter (±5% of reading, Cole Parmer A-32477-04, 0.1 to 1 GPM). Pressure was monitored at the feed and the retentate side with two pressure transducers (±0.25% full-scale, Cole Parmer 0-50 psig A-68075-16). Trans-membrane pressure (TMP) was controlled on the retentate side by a manual pinch valve

(Cole Parmer A-98002-10). The flowmeter, pressure transducers and manual pinch valve were purchased from Cole Parmer Canada Inc. (Anjou, QC, Canada). The permeate was collected in a reservoir, and its mass measured with a balance ((±0.01g, Ohaus Corp., Pine Brooks, NJ, USA) and monitored by Labview 7.1 data acquisition system. Permeate flux was measured by weighing permeate at specified time intervals. All of the experiments were performed at 25±1 ˚*C*. Feed tank was placed in a water bath maintained at 25 ˚*C* (±1˚C, mercury filled thermometer). A 2L glass Erlenmeyer flask was used as a feed tank for experiments. The loop volume was about 200ml. The clean membrane resistance was estimated before each experiment with Darcy's law and ΔP = TMP in equation 3.9, for different TMP.

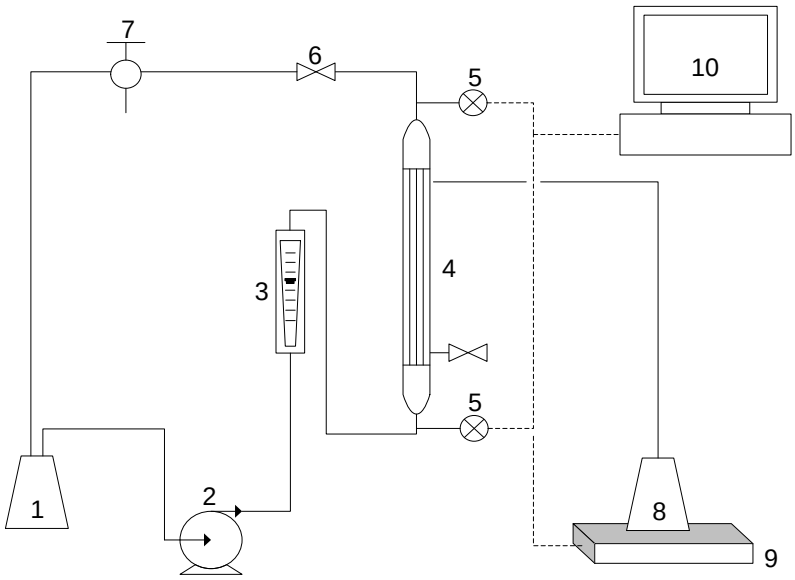

Figure 3.5 Schematic diagram of the filtration unit: 1-feed tank, 2-pump, 3-flowmeter, 4-membrane, 5-pressure transducers, 6-pinch valve, 7-sampling valve, 8-permeate container, 9-balance, and 10-PC/software (adapted from [49])

3.3.3 Initial fouling resistance estimation

The first sets of experiments were performed to analyze the fouling mechanisms at the beginning of the filtration. The filtration, performed at different TMP for both electroacidified and non-electroacidified soy protein extracts, was stopped after 2 minutes to measure the reversible and irreversible fouling resistances. After the 2-minute filtration period, the membrane was rinsed

with 1L Nanopure water in both non-recycle and total recycle mode at the same operating conditions as the filtration. The water flux was then measured and used to estimate the initial irreversible resistance ($R_{I\ initial}$). The initial reversible resistance ($R_{R\ initial}$) was calculated by subtracting the sum of the clean membrane resistance and the initial irreversible resistance from the global resistance (equation 3.9). After each 2-minute filtration, the membrane was chemically washed to remove the irreversible fouling. The experimental values of $R_{I\ initial}$ and $R_{R\ initial}$ were directly used in the computational model as the initial conditions for the filtration.

3.3.4 Transient reversible (R_R) and irreversible (R_I) resistances estimation

To understand how the reversible and irreversible fouling resistances change during the concentration, filtrations were conducted at a number of specified *VCR* and a constant TMP to measure the reversible and irreversible fouling. The volume concentration ratio (*VCR*) is the extent of volume reduction during the filtration operation and is defined by equation 3.16.

$$VCR = \frac{V_F}{V_F - V_{per}} \tag{3.16}$$

where V_F and V_{per} are the volume of the feed and permeate, respectively. V_{per} is calculated by integrating Q_{per} over time.

The reversible and irreversible fouling resistances were measured at the end of the filtration as described in the previous section and were then compared with the results obtained from the CFD model.

3.3.5 Protein quantification

Protein concentration in the retentate was analyzed according to the Bradford assay (Standard Procedure for Microtiter Plates, Bio-Rad Laboratories, Mississauga, ON, Canada) with lyophilized bovine serum albumin (Bio-Rad Laboratories, #500-0007) as standard. Absorbance was read at 590 nm in the Multiskan Ascent spectrophotometer.

3.3.6 Experimentally investigated operating conditions

Hollow fiber ultrafiltration of soy protein solution was performed for electroacidified (pH 6) and non-electroacidified (pH 9) soy protein extracts for a TMP range of 27.5-41.5 kPa at 1m.s-1 axial velocity. Individual filtrations were conducted for the following VCR conditions, VCR=2; 2.4; 3.3 at pH 6 and VCR= 2; 3; 4 at pH 9. Temperature of the feed solution was maintained at 25 ºC through the concentration process (water bath). The ultrafiltration was continued up to about VCR 4. Permeate flux, protein concentration, reversible and irreversible fouling was measured with time during the concentration process.

3.4 Results and discussion

3.4.1 Experimental fouling observations

The first step for the model development was to characterize experimentally the fouling resistances for the initial conditions and as the concentration operation proceeded. The initial fouling resistances, measured experimentally after 2 minutes of concentration operation and distinguished as reversible fouling resistance (removed by water wash) and irreversible fouling resistance (removed by chemical cleaning), are presented in Figure 3.6. The initial irreversible fouling resistance for the electroacidified soy protein extract is double that of the non-electroacidified soy protein extract while the reversible fouling resistance is similar. The higher initial irreversible fouling resistance observed for the electroacidified soy protein extract suggests more significant protein-membrane interactions at pH6, pH conditions closer to the soy protein isoelectric point (4.8-5.2). These pH conditions represent lower electrostatic repulsion forces than for the non-electroacidified soy protein extract at pH 9. Also, the presence of quantifiable irreversible fouling resistance for both extracts can explain the observations previously reported for the discontinuous diafiltration approach, a dilution of the concentrated retentate solution after an initial concentration step, which was unable to improve the permeate flux for both the non-electroacidified and electroacidifed soy protein extracts [48]. As expected, the TMP affected mainly the initial reversible fouling resistance that increases with increasing TMP. Based on these observations, the effect of TMP on the initial reversible fouling resistance for the model development was represented with a linear relationship in equation 3.11 and with the parameters presented in Table 3.2. The initial reversible fouling resistances for the non-

electroacidified soy protein extract are slightly greater than those of the electroacidifed soy protein extract.

The second step was to validate the transient resistance model estimates with independent experimental data obtained for the entire concentration operation. Table 3.3 presents model and experimental fouling resistances at different VCR conditions. In general, there is a good agreement between experimental and model estimates. The reversible fouling resistances are quite similar for both extracts. In contrast, the irreversible fouling resistances are more significant for the electroacidified extract. The irreversible fouling resistance increases initially with a subsequent leveling off observed for both the non-electroacified and the electroacidified soy protein extracts. This behavior was estimated by equation 3.13 and the parameters presented in Table 3.2. In contrast, the reversible fouling resistance increases as long as the filtration operation continues as represented by equation 3.12. The increase is more pronounced for the electroacidified soy protein extract. For example, at VCR=3, the reversible fouling resistance of the non-electroacidified soy protein extract has doubled while for the electroacidified soy protein extract it has tripled. It appears that pH has an effect on the formation of the reversible fouling resistance related to the formation of the concentration polarization layer. The lower pH of the electroacidified soy protein extract allows proteins to come into closer contact forming a denser concentration polarization layer [7].

Table 3.3 Contribution of reversible and irreversible fouling during soy protein concentration by cross-flow ultrafiltration at TMP = 34.5 kPa, axial velocity = 1m.s^{-1}

VCR	Non-electroacidified soy protein extract				Electroacidified soy protein extract			
	Reversible fouling resistance, R_R (m^{-1})		Irreversible fouling resistance, R_I (m^{-1})		Reversible fouling resistance, R_R (m^{-1})		Irreversible fouling resistance, R_I (m^{-1})	
	Exp	Model	Exp	Model	Exp	Model	Exp	Model
1*	2.85×10^{12}	2.67×10^{12}	5.8×10^{11}	-----	2.27×10^{12}	2.38×10^{12}	1.31×10^{12}	-----
2	3.9×10^{12}	3.57×10^{12}	1.62×10^{12}	1.78×10^{12}	5.5×10^{12}	4.78×10^{12}	3.47×10^{12}	3.80×10^{12}
2.4	------	------	------	------	------**	5.19×10^{12}	3.92×10^{12}	3.93×10^{12}
3	5.2×10^{12}	3.99×10^{12}	1.92×10^{12}	1.93×10^{12}	------	------	------	------
3.3	------	------	------	------	7.4×10^{12}	5.89×10^{12}	4.17×10^{12}	4.07×10^{12}
4	5.28×10^{12}	4.26×10^{12}	2.03×10^{12}	1.97×10^{12}	------	------	------	------

* Estimated after 2 minutes of filtration. The experimental values of the initial fouling were directly imported to the model, as is explained in the text.
** The value was not reported due to the experimental error.

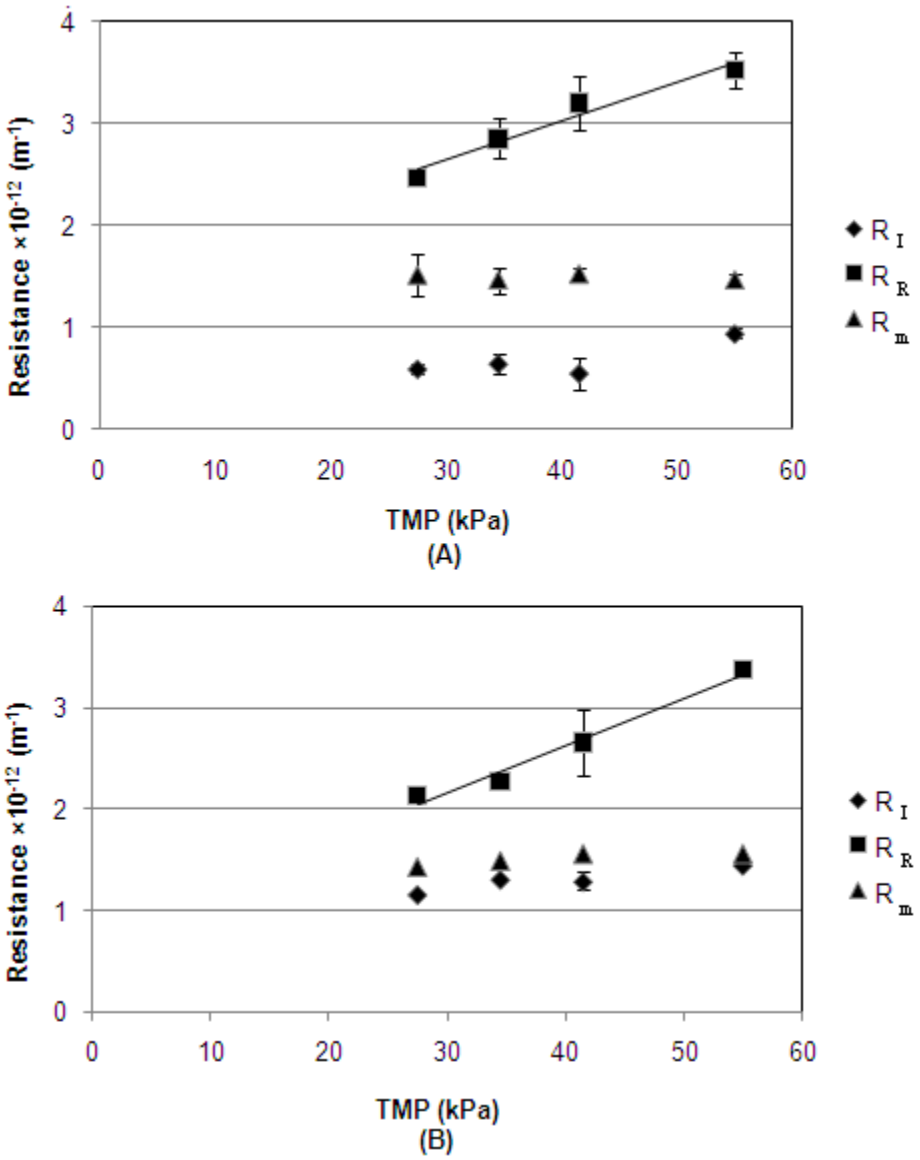

Figure 3.6 Effect of TMP on the initial fouling; axial velocity=1 m.s^{-1}; (A) Non-electroacidified soy protein extract; (B) Electroacidified soy protein extract (mean ± SD, n=2). Solid line shows the fit based on equation 3.12 and parameters Table 3.2

3.4.2 Permeate flux and protein concentration modeling

The permeate flux during the entire concentration operation was modeled for different conditions of inlet axial velocity and TMP and two types of soy protein extracts. The model incorporated the behavior of the initial and steady-state irreversible fouling resistances deduced from experiments. The model contained two adjustable parameters, k_R, k_I (Table 3.2) estimated by minimizing the error between the prediction and the experimental data for the permeate flux and the protein concentration at one TMP (34.5 kPa). There is a very good agreement between the model and the experimental data for the permeate flux (Figure 3.7) and the protein concentration in the retentate (Figure 3.8). The model validation also shows a good agreement between model estimates and experimental data for the permeate flux and the protein concentration of the non-electroacidified soy protein extract at a different TMP (41.5 kPa) (Figure 3.7A and Figure 3.8A). The effect of electroacidification pretreatment on the permeate flux and protein concentration (Figure 3.7 and Figure 3.8) is also well captured by the model. The estimates of the individual contribution of the reversible and the irreversible fouling resistances at different concentration conditions (VCR) corresponding to independent experiments for the non-electroacidifed and electroacidifed soy protein extract (Table 3.3) are also very good and demonstrates the applicability and ability of the CFD model to provide insights on the fouling mechanisms. Experimental and model estimates indicate that the reversible resistance is always higher than the irreversible resistance for the electroacidifed and non electroacidified soy protein extract. The difference is less pronounced for the electroacidified soy protein extract. The more significant reversible fouling resistance in comparison to the irreversible fouling resistance agrees with the observation made by Li et al. [57] for the microfiltration of raw soy sauce. Note that this model was able to estimate appropriately the magnitude of the two fouling resistance components and their transient behavior. Recent models have difficulty to evaluate accurately the balance between the different resistances. For instance, the model of Schausberger et al. [43] underestimated the polarization resistance and overestimated the adsorption resistance (with respect to their experimental measurements).

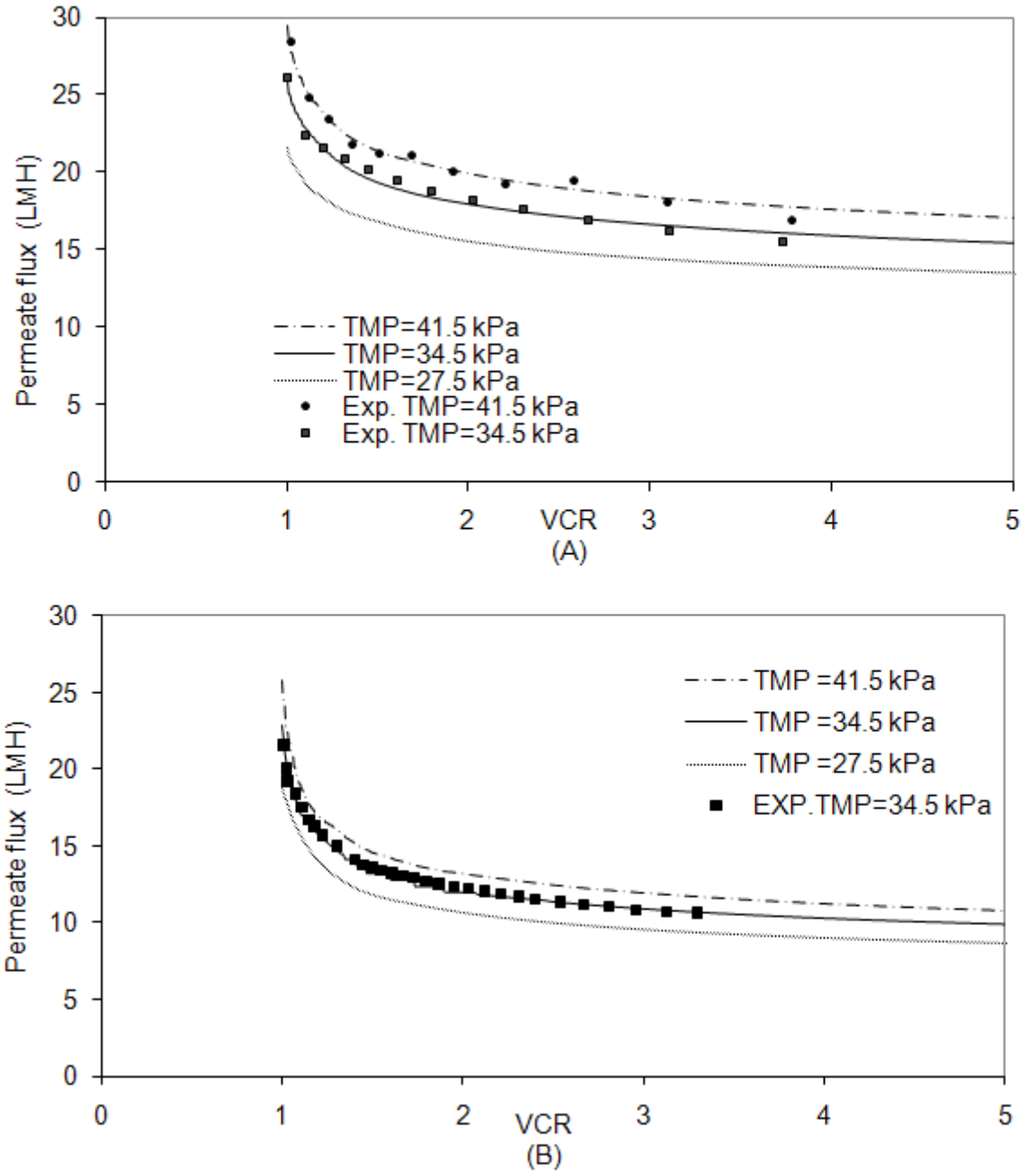

Figure 3.7 Effect of TMP on the permeate flux; axial velocity = 1 $m.s^{-1}$; (A) Non-electroacidified soy protein extract; (B) Electroacidified soy protein extract

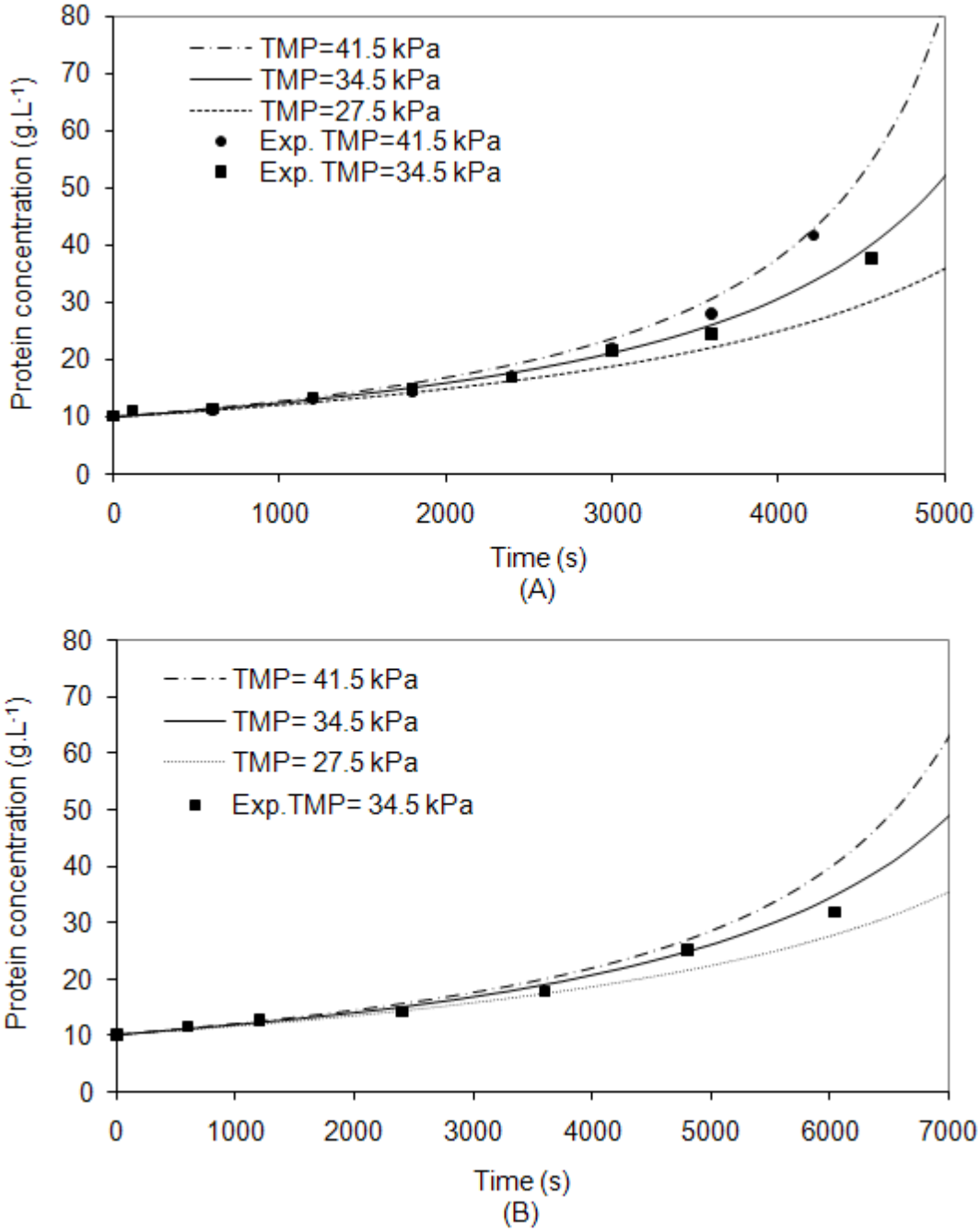

Figure 3.8 Effect of TMP on the bulk protein concentration; axial velocity = 1 $m.s^{-1}$; (A) Non-electroacidified soy protein extract; (B) Electroacidified soy protein extract

The model provides information on the two important operating parameters, TMP and inlet axial velocity. Increasing the TMP from 27.5 kPa to 41.5 kPa, improved the permeate flux during the entire concentration operation for both types of soy protein extracts. As the permeate flux is inversely proportional to the global fouling resistance (equation 3.9), a significant global resistance corresponds to a low permeate flux. The simulated results at VCR = 5 show a more pronounced effect of the TMP on the total fouling resistance (R_R+R_I) for the non-electroacidified soy protein extract, 7.20×10^{12}, 6.46×10^{12}, and 5.79×10^{12} m^{-1} at TMP of 41.5, 34.5, and 27.5 kPa, respectively in comparison with the electroacidified soy protein extract, 1.22×10^{13}, 1.09×10^{13} and 9.54×10^{12} m^{-1} at TMP of 41.5, 34.5, and 27.5 kPa, respectively. The effect of the TMP on the protein concentration was less pronounced but became more important only after 3000 seconds. The model estimates indicate that increasing the inlet axial velocities from 0.5 to 1.5 $m.s^{-1}$ reduces more significantly the filtration time to reach VCR = 5 for the electroacidified soy protein extract (8100 and 6840 seconds) compared to the non-electroacidified protein extract (5430 and 4890 seconds) as shown in Figure 3.9. The limited effect of the inlet axial velocity to improve the permeate flux supports the experimental observations where a significant irreversible fouling was already observed after 2 minutes of the concentration operation. A consequence of the limited effect of increasing axial velocity is reflected in the very small differences for the protein concentration in the retentate for different axial velocities (Figure 3.10).

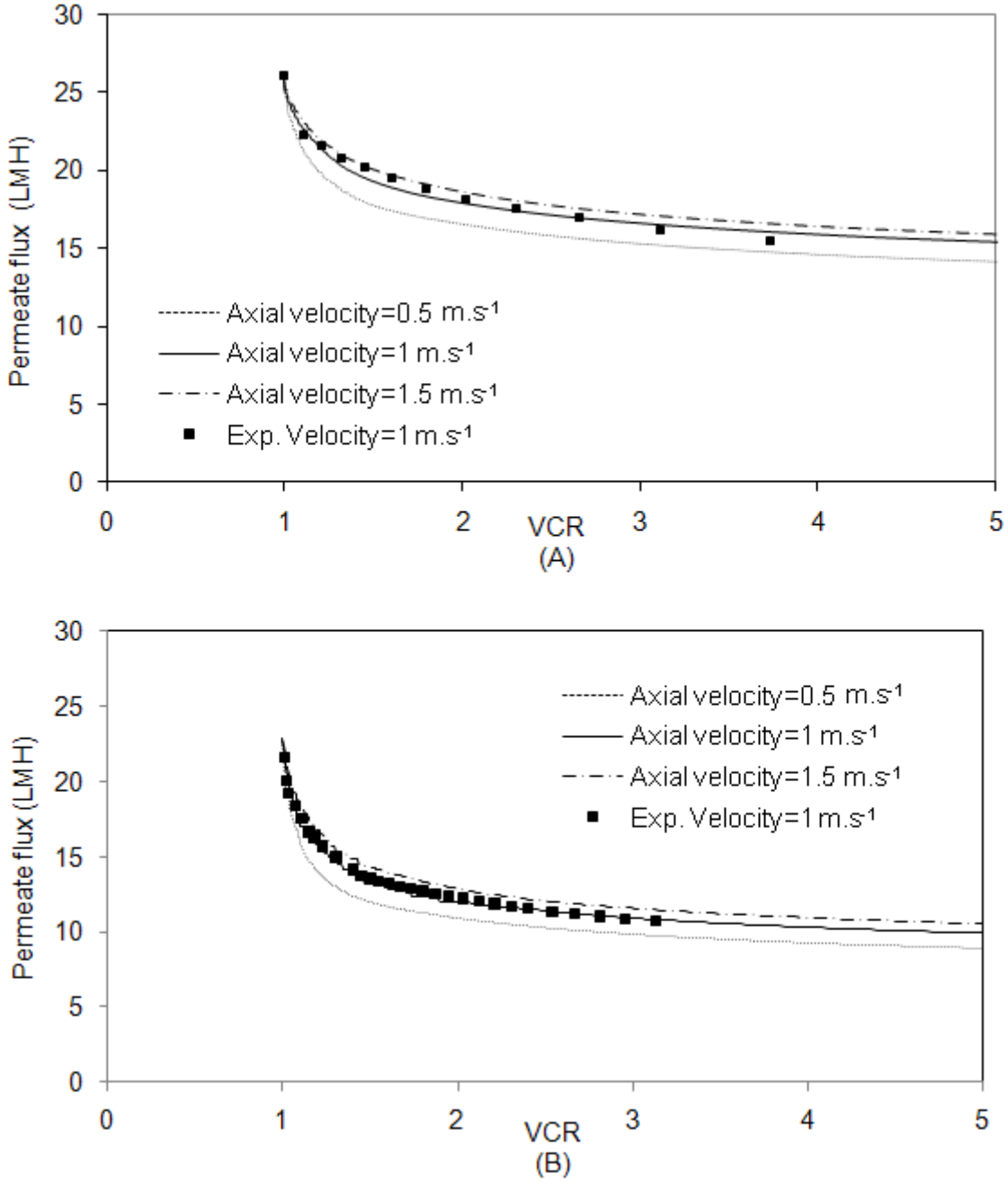

Figure 3.9 Effect of axial velocity on the permeate flux; TMP=34.5 kPa; (A) Non-electroacidified soy protein extract; (B) Electroacidified soy protein extract

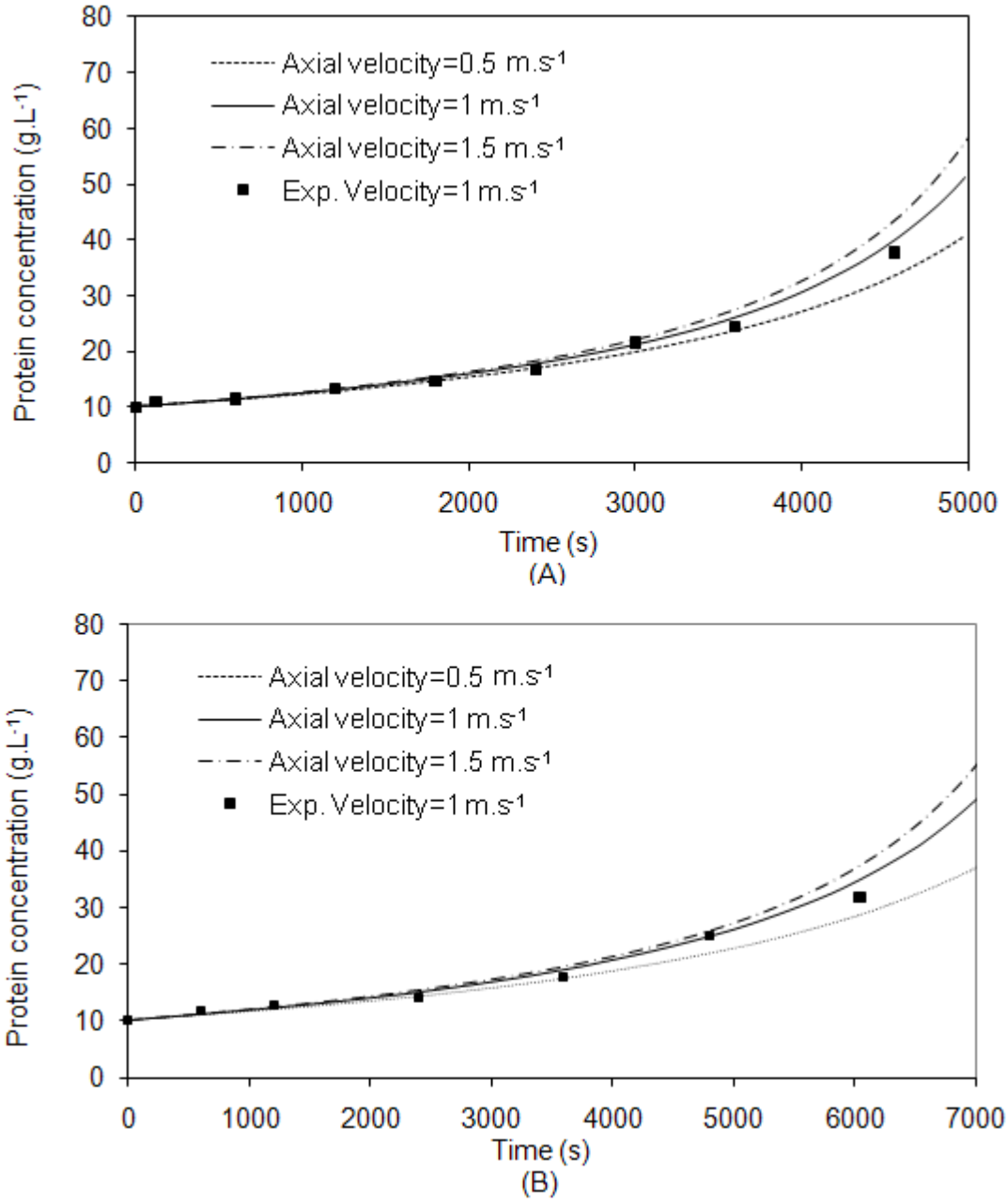

Figure 3.10 Effect of axial velocity on the bulk protein concentration; TMP=34.5 kPa; (A) Non-electroacidified soy protein extract; (B) Electroacidified soy protein extract

3.4.3 Effect of electroacidification on the fouling behavior

The CFD model, developed in this study and based on the dynamics of the reversible and irreversible fouling resistances specific to each soy protein extract (equations 3.12 and 3.13), provided spatial information on the axial fouling behavior, i.e. along the length of the fiber as the concentration operation proceeded (Figure 3.11 and Figure 3.12). Differences were observed according to the type of soy protein extract and the type of fouling resistance. The simulated reversible fouling resistance profile reached a maximum before the end of the fiber, which is more pronounced for the electroacidified soy protein extract and at higher VCR (Table 3.4). As VCR increases, the estimated reversible fouling resistance increases more significantly for the electroacidified soy protein extract. The reversible fouling resistance is related to the profile along the fiber of the permeate flux and the protein concentration at the membrane surface, which will be discussed in the next section. The simulated irreversible fouling resistance profile is very different. As shown in Figure 3.12, a sharp increase at the entrance of the fiber is predicted with a subsequent relatively constant value for the remaining fiber length. The initial sharp increase could be related to the concentration boundary layer that was not fully developed (Figure 3.13). The initial sharp increase was more pronounced for the electroacidified soy protein extract. For VCR = 3 and higher, the irreversible fouling resistance did not vary very much and seemed to reach a plateau and this behavior was observed previously [60,61].

Table 3.4 Model estimates of the maximum reversible resistance during soy protein concentration by cross-flow ultrafiltration at TMP=34.5 kPa and axial velocity=1m.s^{-1}

VCR	Non_electroacidified soy protein extract		Electroacidified soy protein extract	
	Estimated maximum reversible fouling resistance, R_R (m^{-1})	Position (m)	Estimated maximum reversible fouling resistance, R_R (m^{-1})	Position (m)
1	3.82×10^{12}	0	2.96×10^{12}	0
2	4.10×10^{12}	0.0135	4.98×10^{12}	0.158
3	4.38×10^{12}	0.0387	5.97×10^{12}	0.158
4	4.63×10^{12}	0.06	6.62×10^{12}	0.158
5	4.87×10^{12}	0.0682	7.12×10^{12}	0.149

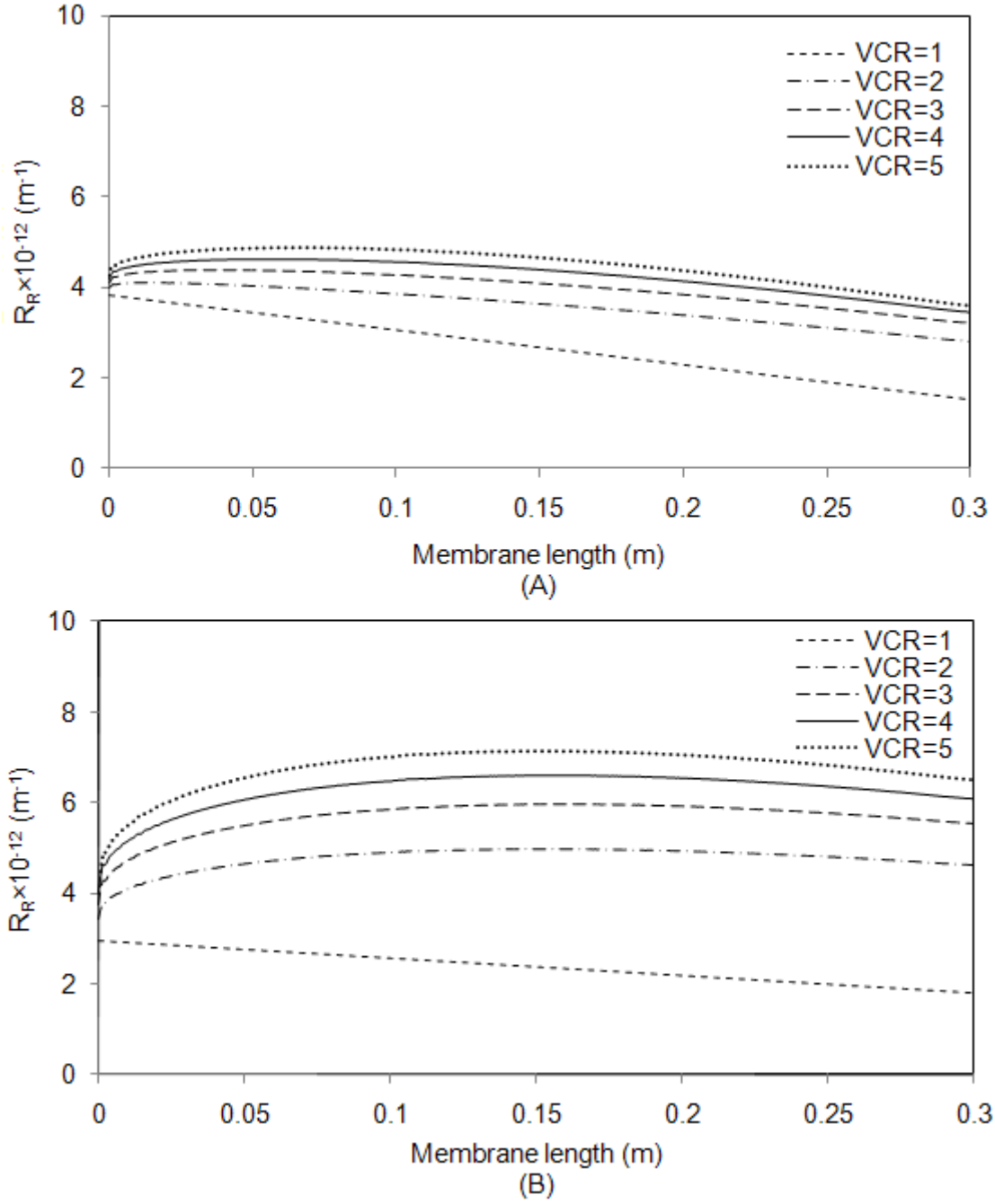

Figure 3.11 Effect of VCR on the estimated reversible fouling resistance; TMP = 34.5 kPa; axial velocity = 1 $m.s^{-1}$; (A) Non- electroacidified soy protein extract; (B) Electroacidified soy protein extract

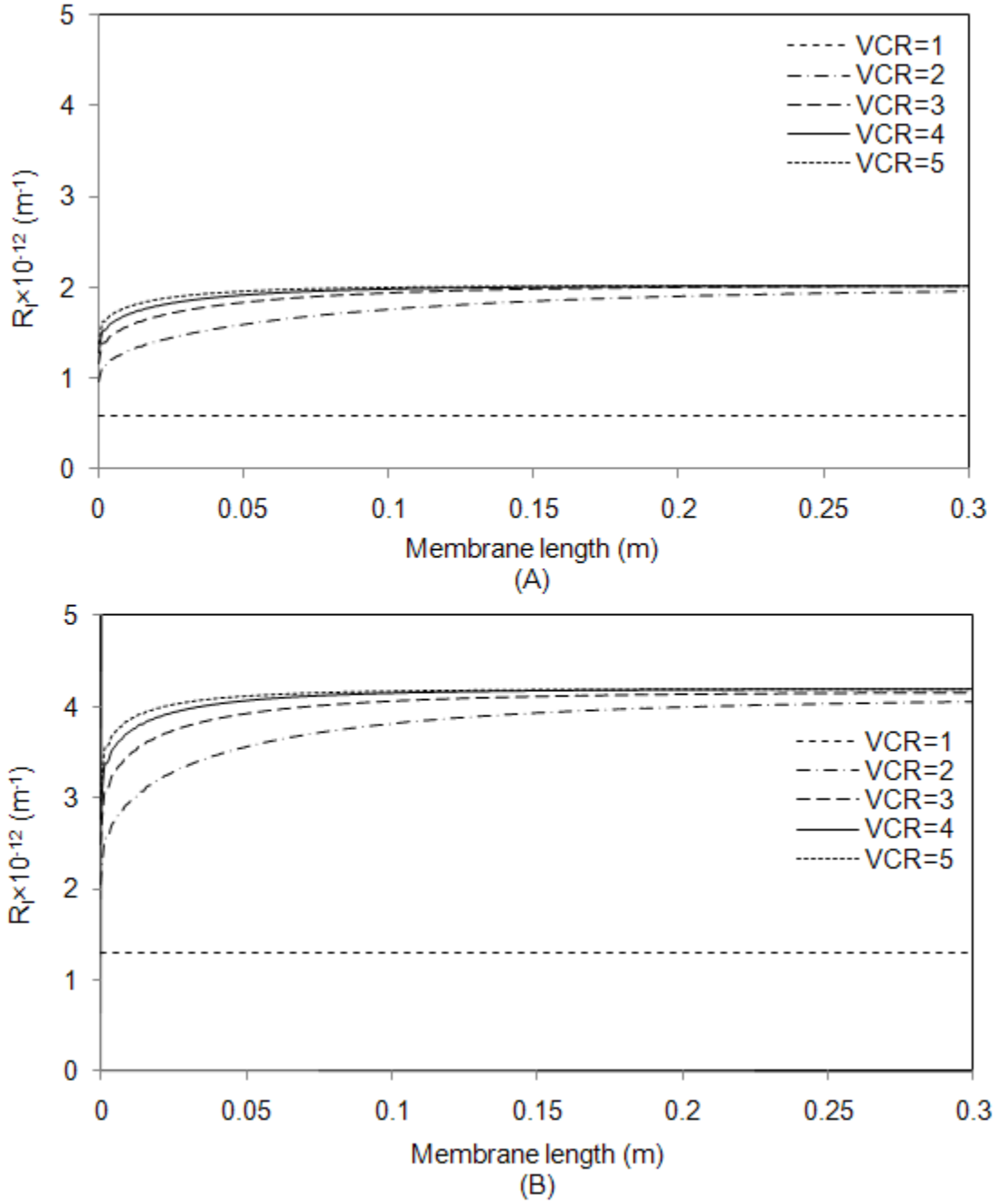

Figure 3.12 Effect of VCR on the estimated irreversible fouling resistance; TMP=34.5 kPa; axial velocity = 1 $m.s^{-1}$; (A) Non- electroacidified soy protein extract; (B) Electroacidified soy protein extract

As noted, the fouling behaviour is different between the electroacidifed and non-electroacidified soy protein extracts. The differences come from the pH effect. According to Marshall et al. [13], the pH affects protein for three reasons: the pH changes the protein conformation and its ability to deposit on the membrane; the pH changes the size of the protein or the size of protein aggregates; the pH changes the charge between the membrane and the protein. For soy protein extracts, previous studies reported size and charge differences according to electroacidification conditions. Mondor et al. [4] reported a larger mean particle diameter for the electroacidified soy protein extract at pH 6 reconstituted in water compared with the non-electroacidified soy protein at pH 9 and Skorepova and Moresoli [48] reported reduced interactions between proteins having a reduced negative charge for the electroacidified soy protein extracts and cations (minerals and phytic acids). In the context of fouling, the reduced negative charge and the larger diameter for the electroacidified soy protein extract could be associated with a more important protein adsorption and the more severe irreversible fouling observed experimentally in this study for the soy protein extracts subjected to electroacidification.

3.4.4 Protein concentration and velocity profile inside the membrane fiber

The estimated spatial protein concentration inside the fiber at VCR = 3 for non-electroacidified soy protein extract (Figure 3.13) presents a uniform protein concentration profile along the fiber length and away from the membrane surface confirming that the bulk protein concentration does not change significantly along the fiber. This uniform bulk protein concentration can be explained by the small permeate velocity compared to the axial velocity. The thickness of the concentration boundary layer increases along the fiber length but represents less than 10% of the fiber radius. The axial velocity profile (Figure 3.14) corresponds to the classical parabolic profile for laminar flow. It shows that the axial velocity inside the fiber is affected by the permeate velocity and the concentration boundary layer on the membrane surface as shown in the close-up of the membrane surface where a different profile is observed according to position along the fiber.

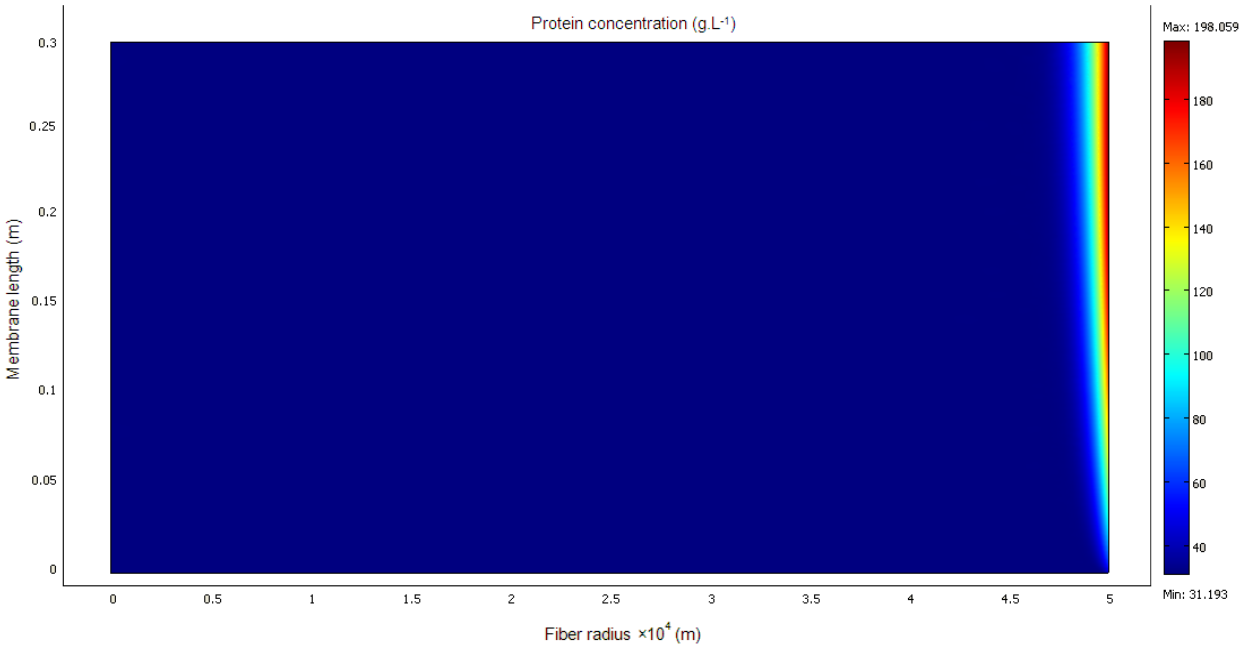

Figure 3.13 Protein concentration field inside the fiber, TMP=34.5 kPa; axial velocity = 1 m.s^{-1}; t = 4050 s; Non- electroacidified soy protein extract

Since the fouling is determined by the conditions near the membrane surface, it is important to analyze the protein concentration at the membrane surface ($C_w(z,t)$) and the permeate velocity ($v_w(z,t)$). The estimated protein concentration at the membrane surface increased significantly along the fiber length as concentration proceeded, ie increasing VCR (Figure 3.15) for both extracts. The position and the magnitude of the maximum are different according to VCR and type of soy protein extract. As the protein concentration at the membrane surface is related to the reversible fouling resistance according to equation 3.12, their differences are interrelated. The estimate of the average protein concentration at the membrane surface, for the non-electroacidified and electroacidified soy protein extract are 116 g/L and 118 g/L at VCR =2 and then increases to 258 g/L and 250 g/L at VCR 5. These values have the same order of magnitude as those found in Ref. [47] for soy protein concentrate. A predicted maximum protein concentration at the membrane surface before the exit of the membrane was also reported by Marcos et al. [41] for soy protein extracts and Ma et al. [26] for dextran solutions and was explained by a variable permeate velocity as considered in the current study.Figure 3.16 presents the estimated axial permeate velocity at the membrane surface. A decreasing local permeate velocity is predicted along the fiber length for both types of extracts. The decrease is linear at the

beginning of the filtration (VCR = 1, data not shown) because of the decreasing local trans-membrane pressure along the fiber (associated with the pressure drop inside the fiber). The decrease is more pronounced as the VCR increases and is more significant for the electroacidified soy protein extract. A non-linear axial velocity decrease was also predicted by Ma et al. [26] for dextran solutions when a variable viscosity was considered. Marcos et al. [41] reported a linear decrease as the concentration proceeded for non-electroacidified soy protein extracts. The viscosity relationship may explain the different predictions between our results and those reported by Marcos et al. [41].

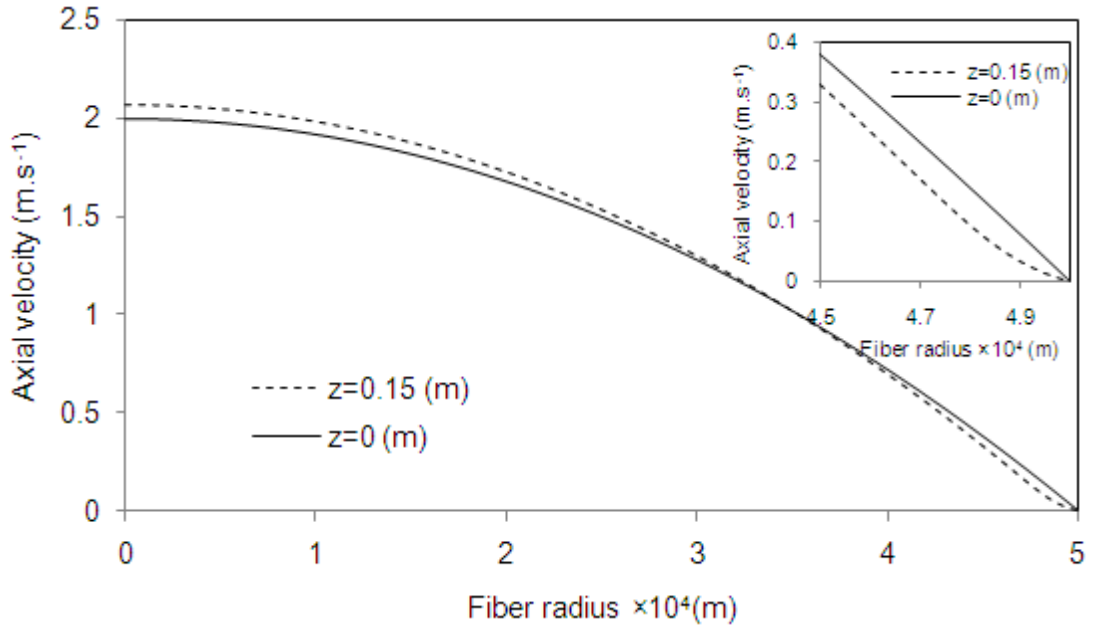

Figure 3.14 Estimated axial velocity profile along the fiber radius, TMP=34.5 kPa; axial velocity = 1 $m.s^{-1}$; t = 4050 s; Non- electroacidified soy protein extract. Insert shows the profile near the membrane surface

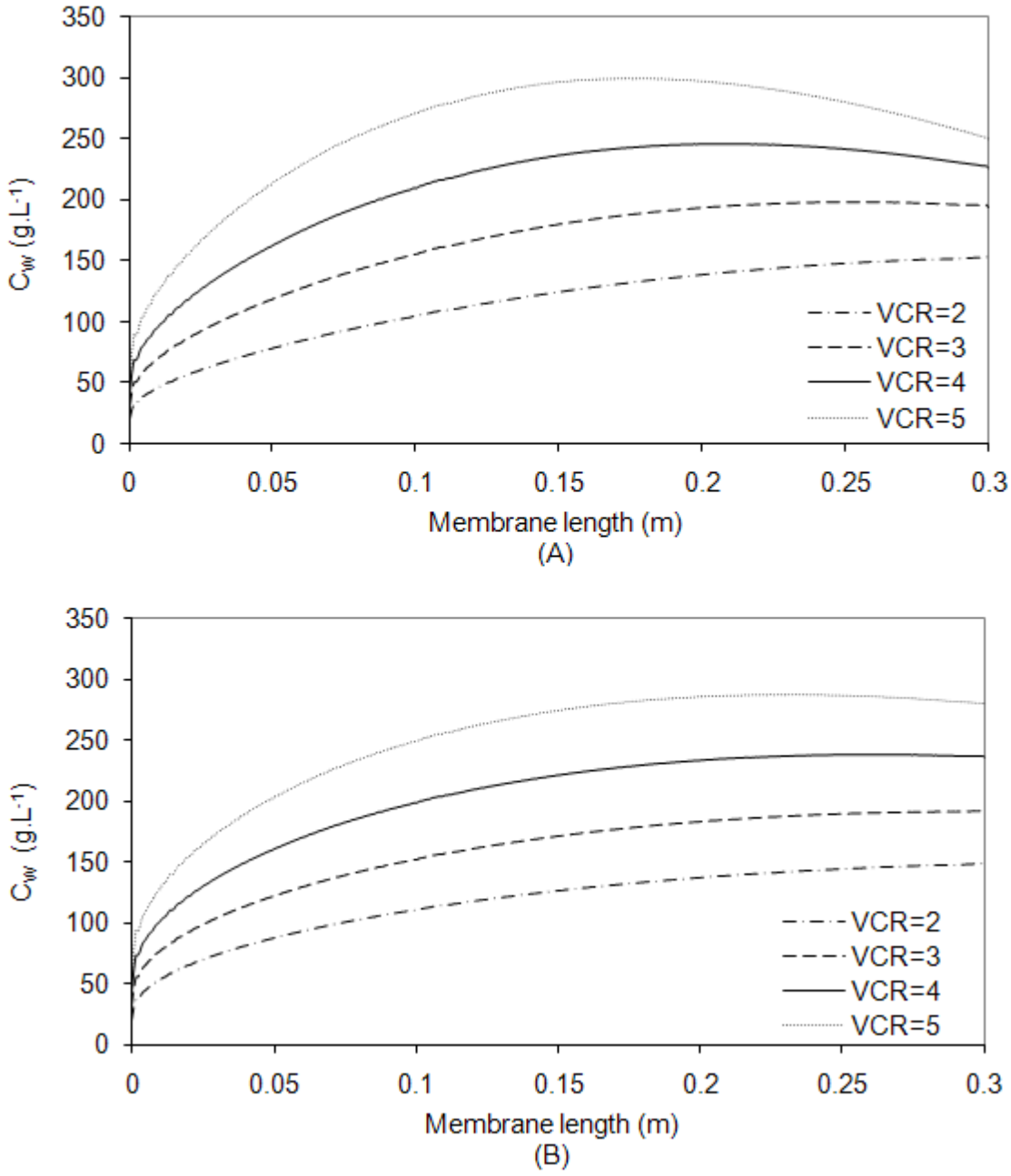

Figure 3.15 Effect of VCR on the estimated protein concentration at the membrane surface; TMP=34.5 kPa; axial velocity = 1 m.s^{-1}; (A) Non-electroacidified soy protein extract; (B) Electroacidified soy protein extract

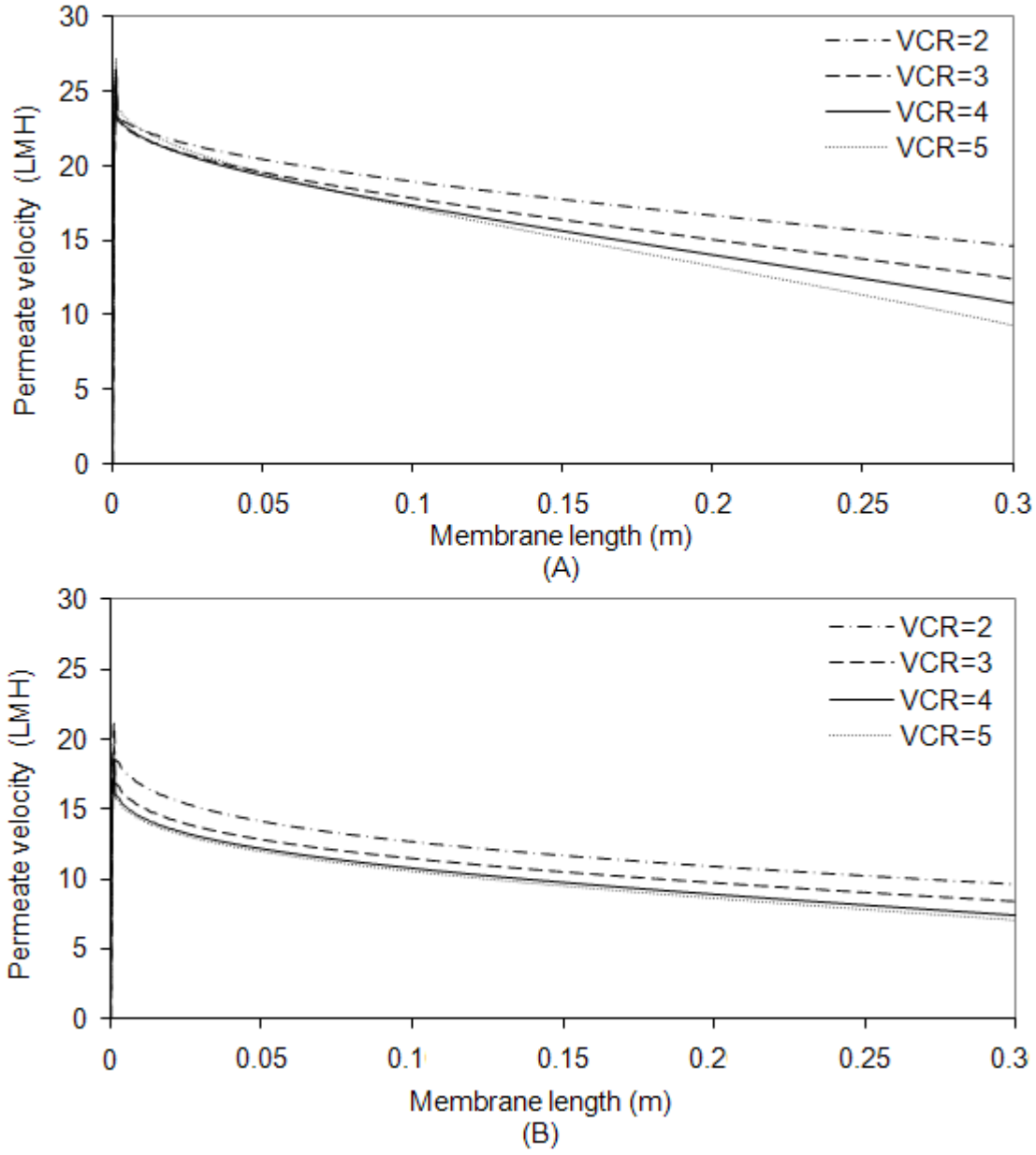

Figure 3.16 Effect of VCR on the estimated permeate velocity at the membrane surface; TMP=34.5 kPa; axial velocity = 1 $m.s^{-1}$; (A) Non-electroacidified soy protein extract; (B) Electroacidified soy protein extract

3.4.5 Effect of viscosity

UF is a pressure driven process in which the pressure drop along the fiber and the trans-membrane pressure play an important role in the fouling behavior. During the filtration, the protein concentration increases in the retentate and consequently the viscosity of the solution (equation 3.8). As the viscosity increases, the pressure drop will also increase. The effect of the viscosity on the estimated C_w is significant (Figure 3.17). When a low and constant viscosity (water) is considered, the protein concentration at the membrane surface increases along the fiber such that the maximum is observed at the end of the fiber. However, when a high viscosity with a protein concentration dependency is considered (equation 3.8), the maximum protein concentration at the membrane surface increases for both extracts and occurs before the exit of the fiber for the non-electroacidified soy protein extract. The critical viscosity, corresponding to the maximum protein concentration at the membrane surface is 0.002 Pa.s. Increasing the viscosity from 0.001 Pa.s (water) to 0.002 Pa.s is associated with a negligible increase of the average total fouling (R_r+R_I) at VCR = 3 (0.07% for the non-electroacidified and 0.6% for the electroacidified soy protein extracts). A more significant increase of the total fouling, 5 %, was estimated for both non-electroacidified and electroacidified soy protein extract when the constant value of 0.001 Pa.s for the viscosity was replaced by the concentration dependent viscosity (equation 3.8). This shows the importance of having the appropriate viscosity relationship with the contribution of the protein concentration and the effect of electroacidification.

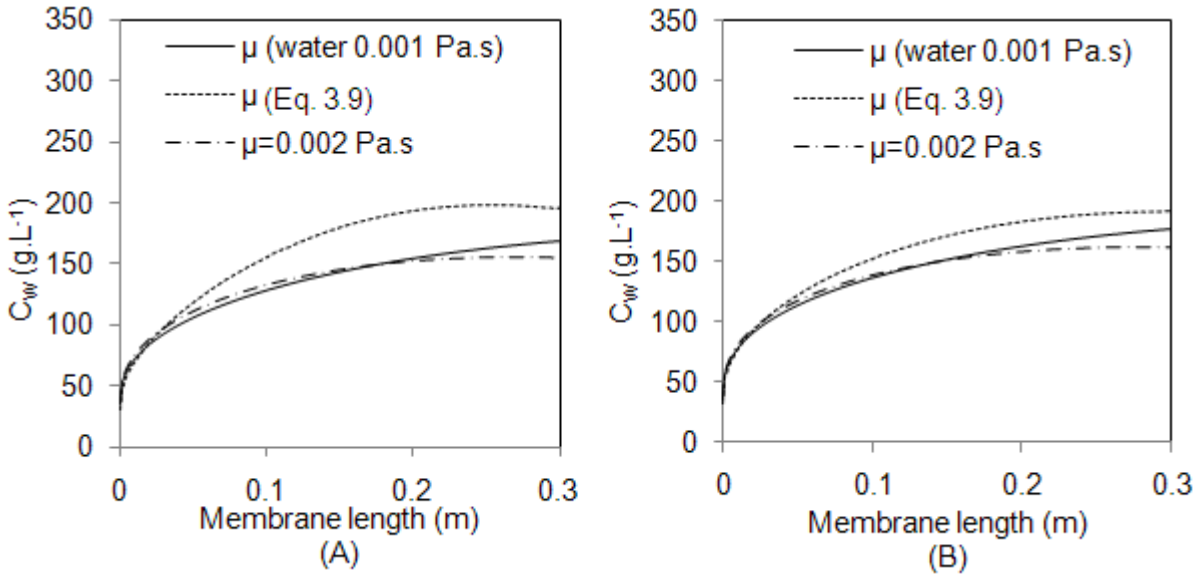

Figure 3.17 Effect of viscosity on the estimated protein concentration at the membrane surface; TMP=34.5 kPa; axial velocity = 1 m.s^{-1};t=4050 s; (A) Non-electroacidified soy protein extract; (B) Electroacidified soy protein extract

3.4.6 Model sensitivity analysis

Three parameters were selected to perform the model sensitivity analysis: the diffusivity coefficient, the parameter k_R (equation 3.12), and the parameter k_I (equation 3.13). The diffusivity coefficient was changed by ±50% and selected according to previous studies for BSA where the diffusion coefficient varies by about 50% when the concentration is multiplied by 10 (Keller et al. [63]). The parameters k_R and k_I were changed by ±10%. The protein concentration at the membrane surface (C_w) was chosen to evaluate the influence of the three selected parameters because it represents a local variable and has a very important role in the fouling dynamics. The effects of the different parameters were investigated for VCR = 3 and are reported for the non-electroacidified soy protein extract (Figure 3.18 a, b, c) and for the electroacidified soy protein extract (Figure 3.18 d, e, f).

The effect on the protein concentration at the membrane surface (Figure 3.18 a and d) when the diffusion coefficient decreases by 50% resulted in 52% and 32% increase for the non-electroacidified and electroacidified soy protein extract respectively. In contrast, the effect of a 50% increase for the diffusion coefficient resulted in 15% and 11% decrease of the protein

concentration at the membrane surface for non-electroacidified and electroacidified soy protein extract respectively. These estimates indicate that the protein concentration at the membrane surface is much more sensitive to the diffusion coefficient for the non-electroacidified soy protein suggesting that back transport associated with the diffusion coefficient plays a more important role.

A 10% increase in the irreversible fouling parameter, k_I shown in Figure 3.18 b and 3.18e, results in a negligible increase of the protein concentration at the membrane surface (1%). Increasing by 10% the reversible fouling resistance parameter, k_R, increases the protein concentration at the membrane surface by 4.6% for both the non-electroacified soy protein extract and the electroacified soy protein extract (Figure 3.18 c and f). Increasing the parameters k_R and k_I decrease the rate of growth of the fouling resistance that eventually increases the convective protein flux and the resulting protein concentration at the membrane surface.

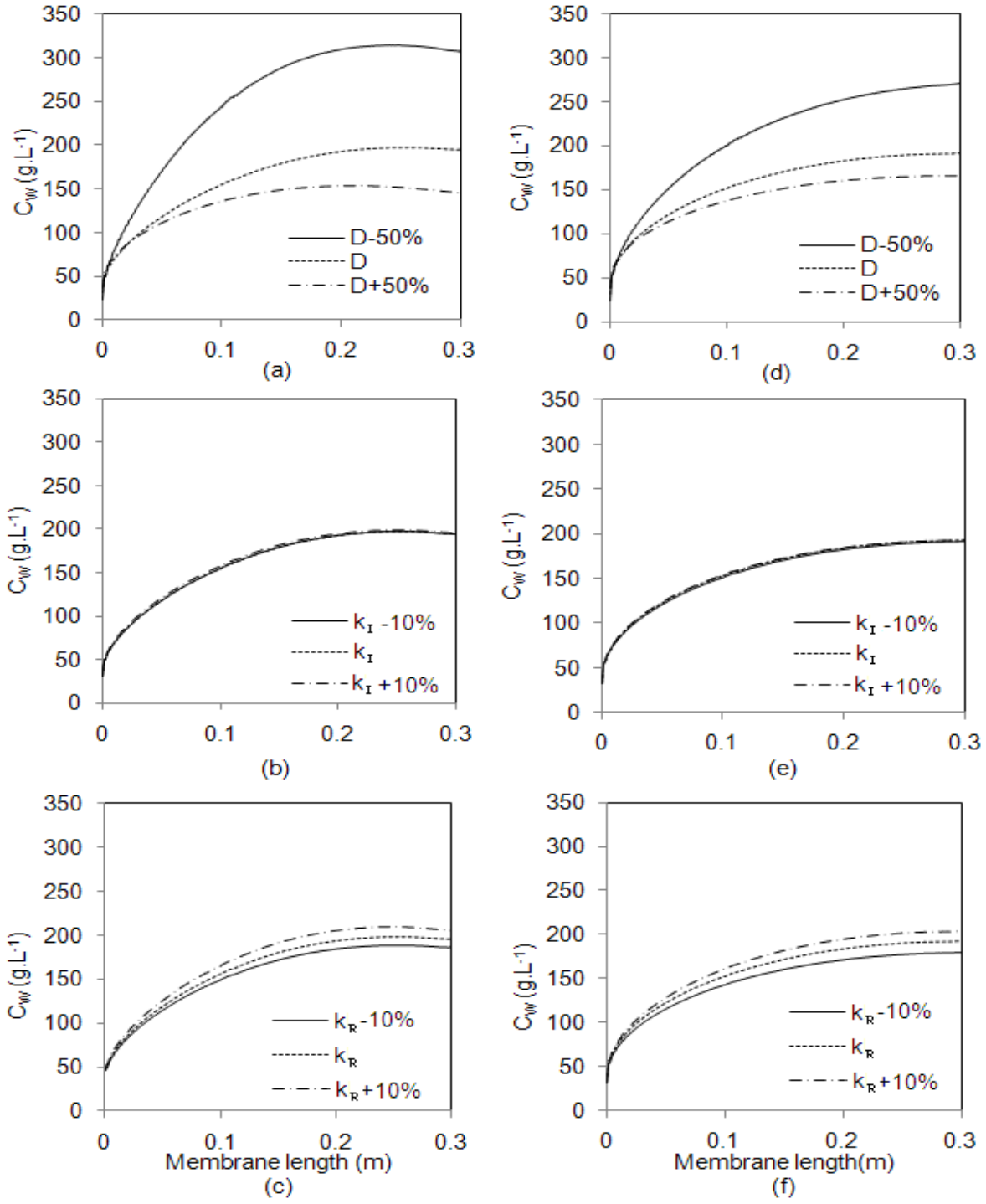

Figure 3.18 Model sensitivity analysis for the estimated protein concentration at the membrane surface of the non-electroacidified (a; b; c) and electroacidified (d; e; f) soy protein extract; TMP= 34.5 kPa; axial velocity = 1 m.s^{-1}; t = 4050 and 5760 s for the non-electroacidified and electroacidified soy protein extracts

3.5 Conclusion

Computational Fluid Dynamics (CFD) provided an attractive tool for the modeling of the complete sequence, feed tank and hollow fiber ultrafiltration unit. A model was developed to investigate the transient permeate flux and protein concentration and the spatial fouling behavior during the concentration of soy protein extracts by membrane ultrafiltration and subjected to electroacidification. The CFD model solved the transient equations of motion and continuity in 2-D cylindrical coordinates. A new transient two-component fouling resistance model based on the local pressure difference, permeate velocity and protein concentration and fitted from experimental data was implemented in the resistance-in-series flux model to describe the dynamics of the reversible and irreversible fouling during the filtration. The concentration dependency of the viscosity of the solution and the effect of electroacidification were considered in the model development and shown to affect significantly the estimated protein concentration at the membrane surface. The model provided an accurate prediction of the experimental permeate flux, the protein concentration and the fouling dynamics during the concentration operation. In particular, the model was able to estimate accurately each of the transient reversible and irreversible fouling resistances and the contribution of electroacidification, a limitation of many models previously published. The model shows a uniform bulk protein concentration along the fiber but spatially non-uniform protein concentration profile near the membrane surface where the concentration gradient is high. The model estimates show that a moderate increase of the permeate velocity can be achieved when increasing the axial velocity. In contrast, increasing the TMP increases more substantially the permeate flux. Experimental results showed that polarization layer is not the only phenomenon affecting the permeate flux decrease at the beginning of the filtration; the irreversible fouling is an important factor to be considered for the concentration of soy protein extracts. The irreversible fouling at the beginning of the filtration contributes to 20% and 40% of the total fouling for non-electroacidified and electroacidified soy protein extracts, respectively. The model estimates suggest that the irreversible fouling is associated with protein adsorption since a plateau is estimated for both types of extracts. Therefore, the improvement of the concentration of soy protein extracts subjected to electroacidification will be achieved by manipulating the interactions leading to irreversible fouling, ie between the proteins and the membrane surface. The model sensitivity analysis showed that the viscosity of the soy protein solution is a sensitive parameter and the

concentration dependant viscosity changes significantly the profile of the protein concentration at the membrane surface. The concentration at the membrane surface is also much more sensitive to the diffusion coefficient for the non-electroacidified soy protein suggesting that protein back transport associated with the diffusion coefficient plays a more important role. Future work will focus on the interaction between the proteins and the membrane surface as well as the contribution of the minerals in these interactions. The role of the diffusion coefficient will also be further examined.

Chapter 4

Mathematical Modeling of Osmotic Pressure and Diffusion Coefficient of BSA and Soy Glycinin

Overview

Colloidal interactions influence the transport properties, such as viscosity and diffusion coefficient, and the thermodynamic properties such as osmotic pressure. These properties play vital roles in membrane filtration processes because they control the distribution of particles in the vicinity of the membrane surface, often influencing the permeation rate. Therefore, understanding the behavior of these properties is of great importance in addressing questions about membrane fouling. Osmotic pressure and diffusion coefficient of the proteins bovine serum albumin (BSA) and glycinin, one of the major storage proteins in soy, were modeled considering the particle-particle interactions; Electrostatics, London-van der Waals, and hydration forces along with entropy pressure. A hexagonal Wigner-Seitz cell model including the numerically solved nonlinear Poisson-Boltzmann equation was used to calculate the electrostatic forces. Ionic strength, pH, protein concentration, and thermodynamical properties of the protein were considered in the model to calculate osmotic pressure and diffusion coefficient without any adjustable parameter. Since osmotic pressure was calculated through a complicated mathematical model, obtaining a simple equation for osmotic pressure as a function of pH, ionic strength, and protein concentration was of great interest. Due to the inherent nonlinearity of the problem, an Artificial Neural Networks (ANN) tool was used to analyze the estimated data in order to find the relation.

For both proteins, results showed that osmotic pressure increases as pH diverges from the protein isoelectric point. Increasing the ionic strength, however, tends to reverse the effect by shielding charges, causing molecular contraction and thereby decreasing the osmotic pressure. Results also showed that osmotic pressure is more sensitive to the ionic strength as pH diverges from the isoelectric point of the protein. Two different trends were found for diffusion coefficient at specified pH and ionic strength values, diffusion coefficient values that decrease with protein concentration and diffusion coefficient values that pass through a maximum. When zeta potential of the protein is low, either at high ionic strength or at pH close to the protein isoelectric point, diffusion coefficient decreases with protein concentration and no maximum is observed. Simulated results for BSA were compared with experimental results and good agreement was found. The osmotic pressure of soy glycinin was found much smaller than that of BSA for all the

pH, ionic strength, and protein concentration range due mostly to the size of the protein molecule.

4.1 Introduction

A colloidal system consists of a large number of small particles in a suspending fluid. The particles are in a size range of 1-1000 nm that covers a large number of proteins, the size range however is arbitrary [34,64]. Particles interact with one another in the course of their Brownian motion. Because of the motion of the particles, interactions between particles occur million of times per second even in dilute solution. These interactions could be either attractive or repulsive depending on the nature of the solution and the particles. The resulting interactions have a profound effect on the properties of the solution such as viscosity, diffusion coefficient, and osmotic pressure.

Osmotic pressure and diffusion coefficient of particles are of importance in membrane filtration processes because they control the solute accumulation on the membrane surface and consequently the permeate flux decline. Therefore, accurate prediction of these parameters is of vital importance in estimating the permeate flux during the filtration process. Osmotic pressure arises when two solutions of different concentrations are separated by a semi-permeable membrane. During protein ultrafiltration process for example, permeable solvent passes through the membrane because of the trans-membrane pressure (TMP) driving force resulting in a solution with higher concentration of protein on the feed side of the membrane (side with higher pressure) than that of the permeate side (side with lower pressure). Permeable solvent tend to migrate back from the permeate side with a low solute concentration to the feed side of the membrane with a high solute concentration, to keep both sides of the membrane at the same chemical potential of the solutes. The pressure required to prevent the back migration of the solvent is known as the osmotic pressure [17]. Therefore, TMP confronts a back pressure, osmotic pressure, during the filtration which lowers the efficiency of the filtration process. Osmotic pressure is frequently ignored in the permeate flux calculation at a typical protein concentration of the feed solution (5-50 $g.L^{-1}$) due to its negligible value compared to TMP [65].

However, osmotic pressure may become important with the effect of concentration polarization at the membrane surface.

In chapter 3, the ultrafiltration process of soy protein extracts was simulated neglecting the osmotic pressure and assuming a constant value for diffusion coefficient of soy proteins in the solution. Lack of experimental data for osmotic pressure and diffusion coefficient of soy proteins motivated us to develop a mathematical model considering the particle-particle interactions. This mathematical model was initially applied to bovine serum albumin (BSA) for which the experimental data was available in literature. Good agreement between the model prediction and the experimental data for BSA was observed. The validated model was then modified for soy glycinin.

A fundamental assumption made in this chapter was rigid spherical proteins with uniform surface charge density. This assumption was made through the DLVO theory and the electrical double layer model [66]. Although this assumption seems to be far from the real picture of dispersed proteins in a solution, good agreement between the theoretical prediction and experimental data for osmotic pressure and diffusion coefficient of BSA was observed.

4.2 Proteins

4.2.1 Bovine Serum Albumin (BSA)

Serum albumins are the most abundant proteins in blood plasma [67]. The albumin has a molecular weight of 66500. BSA was chosen as a model protein in this work because it is well characterized and the physiochemical property of the solution was well studied. The primary structure of BSA and the electrostatic potential distribution around the molecule was plotted using Swiss-pdb viewer version 4.0.1, Swiss institute of bioinformatics, based on the protein data bank ID 1UOR (Figure 4.1)[68,69].

4.2.2 Soy glycinin

Glycinin is one of the major storage proteins in soy and accounts for about 40% of the total seed protein. Glycinin has a hexameric structure with a sedimentation coefficient of 11s. The molecular weight of glycinin is most often reported to be 320,000-380,000 [70,71]. Glycinin consists of 5 different subunits, A1aB1b, A2B1a, A1bB2, A3B4, A5A4B3 [70,76]. Figure 4.2 shows the structure of A1aB1b and A3B4 with protein data bank ID of 1FXZ and 2D5F, respectively. The amino acid sequence of the other subunits are available in the protein data bank (pubmed, National Center for Biotechnology Information, U.S. National Library of Medicine). Physical properties and the distribution of charged amino acids of BSA and soy glycinin are summarized in Table 4.1 and

Table 4.2. Appendix present the structure of the amino acids. According to [72], soy glycinin was prepared as follow: one part of soy flour was hydrolyzed with 5 parts of water at 40 °C for 30 min. The cold insoluble fraction was found to be at least 80 % glycinin by ultra-centrifugation. Samples were dissolved in standard buffer (0.0325 M K2HPO4, 0.0026 M KH2PO4, 0.4 M NaC1, 0.01 M mercaptoethanol, pH 7.6), followed by centrifugation at 38 000 × g for 30 min and then dialysis against chromatography buffer. 5 × 35 cm columns of hydroxylapatite (Biorad, HTP) were packed and equilibrated. The glycinin eluted from hydroxylapatite was concentrated by membrane ultrafiltration and applied to a 2.5 × 100 cm column of Sepharose 6B (Pharmacia Ltd) equilibrated with 1 M KH2PO4, pH 7.6 containing 0.02 ~ sodium azide. The Stokes' radius of glycinin was estimated by gel filtration [72].

Table 4.1 Physical properties of BSA and glycinin

Physical property	BSA [21,73]	Soy glycinin [72]
M_w	66500	320000
$\overline{v_2}$ ($cm^3.g^{-1}$)	0.734	0.730
a_{dry} (nm)*	2.69	4.52
δ_1 (g water/ g protein)	0.26	0.36
*a_{Hyd} (nm)	3.2	5.4
D_B ($m^2.s^{-1}$)	6.7×10^{-11}	3.44×10^{-11}
pI	4.72[74]	6.4 [75]

* Estimated values as explained in the text

Table 4.2 Distribution of charged amino acids of BSA [21] and soy glycinin [70]

Specific amino acid	Total number of specific amino acid (BSA)	Total number of specific amino acid (glycinin)	pKa
Aspartic acid+Glutamic acid (ASP+GLU)	100	320	4.0
Histidine (HIS)	17	49	6.9
Lysine (LYS)	59	108	9.8
Tyrosine (TYR)	19	52	10.4
Arginine (ARG)	23	152	12
Cysteine (CYS)	1	44	8.5

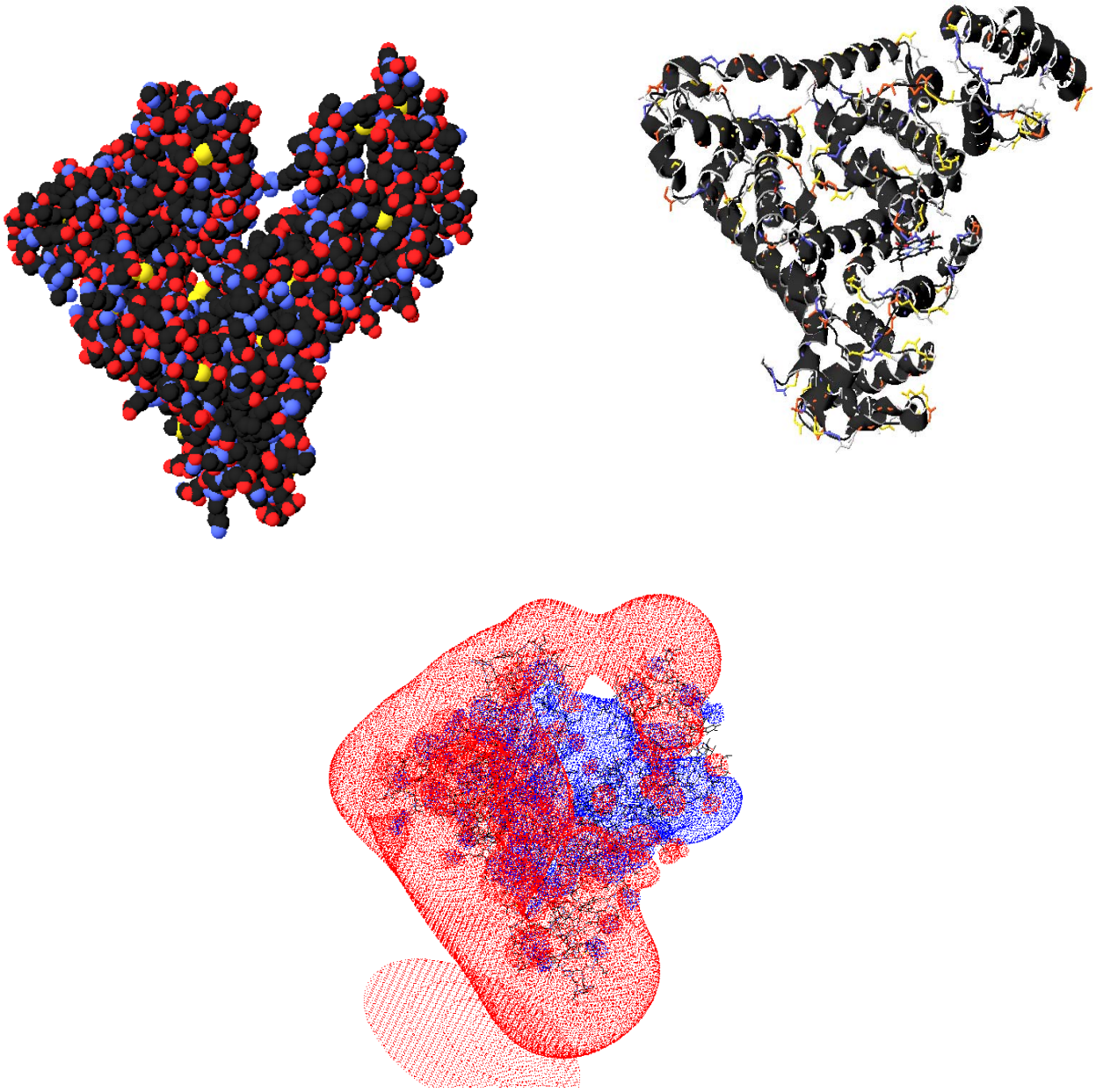

Figure 4.1 Primary structure of bovine serum albumin (top), basic amino acids in blue, acidic amino acids in red, polar amino acids in yellow, and hydrophobic amino acids in black; approximate electrostatic potential (down) around the molecule. Swiss-pdb viewer 4.0.1, Swiss institute of bioinformatics. Pdb ID "1UOR" [68]

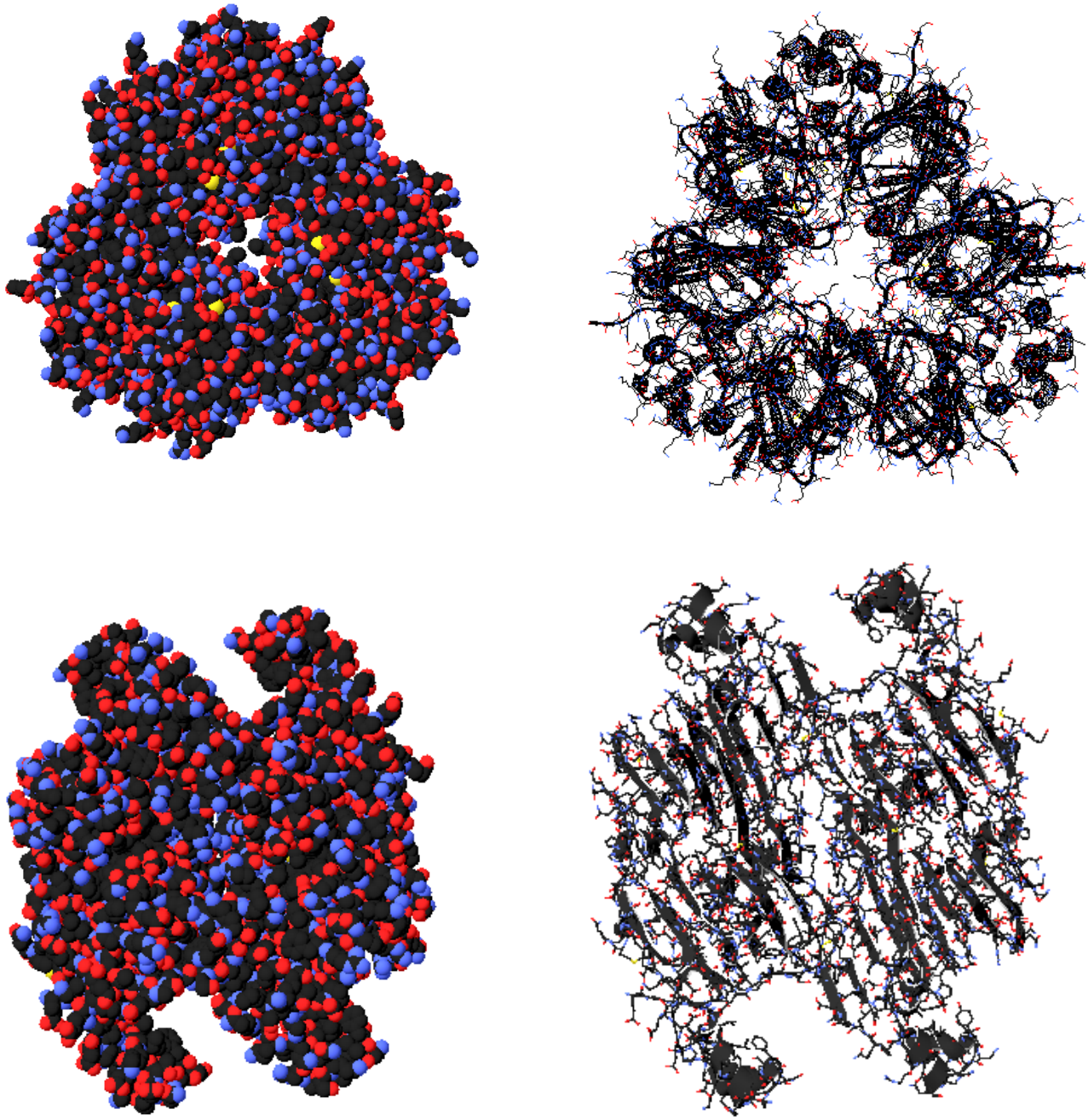

Figure 4.2 Subunit structures of A1aB1b (top, Pdb ID 1FXZ) and A3B4 (down, Pdb ID 1OD5), basic amino acids in blue, acidic in red, polar in yellow, and hydrophobic in black [70,76]; Swiss-pdb viewer 4.0.1, Swiss institute of bioinformatics.

4.3 Osmotic pressure

A thermodynamic relation for osmotic pressure can be derived from the Gibbs free energy equation and the concept of chemical potential (equations 4.1a and 4.1b) [7]. Chemical potential is defined as the free energy change per mole of solute formed, consumed or transferred e.g. from one side of a semi-permeable membrane to another side. With the assumptions of ideal and incompressible solution, van't Hoff's equation can be derived, the applicability of which is limited to dilute solutions (equation 4.2). Another simplification made in deriving equation 4.2 is the approximation of log form of solvent mole fraction by mole fraction of the solutes in a binary system. These assumptions are only valid for dilute solutions. The van't Hoff's equation assumes that osmotic pressure increases linearly with solute concentration. For concentrated solutions, the van't Hoff's equation is modified using virial equations; the coefficients of which can be obtained by fitting the truncated virial equation to the experimental data. According to statistical mechanics, the second virial coefficient corresponds to the interactions between pairs of particles, higher order virial coefficients are associated with larger number of particles [7,64]. Different techniques exist to measure the osmotic pressure experimentally. Osmotic pressure is generally measured with a membrane osmometer consisting of two chambers separated by a semi-permeable membrane (permeable only to the solvent) [77]. The osmotic pressure is considered as the pressure that prevents the solvent to permeate from the dilute side of the membrane to the other side. Another technique to calculate the osmotic virial coefficient is the static light scattering (SLS) method [78]. This method is usually used to obtain the molecular weight of the solute and the second virial coefficient. Experimental data of osmotic pressure for proteins, however, is usually scarce in literature and usually confined to the dilute range.

$$dG = -SdT + VdP + \sum \hat{\mu}_i dn_i \tag{4.1a}$$

$$d\hat{\mu}_i = RT\frac{dP_i}{P_i} \tag{4.1b}$$

$$\pi = \frac{CR^0T}{M_w} \tag{4.2}$$

$$\pi = B_1 C + B_2 C^2 + B_3 C^3 + \cdots \quad (4.3)$$

where G is the Gibbs free energy, T is absolute temperature, S is entropy, $\hat{\mu}_i, P_i \; and \; n_i$ are chemical potential, pressure and molar concentration of component i, V is volume, π is osmotic pressure, C is the solute concentration, R^0 is the gas constant, M_w is molecular weight of the solute, and B_1-B_3 are the virial coefficients.

Another approach to estimate the osmotic pressure is based on the colloidal interactions and the DLVO theory. Bowen et al. developed a method to calculate the osmotic pressure of colloidal dispersion using the extended DLVO theory [21-25]. The method was selected in this work to estimate the osmotic pressure of BSA and soy glycinin. In this method, electrostatics forces, London-van der Waals forces, hydration forces, and entropic effects were considered in the extended DLVO theory (equation 4.4).

$$\pi = \frac{\sqrt{6}}{A_h}(F_{ATT} + F_{ELEC} + F_{HYD}) + P_{ENT} \quad (4.4)$$

where π is the osmotic pressure, A_h is the effective area occupied by the protein at a hypothetical plane (surface of a hexagonal cell, see section 4.5.1 for detail) and is calculated from equation 4.5, F_{ATT} is the attractive force, F_{ELEC} is the electrostatic force, F_{HYD} is the hydration force, and P_{ENT} is the entropic pressure, the descriptions of which are given in section 4.5.

$$A_h = 2\sqrt{3}\left(a + \frac{D_p}{2}\right)^2 \quad (4.5)$$

where a is an effective hard sphere radius of the protein and D_p is the interparticle distance (section 4.5.1).

4.4 Diffusion coefficient

Diffusion coefficient of particles is normally measured experimentally by dynamic light scattering (DLS) method [64]. This method however, fails at high particle concentration. Most of

the experimental data on diffusion coefficient in literature is limited to dilute solutions necessitating a comprehensive mathematical model to represent the behavior of diffusion coefficient at high concentration.

Stokes-Einstein equation (equation 4.6) describes the Brownian motion of a single sphere in a solution, due solely to the thermal fluctuation of the molecular movement around the particles

$$D_B = \frac{KT}{6\pi\mu a} \tag{4.6}$$

where K is the Boltzmann constant, T is the absolute temperature, μ is the fluid viscosity, and a is the particle radius. The Stokes-Einstein equation, however, is unable to predict the diffusion coefficient of concentrated solutions because the effect of neighboring particles was neglected in this equation.

The aim of the present work was to obtain the concentration dependency of the diffusion coefficient for BSA and soy glycinin as a function of physiochemical parameters; pH, and ionic strength. This problem is of great interest in filtration process optimization because diffusion coefficient controls the particle accumulation in the vicinity of the membrane surface. Most of the experimental data on protein diffusion coefficient in the literature is limited to dilute solutions necessitating a comprehensive mathematical model to represent the behavior of diffusion coefficient at high concentration.

Generalized Stokes-Einstein equation (equation 4.7) was used in this work to calculate the diffusion coefficient of the proteins [25,79,80].

$$D(\phi) = D_B \frac{k(\phi)}{S(\phi)} \tag{4.7}$$

where ϕ is the volume fraction of the protein (equation 4.16, section 4.5.1), $k(\phi)$ is the hydrodynamic interaction coefficient, $S(\phi)$ is the osmotic compressibility factor, and D_B is the Brownian diffusion coefficient at dilute solution [24]. The coefficient $k(\phi)$ takes into account

the hydrodynamic effect of the neighboring proteins. The osmotic compressibility factor $S(\phi)$ describes the motion of proteins as a result of osmotic pressure. The parameters $S(\phi)$ and $k(\phi)$ are calculated from equations 4.8 and 4.9 [81].

$$\frac{1}{S(\phi)} = \left[\frac{4\pi a_{Hyd}^3}{3KT}\right]\frac{\partial \pi}{\partial \phi} \tag{4.8}$$

$$k(\phi) = (1-\phi)^{k_D} \tag{4.9}$$

where k_D is hydrodynamic hindrance factor and varies in a range of 7.2-11.9 [73]. Saksena and Zydney [80] obtained the hydrodynamic hindrance factor value of 8.8 to best fit their experimental data and was used in this work for both proteins.

4.5 Interaction forces of proteins

4.5.1 Electrostatic forces

Proteins acquire a surface electric charge when brought into contact with a polar medium due to the ionization of the polar groups of the amino acids or by the adsorption of ions. The charged protein will be surrounded by ions of opposite charge. The acquisition of the surface charge by the protein affects the distribution of the ions in solution. The arrangement of the electric charges on the protein, together with the balancing charge in the solution is known as the electrical double layer (EDL). The importance of the EDL has led to numerous studies, and many models were proposed [34,82,83]. Figure 4.3 shows the modified Gouy-Chapman EDL model around a negatively charged protein [21,34,84]. The electrical double layer is formed by a compact layer of counterions around the protein surface followed by a diffuse layer extending into the bulk solution. Since the charge on the protein is not fully compensated by the compact layer, additional ions are attracted to the surface with weaker electrostatic forces, the distribution of which is given by the Poisson Boltzmann equation (PBE), equation (4.10) [17,85]. At a distance *d,* the transition from the compact to the diffuse layer occurs. The separation between two layers is called outer Helmholtz plane (OHP).

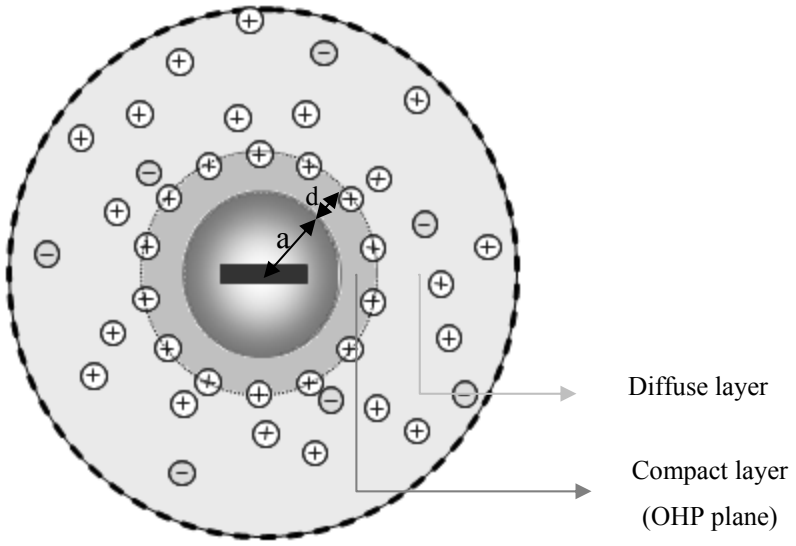

Figure 4.3 Electrical double layer (EDL) in the vicinity of negatively charged protein (modified Gouy-Chapman model)

$$\frac{d^2\psi}{dr^2} + \frac{2}{r}\frac{d\psi}{dr} = \frac{2n^0 Ze}{\varepsilon_0 \varepsilon_{r3}} sinh\left(\frac{ez\psi}{KT}\right) \tag{4.10}$$

Where ψ is the electrostatic potential, r is the radial coordinate, n^0 is the ion number concentration in the bulk, Z is the valency of the salt (ions), e is the elementary charge, ε_0 is the permittivity of vacuum, ε_{r3} is the dielectric constant of water, K is the Boltzmann constant, and T is the absolute temperature.

The electrical double layer of proteins starts to overlap when proteins approach one another. As a result, a repulsive force is formed between the proteins. In a suspension, the electrical double layer of each protein overlaps with that of neighboring proteins. Therefore, the interaction energy depends not only on one protein but also on the configuration of many proteins. The multi-particle interaction nature of the colloid can be taken into account using a cell model which is also known as Wigner and Seitz model [22]. Each cell is presumed to be comprised of a single protein surrounded by a shell of fluid. A hexagonal close packed cell model similar to that of Bowen and Jenner [22] was used in this work to describe the electrical double-layer interactions of the colloid (Figure 4.4). There is considerable evidence that electrostatically stabilized dispersions exist in a hexagonal packing form of minimum energy [22]. The charge distribution

of the counterions in the diffuse layer is described by PBE, equation 4.1. The expression for the repulsive force between proteins at a distance D_p, is given by equation 4.11 [22,86].

$$F_{ELEC} = \frac{1}{3} S_\beta n^0 KT \left(cosh \frac{Ze\psi}{KT} - 1 \right) \tag{4.11}$$

where S_β is the outer cell surface and is calculated by equation 4.12 for hexagonal close packed arrangements. Electrostatic potential, ψ, was obtained by solving the PBE numerically with the finite element methods (FEM) using COMSOL Multiphysics (version 3.5). Zeta potential at the hydrodynamic radius of the protein and $\frac{d\psi}{dr} = 0$ at $r=r_{cell}$ were assumed as the boundary conditions to solve the PBE [21]. The hydrodynamic radius was assumed to be the protein hydrated radius and the compact layer. The thickness of the compact layer, *d*, was taken to be the value of the hydrated counterion radius [21]. For sodium ions, the most probable value for the hydrated counterion radius is 0.23±0.02 nm [23,87]. Zeta potential of the protein was calculated based on the charge regulation model which will be explained in details later on. The second boundary condition stands for the electroneutrality at the cell surface.

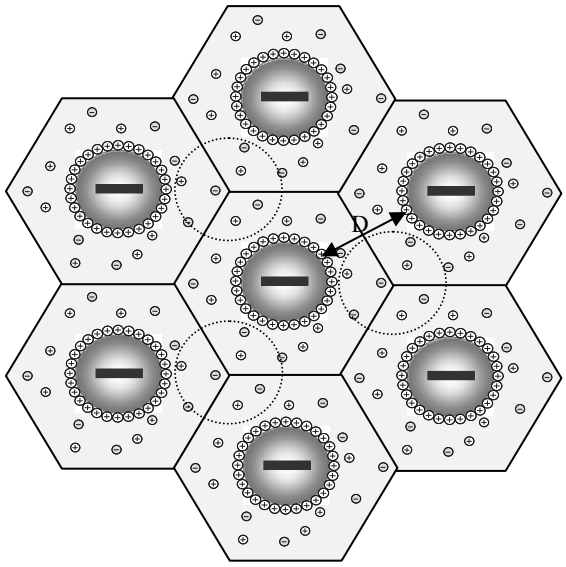

Figure 4.4 Schematic representation of a hexagonal packed array of spherical proteins, showing the three adjacent neighbors in the contiguous layer (broken circle)

$$S_\beta = \left(\sqrt{3} + 2\sqrt{2}\right)\left(2a + D_p\right)^2 \tag{4.12}$$

where a is the effective hard sphere protein radius, D_p is the interparticle distance calculated from equation 4.13, and r_{cell} is the radius of a volume-equivalent sphere for the aforementioned hexagon (equation 4.14).

$$D_p = \frac{\left(a_{Hyd}\right)}{\left(\frac{3\phi}{4\sqrt{2\pi}}\right)^{\frac{1}{3}}} - 2a \tag{4.13}$$

$$r_{cell} = \left(2a + D_p\right)\left(\frac{3}{4\pi\sqrt{2}}\right)^{1/3} \tag{4.14}$$

The parameter ϕ is the volume fraction of the protein and is calculated from equation 4.15[21]

$$\phi = \frac{C\overline{v_2}(a+d)^3}{a_{dry}^3} \tag{4.15}$$

where C and $\overline{v_2}$ are the protein concentration and the specific volume of the protein, respectively. Accurate knowledge of the effective hard-sphere particle size, a, is required to predict the interaction. The dry radius of the protein can be estimated if the molecular weight M_w and the specific volume of a pure sample of the protein, v, are known (equation 4.16). The molecular volume of a protein inside a solution containing the bound water can be calculated from equation 4.17.

$$a_{dry} = \left(\frac{3}{4\pi}\frac{M_w}{N_A}v\right)^{1/3} \tag{4.16}$$

$$v_h = \frac{4}{3}\pi a^3 = \frac{M_w}{N_A}\left(\overline{v_2} + \delta_1\overline{v_1}\right) \tag{4.17}$$

where v_h is the molecular volume of the hydrated protein, $\overline{v_1}$ is the specific volume of the solvent (usually water), $\overline{v_2}$ is the specific volume of the dry protein, and δ_1 is the number of grams of bound water per gram of protein to form a monolayer over the dry protein particle [21,73].

Charge regulation model

Charge regulation (CR) model was used in this work to estimate the protein surface charge. The model necessitates the type and number of the amino acid groups that take part in ionization and also the amount of ions adsorbed on the protein surface [21]. In charge regulation model, particles' surface potential changes when surface of proteins approach one another [88].

Figure 4.5 represents a flowchart for the charge regulation model [21,34]. The model starts with initial estimates of the potential at the hydrodynamic radius, zeta potential, and then continues with solving the PBE (equation 4.10) based on the boundary conditions. Based on the modified Gouy-Chapman model the compact layer around the protein is free of charge [34], therefore the charge density at the protein surface (σ_0) equals the charge density at the OHP distance (σ_d) (equation 4.18). According to the charge density definition and the relation between potential and charge density, equation 4.19 can be derived [34].

$$\sigma_d = -\sigma_0 \tag{4.18}$$

$$\sigma_d = \varepsilon_0 \varepsilon_r \left.\frac{d\psi}{dr}\right|_{r=a_{hyd}} \tag{4.19}$$

At thermodynamic equilibrium, the Poisson Boltzmann equation relates ion concentrations to the electrostatic potential (equation 4.20) [89].

$$[H^+]_s = [H^+]_{bulk} e^{\left(\frac{-ze\psi_0}{KT}\right)} \tag{4.20}$$

where $[H^+]_s$ is the hydrogen ion concentration at the protein surface, $[H^+]_{bulk}$ is the bulk hydrogen ion concentration which is calculated from the pH of the solution, and ψ_0 is the surface potential of the protein. The surface potential of the protein is calculated from equation 4.21.

This equation represents the potential drop across the compact layer due to the capacitance of the fluid [34].

$$\psi_0 = \frac{\sigma_0 ad}{\varepsilon_0 \varepsilon_r (a+d)} + \psi_d \tag{4.21}$$

Equations 4.22 and 4.23 illustrate the equilibrium ionization for aspartic acid or glutamic acid. The fraction of the carboxyl group and the number of surface charges generated on the protein due to the ionization of the carboxyl group are calculated through equations 4.24 and 4.25. Similar calculation is performed for other charged amino acids and the total surface charge on the protein surface due to acid-base equilibria is calculated (equation 4.26). To solve these equations, the pKa of the amino acids is required (

Table 4.2). As explained earlier, the surface charge of the protein is due to ionization of the amino acids and also ion adsorption (such as chloride binding) on the protein surface. Therefore, the total surface charge is calculated using equation 4.27.

$$-COOH \overset{K_1}{\leftrightarrow} COO^- + H^+ \tag{4.22}$$

$$k_1 = \frac{[COO^-][H^+]_S}{[COOH]} \tag{4.23}$$

$$X_{COO^-} = \frac{[COO^-]}{[COOH] + [COO^-]} \tag{4.24}$$

$$Z_{COO^-} = X_{COO^-} \times [Total\ number\ of\ carboxyl\ group\ on\ the\ protein\ surface] \tag{4.25}$$

$$Z_{AB} = \sum Z^+ - \sum Z^- \tag{4.26}$$

$$Z_T = Z_{AB} - Z_{Cl^-} \tag{4.27}$$

Since the total number of surface charge is known, an updated charge density is calculated with equation 4.28. The new charge density value is compared to the previously calculated value, equation 4.18. The calculation terminates when the relative percent error between the two charge density estimates was less than 10^{-5}.

$$\sigma_{0new} = \frac{Z_T e}{4\pi a^2} \tag{4.28}$$

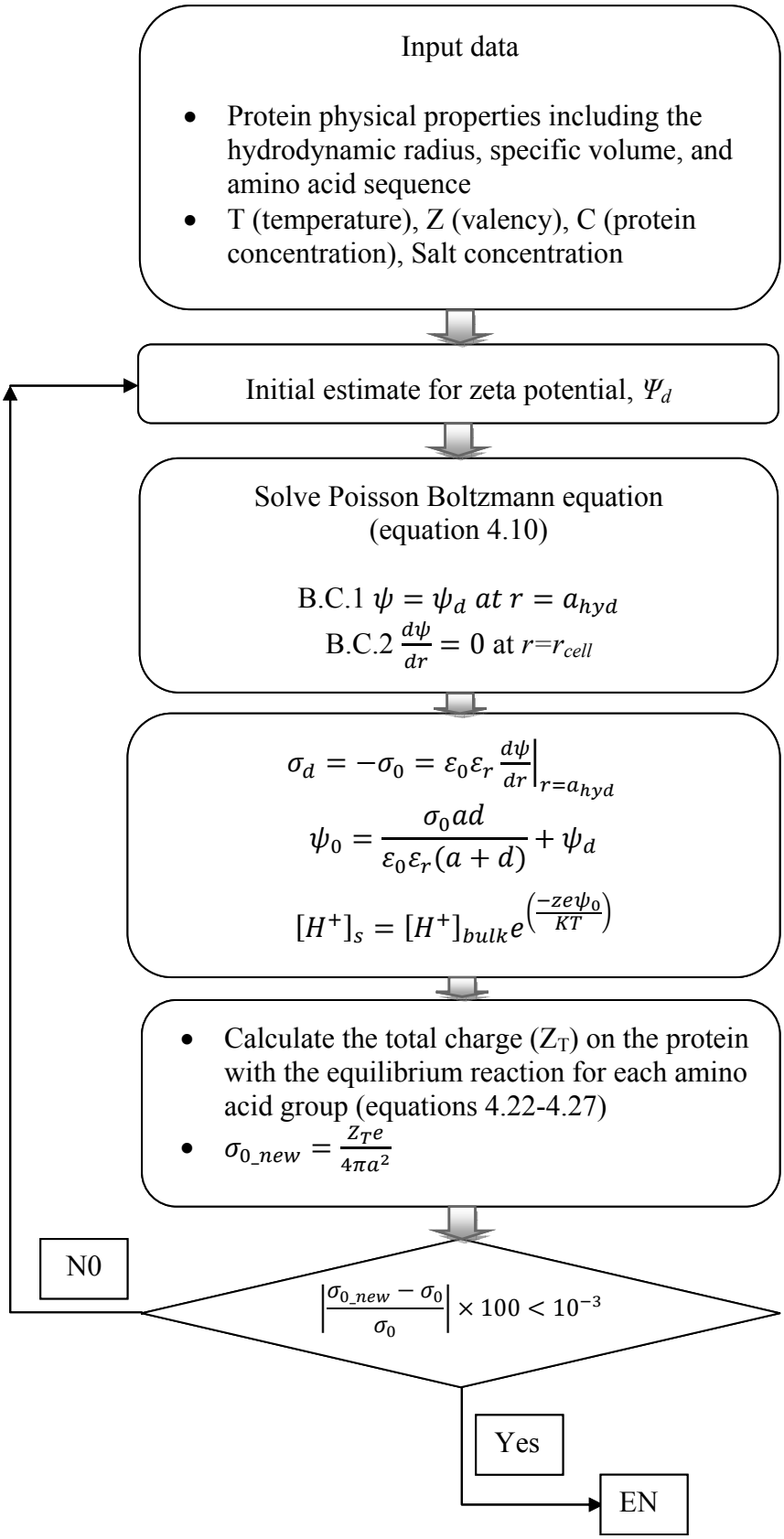

Figure 4.5 Charge regulation model flowchart

4.5.2 London-van der Waals forces

Molecules in close proximity induce charge polarization due to the electromagnetic fluctuations. These forces grouped as London-van der Waals forces are inherently attractive. These attractive forces can become effective when the surfaces approach one another. Hamaker [36] introduced a simple procedure for calculating these attractive forces considering quantum mechanics. According to quantum mechanics, the London-van der Waals energy between any two atoms is proportional to $\frac{H}{(D_p+2a)^6}$ in which H, is the Hamaker constant dependent on the polarizability of the atoms. The total attraction energy is obtained by considering this attraction energy between an atom and a nearby surface and by integrating this equation over the volume of each atom. Equation 4.29 represents the London-van der Waals energy between two similar size spherical proteins with their centers a distance (D_p+$2a$) apart.

$$V_A(D_p) = -\frac{H}{6}\left[\frac{2a^2}{{D_p}^2 + 4aD_p} + \frac{2a^2}{(D_p + 2a)^2} + ln\left(1 - \frac{4a^2}{(D_p + 2a)^2}\right)\right] \tag{4.29}$$

Hamaker constant can be evaluated from the refractive index of the protein in solution and Lorenz-Lorentz equation [23,90-92]. At last, the force between two proteins is calculated from the interaction energy expression (equation 4.30).

$$F_{ATT} = -\frac{dV_A}{dD_p} \tag{4.30}$$

4.5.3 Hydration forces

Other repulsive forces between proteins are the hydration forces. The origin of these forces is believed to be electron acceptor-electron donor interactions, often referred to as polar interactions. Strong polar interactions orient water molecules adsorbed on the surface of proteins, and thus the stability of the colloidal system is conferred by those hydrated water molecules that force the two proteins apart at contact. Such polar forces could be comparable to the van der Waals attractive or electrostatic repulsive, energies at close range. Equation 4.31 expresses the hydration force, the coefficients of which were obtained by fitting an equation to the

experimental data measured for silica [22,93]. This equation was used in this work to estimate the hydration force between protein molecules notwithstanding the fact that this equation might result in an error in the results (see the results section to see the sensitivity of the total force to the hydration force). The only parameter assumed to change in the calculations for different protein molecules was the effective hard sphere radius (a) as it was found by Grabbe and Horn [93] that neither the surface treatment of silica nor the ionic strength can affect this force.

$$F_{HYD} = \pi a \left[F_1 e^{\left(\frac{-D_p}{D_1}\right)} + F_2 e^{\left(\frac{-D_p}{D_2}\right)} \right] \tag{4.31}$$

F_1=0.14 J.m^{-2}, D_1=0.057×10^{-9} m

F_2=5.4×10-3 J.m^{-2}, D_2=0.48×10^{-9} m

4.5.4 Entropic pressure

Entropy accounts for the randomized distribution of the proteins in a liquid suspension. Hall [94] derived an equation of state for rigid spheres within the fluid for a full range of particle concentration (equation 4.32). This equation was obtained by fitting the Padé approximant to the first six virial coefficients. The coefficients of the virial equation were obtained by Kolafa et al. [95] using molecular dynamics.

$$\frac{P_{ENT}}{KT} = \left(\frac{3\phi}{4\pi(a+d)^3}\right)\left(\frac{1+\phi+\phi^2-0.67825\phi^3-\phi^4-0.5\phi^5-X\phi^6}{1-3\phi+3\phi^2-1.04305\phi^3}\right) \tag{4.32}$$

$$X = 6.028e^{[Y(7.9-3.9Y)]}$$

$$Y = \frac{1}{6}\pi\sqrt{2} - \phi$$

4.6 Artificial Neural network

From the engineering points of view, it is always of a great interest to model a dependant variable as a function of independent variable with a simple equation. Since osmotic pressure is

estimated with a complex mathematical procedure, as discussed earlier, it would be very efficient and time effective to develop a simplified mathematical representation of the estimated osmotic pressure according to pH, ionic strength, and concentration. An Artificial Neural Networks (ANN) technique was used for this purpose.

ANN has been inspired from the information process mechanisms of the brain. The network is trained through some datasets and then the network acts as an expert to predict the response for new data sets. The neural network can be considered as a black box, transforms an m-variable input into n-variable output [96].

Figure 4.6 illustrates the simplest architecture of a network which was selected for this work. The model contained one hidden layer. Each neuron was connected to the input and output by a corresponding weight. The inputs of each neuron were multiplied by their corresponding weight and the product was then summed together and applied to the transfer function to create the output. No need for a more complicated architecture of network was found because the simple architecture was able to cover the whole data set.

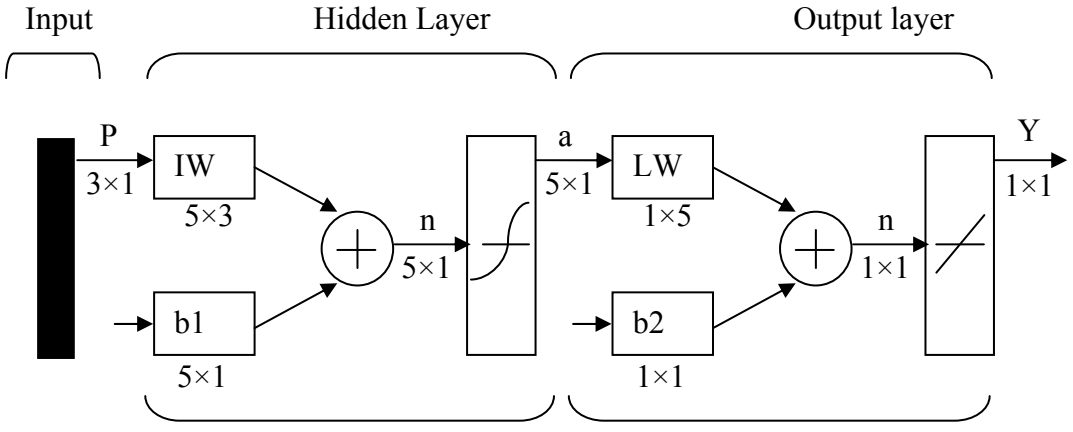

$$a = tansig(IW \times P + b1) \qquad Y = purelin(LW \times a + b2)$$

Figure 4.6 Architecture of the artificial neural network ANN) selected in this work

The network receives 3 independent variables (P), each variable associated with 5 input neuron weights (IW) and 1 bias neuron (b1). The trained matrix, a, is subjected to layer weights (LW)

and the bias matrix, b2. The back-propagation (BP) technique, an iterative search method, was used to modify the weights from the output layer back to the input layer in each run until the mean squared error (MSE) was less than 0.005.

Matlab software version 7 from Mathworks, Natick, Massachusetts was used for the ANN modeling. The Levenberg-Marquardt optimization algorithm (trainlm) was the back propagation technique selected for training the network. The algorithm is the fastest back propagation algorithm in Matlab toolbox. The hyperbolic tangent sigmoid (tansig) and the linear functions (purelin) were the transfer functions for the hidden and the output layers, respectively. The training set was selected randomly from the available osmotic pressure data (75% of the whole data) to cover the whole range of pH, ionic strength, and protein concentration.

4.7 Results and discussion

4.7.1 Bovine serum albumin (BSA)

As was explained in section 4.5.1, accurate knowledge of the effective hard-sphere protein size is required to predict the interparticle interactions. The properties of BSA are presented in Table 4.1. Dry hard-sphere BSA radius may be calculated 2.69 nm (equation 4.16). Equation 4.17 gives an effective hard-sphere particle radius, *a*, of 2.97 nm (2.69+0.28 nm) for BSA inside a solution containing the bound water. The hydrodynamic radius of BSA, a_{hyd}, was taken as the effective hard sphere radius plus the distance to the OHP (see section 4.5.1). Therefore, the hydrodynamic radius of BSA can be calculated as 3.2 nm. According to the charge regulation model in section 4.5.1, the type and number of the amino acids of BSA and the amount of ions adsorbed on the BSA surface should be known to calculate the surface charge. Previous studies indicate that sodium binding to BSA is unimportant but chloride binding occurs [97]. Scatchard et al. developed the chloride binding model for BSA [98].

4.7.1.1 Zeta potential

Zeta potential of BSA was estimated for a large range of pH and ionic strength applying the charge regulation model. Sodium chloride was assumed to be the only salt in the solution.

Results are shown in Figure 4.7. BSA surface carries a positive net charge at pH lower than its isoelectric point and a negative net charge at pH higher than the isoelectric point. At the isoelectric point, the surface net charge and consequently zeta potential are zero. The estimated isoelectric point for BSA (Figure 4.7) varies between 4.5 and 5.2 depending on the ionic strength of the solution. The experimental isoelectric point for BSA in 0.15M NaCl solution was reported to be 4.72 [74] which agrees with the estimated value of 4.76 in this work. Results show that zeta potential is dominated by the effect of pH and is influenced to a lesser extent by the ionic strength. It is also observed that the effect of pH on the zeta potential becomes more important at low ionic strengths. The calculated zeta potential of BSA at ionic strength of 0.03M in sodium chloride solution was also verified with experimental data [21].The calculated zeta potential shows good agreement with the experimental data.

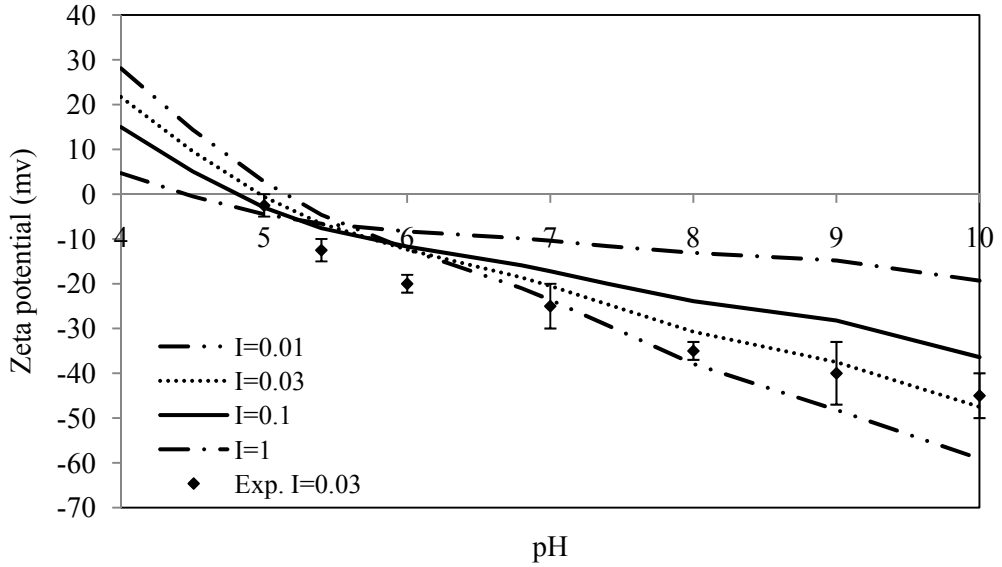

Figure 4.7 Estimated zeta potential for BSA at various ionic strength (I((M)) using charge regulation model (protein concentration of 20 $g.L^{-1}$)

The net charge on proteins depends not only on the pH and ionic strength of the surrounding fluid, but also on the proximity of the protein surfaces [88,99]. Protein concentration affects the ion distribution in the solution surrounding the protein. Table 4.3 shows the effect of BSA concentration on the electrostatic force (F_{ELEC}) and potential ($\boldsymbol{\psi}$) at different distances from the protein. According to equations 4.13 and 4.14, interparticle distance and consequently the

hypothetical cell size decreases when protein concentration increases. As a result, the surface of the hypothetical cell encompassing the protein approaches the protein surface which leads to a higher cell potential ($\boldsymbol{\psi_s}$) and electrostatic force. Results show that the absolute value of the zeta potential remains constant up to protein concentration of 230 $g.L^{-1}$ and then increases with concentration. As was expected, potential is the maximum on the protein surface and decreases with distance from the protein surface.

Table 4.3 BSA potential (ψ), and electrostatic force (F_{ELEC}) at the hexagonal cell surface as a function of concentration at pH=7 and ionic strength of 0.1 M.*

BSA concentration ($g.L^{-1}$)	$\boldsymbol{\psi_0}$ (mV)	$\boldsymbol{\psi_d}$ (mV)	$\boldsymbol{\psi_S}$ (mV)	F_{ELEC} (N)
4	-23.83	-17.2	-9.55×10^{-30}	0.00
40	-23.83	-17.2	-3.00×10^{-10}	4.64×10^{-18}
100	-23.83	-17.2	-1.36×10^{-5}	3.56×10^{-15}
150	-23.96	-17.3	-6.15×10^{-4}	3.79×10^{-14}
230	-24.09	-17.5	-2.33×10^{-2}	3.60×10^{-13}
340	-25.35	-18.9	-0.356	1.97×10^{-12}
450	-28.36	-22.3	-2.12	6.26×10^{-12}

4.7.1.2 London-van der Waals attraction forces

According to equation 4.29, London-van der Waals attraction forces are proportional to the Hamaker constant, a measure of the dielectric properties of the proteins when interacting with the solvent. Figure 4.8 represents the attraction energy and the Hamaker constant of BSA evaluated from the refractive index data for BSA in the solution using Lorenz-Lorentz equation [23,90-92]. Results in Figure 4.8 show that Hamaker constant and therefore the absolute value of London-van der Waals forces depend on the chemical nature of the solution and increase with BSA concentration. At high BSA concentration, the attraction energy has a large negative value; consequently, the attraction energy predominates at high protein concentration. Results also reveal that Hamaker constant is very small at high ionic strength due to the ion shielding effect. Therefore, ionic strength can increase the stability of the protein inside the solution by lowering the attraction force between protein molecules [91].

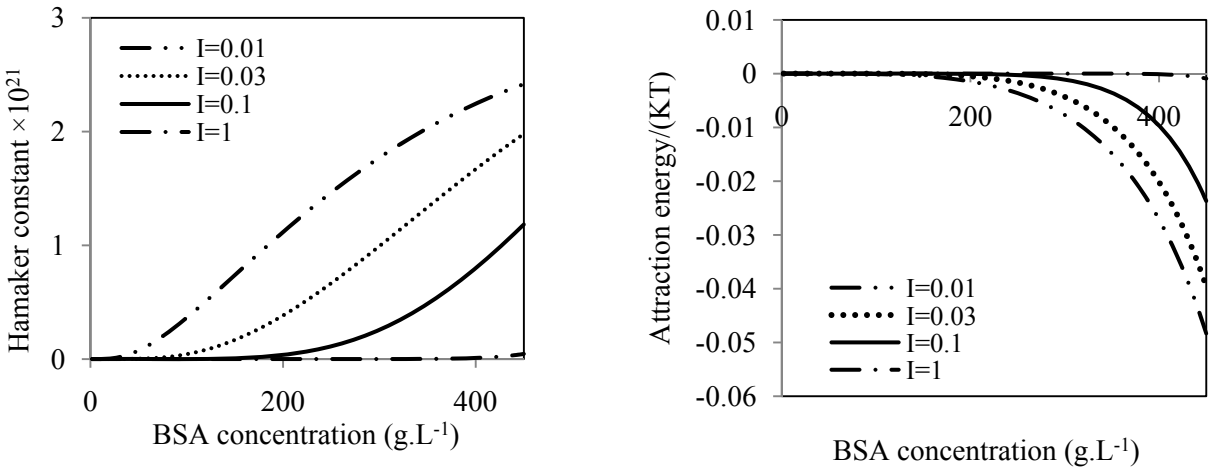

Figure 4.8 Effect of BSA concentration on the Hamaker constant (left) and the London-van der Waals energy (right) at various ionic strengths (I(M))

4.7.1.3 Osmotic pressure

Osmotic pressure of BSA as a function of protein concentration was calculated at different pH and ionic strength values [21,22,25] and is shown in Figure 4.9. At pH close to the isoelectric point of BSA, the net charge on the protein is small. Therefore, electrostatic repulsion and osmotic pressure is low. Osmotic pressure increases as pH diverges from the isoelectric point. Increasing the ionic strength, however, tends to reverse the effect by shielding charges, causing molecular contraction and thereby decreasing the osmotic pressure. These results agree well with those reported in literature [21,74]. Results in Figure 4.9 also show that osmotic pressure becomes more sensitive to the ionic strength as pH diverges from the isoelectric point of BSA.

Based on the DLVO theory, total interaction force between two protein molecules is treated as a combination of attractive and repulsive forces. Negative and positive values represent the attraction and repulsion forces, respectively. The magnitude of the different contributions is affected by the protein concentration, protein type, and physiochemical properties of the suspension. Figure 4.10 and Figure 4.11 represent the contribution of each force term in the osmotic pressure relation (equation 4.4) for BSA at 0.15M NaCl. The predicted osmotic pressure of BSA was compared to the experimental data reported by Vilker et al. [74]. Good

agreement between the theoretical calculation and experimental data was observed. Results also revealed that the hydration force is negligible compared to the other forces and can be neglected in the model calculations. This analysis also indicates that, the attraction force plays a role only at high BSA concentrations. For BSA concentrations less than 400g.L^{-1}, the osmotic pressure is controlled by the entropic and electrostatic force effects.

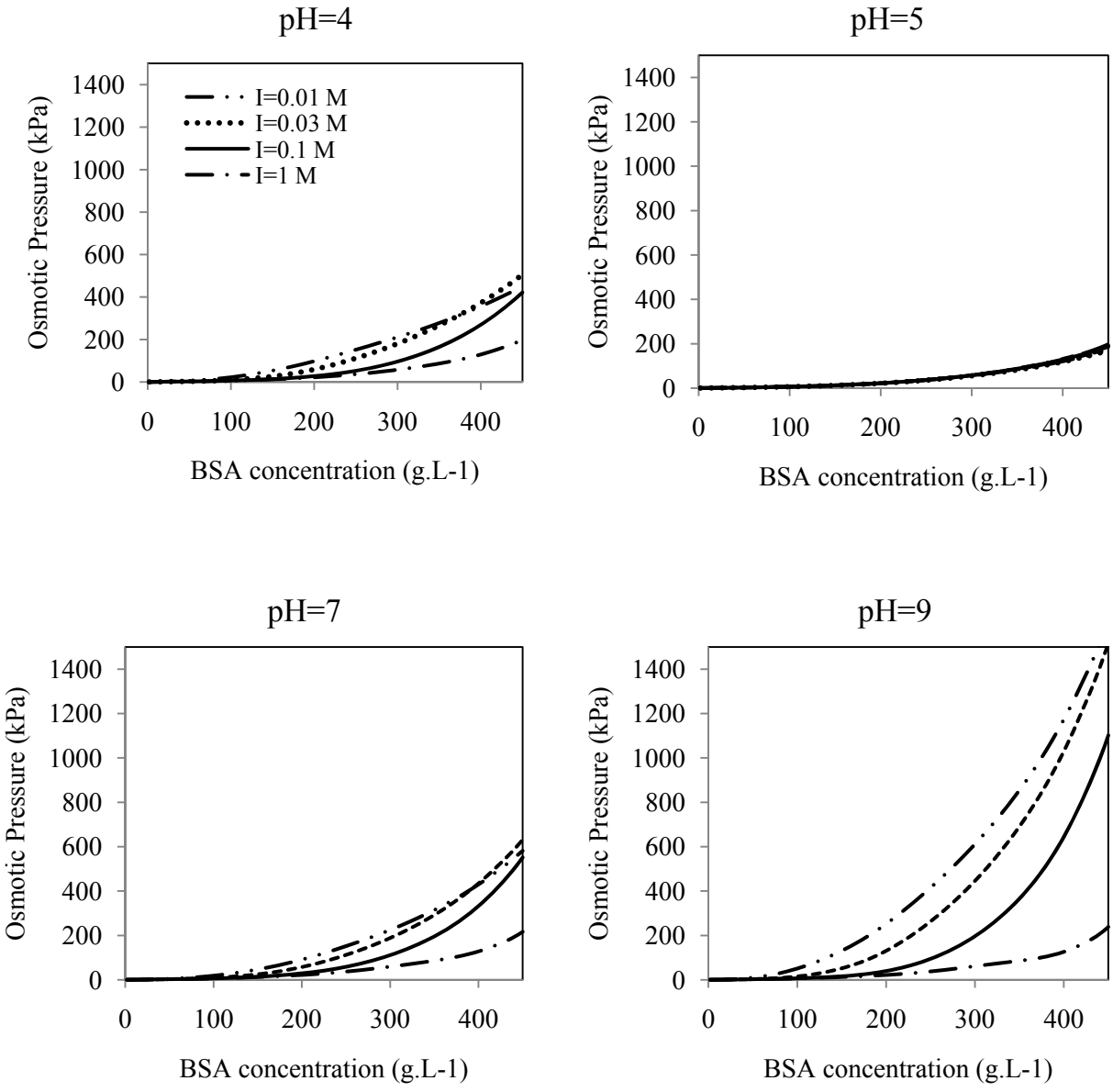

Figure 4.9 Estimated osmotic pressure of BSA according to pH and ionic strength (I(M))

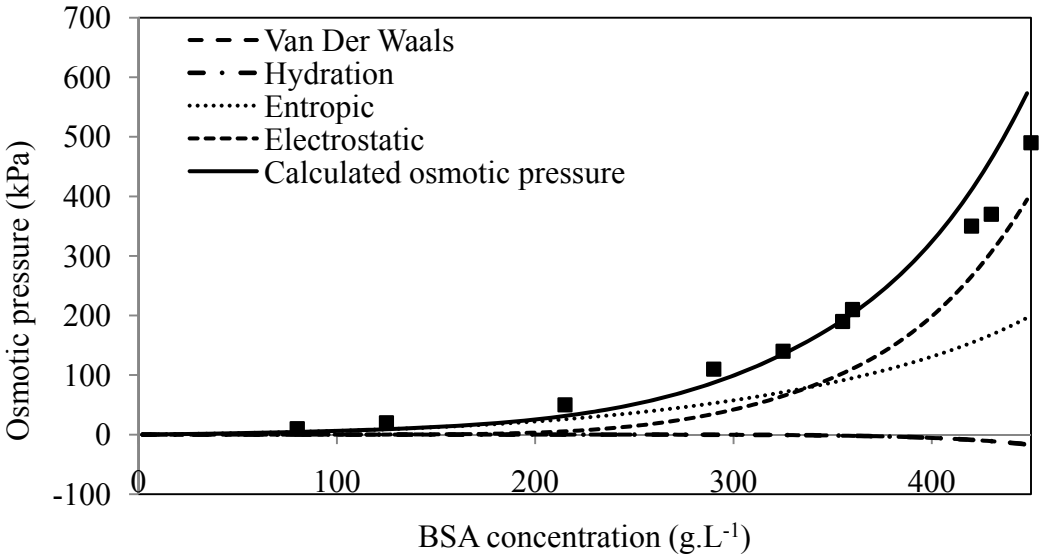

Figure 4.10 Estimation of forces for BSA at pH 7.4 and ionic strength of 0.15M. Experimental data extracted from[21]

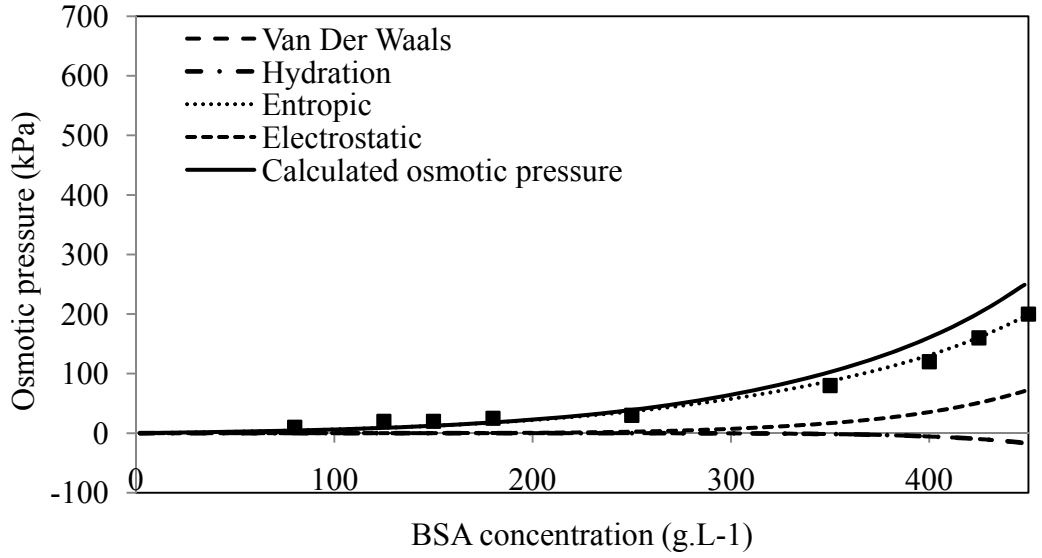

Figure 4.11 Estimation of forces for BSA at pH 5.4 and ionic strength of 0.15M. Experimental data extracted from[21]

4.7.1.4 Diffusion coefficient

The effect of concentration on the dimensionless diffusion coefficient of BSA at various pH and ionic strength is shown in Figure 4.12. Diffusion coefficient was calculated from equations 4.7-4.9. Two different trends were observed; diffusion coefficients that pass through a maximum and diffusion coefficients that decrease with concentration. A maximum diffusion coefficient was observed at pH far from the isoelectric point and at low ionic strength where the zeta potential is high. The estimated maximum diffusion coefficient increased with zeta potential. The estimated maximum diffusion coefficient decreased at pH near the protein isoelectric point and when ionic strength was high. The estimated maximum diffusion coefficient also shifted to lower protein concentration as zeta potential increased. Similar behavior was observed by Mignard and Glass [100], Saksena and Zydney [80], and Bowen et al. [25]. Results also show that diffusion coefficient becomes ionic strength independent at pH close to the isoelectric point of the protein. Very good agreement between the experimental data [101] and the model prediction was obtained at pH 7 and ionic strength of 0.15M. For BSA, D_B was obtained from literature and vary from $5\text{-}7\times10^{-11}$ $m^2.s^{-1}$ [73,102-104]. The value of 6.7×10^{-11} $m^2.s^{-1}$ was used in all the calculations of this study for the Brownian diffusion coefficient of BSA [73].

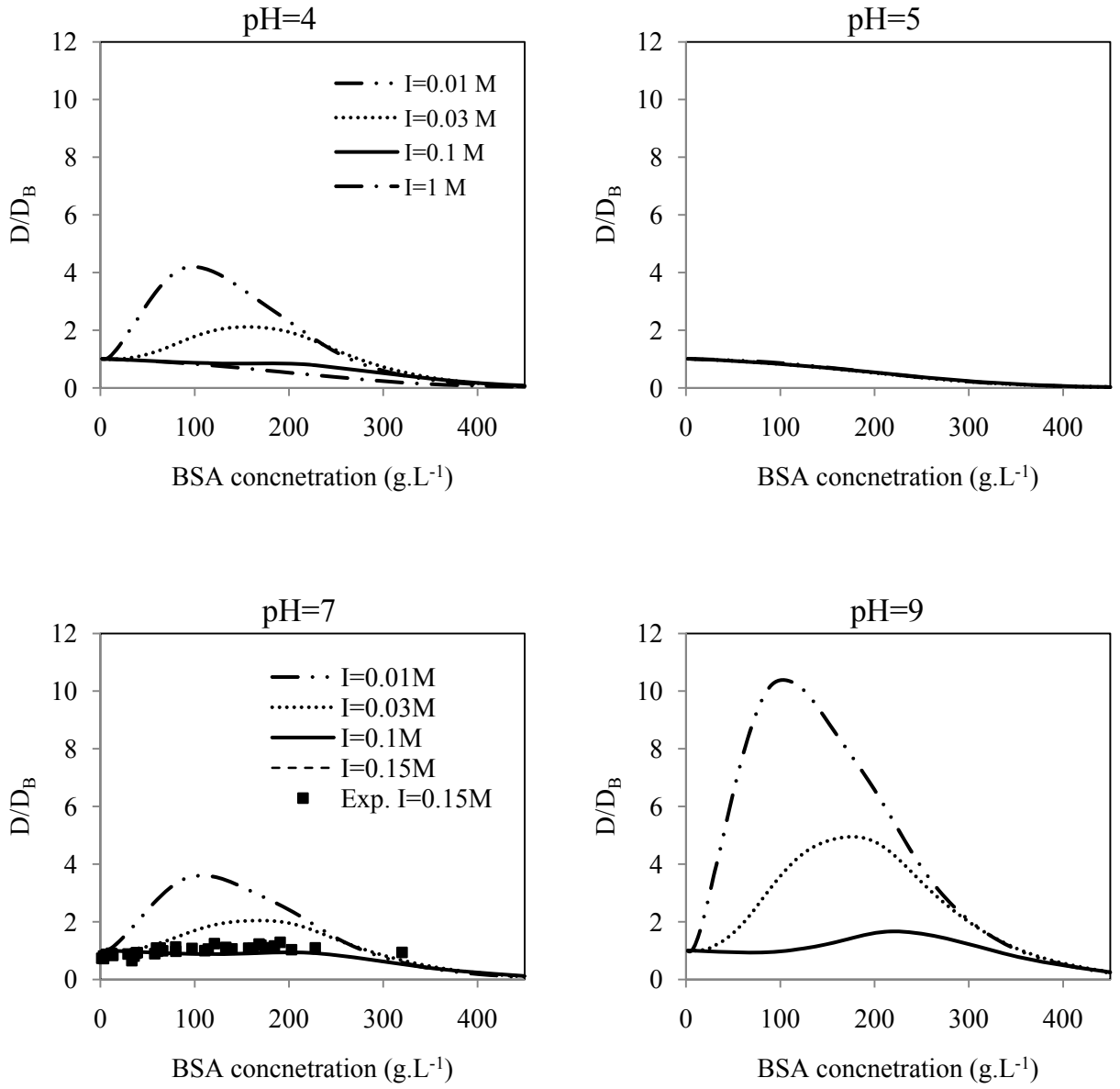

Figure 4.12 Dimensionless diffusion coefficient of BSA according to pH and ionic strength (I(M))

4.7.1.5 Artificial Neural Network

The dataset of osmotic pressure obtained in section 4.7.1.3. was analyzed using linear and nonlinear multivariable regression techniques using MATLAB statistics toolbox (The MathWorks™, 2008); however, the regression models were not accurate enough to cover the

whole dataset due to the inherent nonlinearity of the problem. In this study, ANN was used to obtain an accurate regression model.

It is very important to normalize the input data before starting the ANN to avoid any false influence of factors with higher order of magnitude. Data normalization was performed using equation 4.33.

$$X = \frac{x - {(x_{max} + x_{min})}/{2}}{{(x_{max} - x_{min})}/{2}} \qquad 4.33$$

where x_{max} and x_{min} are the highest and lowest values of actual variable x. The ANN model (Figure 4.6) consisted of training and testing steps. In the first step, the ANN was subjected to approximately 6000 training sets of input/output pattern. The training set was selected to cover the whole range of pH (4-9), ionic strength (0.01M-1M), and protein concentration (2 $g.L^{-1}$-300 $g.L^{-1}$). The weights were obtained according to back-propagation technique. In the second stage, the performance of the ANN was tested with approximately1000 new and independent datasets. The training and testing dataset were selected randomly from the whole available dataset.

Different number of neurons was tested in the model; however, the lower number of neurons was preferred since higher neurons tend to over train the dataset which result in an unstable model and consequently inaccurate results. Figure 4.13 shows the predicted (ANN) versus observed (Multi-scale modeling) values for the osmotic pressure of BSA for both training and testing sets. As can be observed, the ANN model can accurately cover the whole data set. Table 4.4 presents the weights of each neuron.

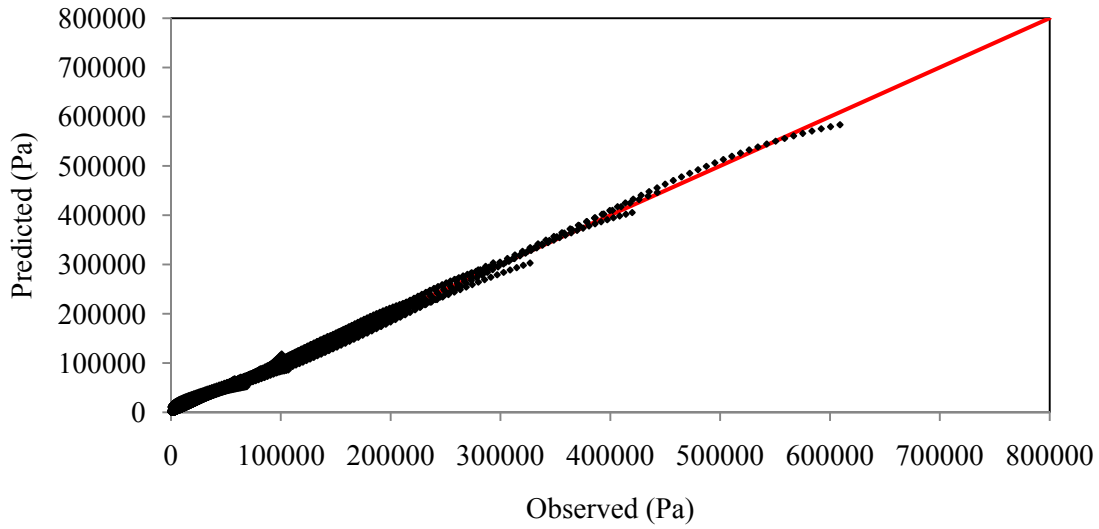

Figure 4.13 Predicted versus observed values for osmotic pressure of BSA

Table 4.4 Weights corresponding to each neuron for ANN modeling of BSA osmotic pressure

	IW			**b1**
BSA osmotic pressure	-1.58163	0.828248	-1.59484	2.393966
	1.952356	-0.60267	-1.24746	-1.19698
	1.606059	0.57537	-1.67946	0
	0.778145	-1.43153	-1.75394	1.196983
	1.335337	1.067513	1.675817	2.393966
LW				
0.389657246	-0.3658	0.900444	-0.93111	-0.12251
b2				
-0.236883086				

4.7.2 Soy glycinin

According to the physical properties of glycinin reported in Table 4.1 and Table 4.2, the dry hard-sphere protein radius was calculated as 4.52 nm using equation 4.16. Equation 4.17 gives the effective hard-sphere protein radius of 5.17 nm for glycinin inside a solution. The hydrodynamic radius of glycinin was taken 5.4 nm which is the effective hard sphere radius plus the distance to the OHP. Zeta potential of glycinin was calculated according to the charge

regulation model and based on the type and number of the amino acids of glycinin presented in Table 4.2..

4.7.2.1 Zeta potential

Figure 4.14 presents the zeta potential of glycinin calculated for a pH range of 4-9 and ionic strength range of 0.01-1M based on the charge regulation model. The isoelectric point of 6 was estimated for glycinin which also agrees with the experimental value of 6.4 reported by Achouri et al. [75]. Glycinin surface carries a positive net charge at pH lower than 6, glycinin isoelectric point, and a negative net charge at pH higher than 6.

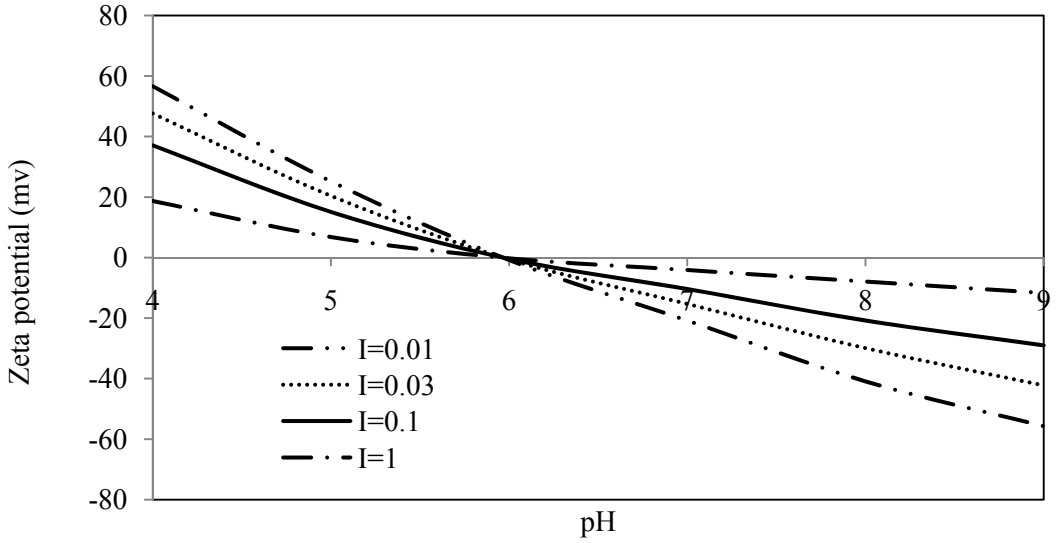

Figure 4.14 Estimated zeta potential for glycinin at various ionic strength (I((M)) using charge regulation model (protein concentration of 20 $g.L^{-1}$)

Table 4.5 represents the soy glycinin electrostatic potential and the charge density (according to the algorithm, Figure 4.5) along with the electrostatic force for a glycinin concentration of $200g.L^{-1}$. Regardless of pH and ionic strength, the absolute value of surface potential is larger than zeta potential according to the electrical double layer theory. When ionic strength is higher than approximately 0.5M, ion shielding effects become very important resulting in decrease in the electrostatic forces/pressure.

Table 4.5 Glycinin potential (ψ), electrostatic force and pressure at the hexagonal cell surface according to pH and ionic strength (I (M)) for a protein concentration of 200g.L^{-1}

	pH	4	5	6	7	8	9
Zeta potential (mV)	**I=0.01**	57.4	26.1	-0.8	-21.6	-41.3	-57.7
	I=0.03	47.7	20.5	-0.6	-15.4	-30	-42.4
	I=0.1	37.1	15.1	-0.42	-10.3	-20.2	-29
	I=0.5	23.7	8.9	-0.2	-5.5	-10.7	-15.7
	I=1	18.7	6.8	-0.2	-4.1	-7.9	-11.7
Surface potential (mV)	**I=0.01**	66.3197	29.6540	-0.9050	-24.5080	-47.2296	-66.6814
	I=0.03	59.2943	25.0554	-0.7306	-18.7918	-36.8233	-52.4715
	I=0.1	51.7110	20.6921	-0.5736	-14.0895	-27.7536	-40.0992
	I=0.5	42.4098	15.7317	-0.3528	-9.7098	-18.9303	-27.8696
	I=1	38.9457	14.0325	-0.4121	-8.4532	-16.3105	-24.2106
Surface charge density (C.m^{-2})	**I=0.01**	0.0287	0.0114	-0.0003	-0.0094	-0.0191	-0.0289
	I=0.03	0.0373	0.0147	-0.0004	-0.0109	-0.0219	-0.0324
	I=0.1	0.0470	0.0180	-0.0005	-0.0122	-0.0243	-0.0357
	I=0.5	0.0602	0.0220	-0.0005	-0.0135	-0.0265	-0.0391
	I=1	0.0651	0.0233	-0.0007	-0.0140	-0.0271	-0.0402
Total charge ()	**I=0.01**	59.7941	22.4532	-2.7727	-21.6852	-42.0594	-62.5179
	I=0.03	76.5851	28.8124	-2.8849	-24.8127	-47.9384	-69.8623
	I=0.1	97.1279	35.6241	-2.9855	-27.4567	-52.7939	-76.7373
	I=0.5	125.0082	44.3656	-3.1265	-29.9725	-57.3134	-83.9847
	I=1	135.8743	47.6162	-3.0887	-30.7023	-58.6317	-86.2159
Electrostatic force (N)	**I=0.01**	5.21E-12	1.25E-12	1.23E-15	8.68E-13	2.94E-12	5.25E-12
	I=0.03	1.00E-12	2.03E-13	1.78E-16	1.16E-13	4.25E-13	8.11E-13
	I=0.1	2.01E-14	3.54E-15	2.77E-18	1.66E-15	6.27E-15	1.26E-14
	I=0.5	1.69E-19	2.45E-20	1.24E-23	9.39E-21	3.53E-20	7.55E-20
	I=1	1.97E-23	2.82E-24	0.00E+00	1.13E-24	3.38E-24	7.89E-24
Electrostatic pressure (Pa)	**I=0.01**	4.29E+04	1.03E+04	1.01E+01	7.15E+03	2.43E+04	4.33E+04
	I=0.03	8.26E+03	1.68E+03	1.47E+00	9.56E+02	3.50E+03	6.69E+03
	I=0.1	1.66E+02	2.92E+01	2.29E-02	1.37E+01	5.17E+01	1.04E+02
	I=0.5	1.39E-03	2.02E-04	1.02E-07	7.74E-05	2.91E-04	6.23E-04
	I=1	1.63E-07	2.32E-08	0.00E+00	9.29E-09	2.79E-08	6.51E-08

4.7.2.2 London-van der Waals forces

Since the refractive index data for soy glycinin is not available in literature, a constant value of 10KT was assumed in this work to calculate the London-van der Waals forces. According to literature Hamaker constant for most of the proteins varies between 1-10KT [105,106]. The

value of 10KT was also assumed for soy protein by Berli et al. [107]. It was found that decreasing the Hamaker constant by 50% could increase the osmotic pressure by an average value of 17% at a high glycinin concentration of 200 $g.L^{-1}$. The effect of ionic strength on the attraction force (equations 4.21 and 4.21) was neglected by assuming a constant value for the Hamaker constant. This assumption is valid when the ionic strength is high (see the results for BSA in Figure 4.8). Figure 4.15 shows the dimensionless London-van der Waals attraction energy ($V_{attraction}/KT$) versus the glycinin concentration

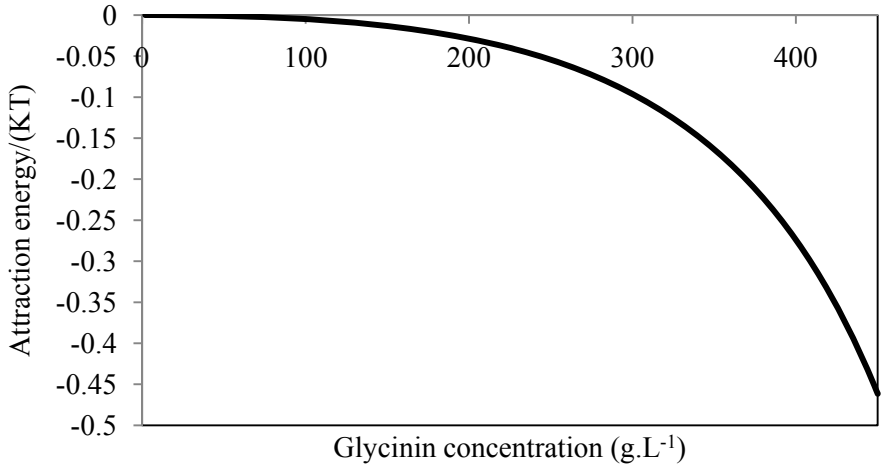

Figure 4.15 Effect of glycinin concentration on the London-van der Waals energy

4.7.2.3 Osmotic pressure

Osmotic pressure of soy glycinin is shown in Figure 4.16. Similar behavior to that of BSA was observed for soy glycinin. Estimated Osmotic pressure of glycinin was significantly lower than for BSA mostly because the molecular size of glycinin is twice the size of BSA. Results in Figure 4.16 show that the estimated osmotic pressure of glycinin at pH 7 passes through a maximum with increasing protein concentration. Petsev et al. [108] and Jönsson et al. [109] explained that the maximum osmotic pressure corresponds to a transition from a dispersed to a solid state. The maximum is observed when the attraction (London-van der Waals) force in equation 4.4 becomes the dominant term. For BSA, the maximum estimated osmotic pressure

was observed at around 550g.L^{-1}. At pH close to the isoelectric point of the protein or at high ionic strength, the attraction force becomes a dominant term in equation 4.4 which causes the maximum to occur at low glycinin concentration (around 250 g.L^{-1}). At ionic strength of 1M, osmotic pressure became pH independent as a result of charge shielding effect.

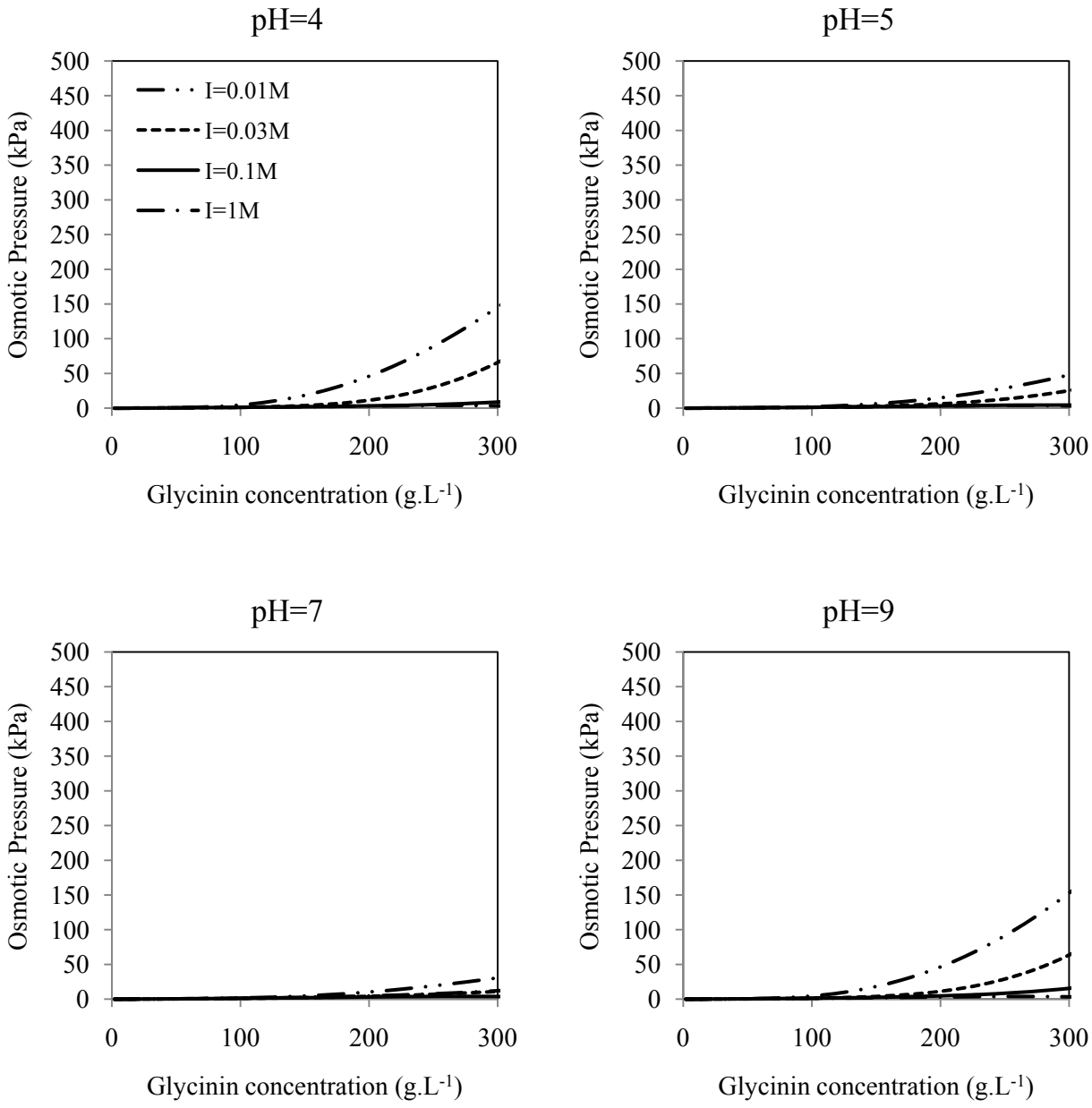

Figure 4.16 Estimated osmotic pressure of soy glycinin according to pH and ionic strength (I(M))

4.7.2.4 Diffusion coefficient

Figure 4.17 shows the diffusion coefficient of glycinin at various pH and ionic strength calculated from the procedure stated in section 4.4. Similar to BSA, two different trends were observed; diffusion coefficients that pass through a maximum and diffusion coefficients that decrease with concentration. The concentration at which the estimated diffusion coefficient becomes zero, corresponds to the highest protein concentration that protein could be soluble in the solution [14]. The value of 3.44×10^{-11} $m^2.s^{-1}$ was used in all the calculations of this study for the Brownian diffusion coefficient of glycinin [72].

4.7.2.5 Artificial Neural Networks (ANN)

Results obtained for osmotic pressure of glycinin were modeled using ANN technique. The network used in this work consisted of 5 neurons and 1 hidden layer (Figure 4.6). The ANN was trained to approximately 3500 sets of input/output pattern and was tested with approximately 850 new and independent datasets. The training set was selected to cover the whole range of pH (4-9), ionic strength (0.01M-1M), and protein concentration (2 $g.L^{-1}$-300 $g.L^{-1}$). Figure 4.18 shows the predicted values (ANN) versus the observed values (Multi-scale modeling). Results show that the ANN model was able to correlate the osmotic pressure data set. Table 4.5 summarizes the weights of each neuron.

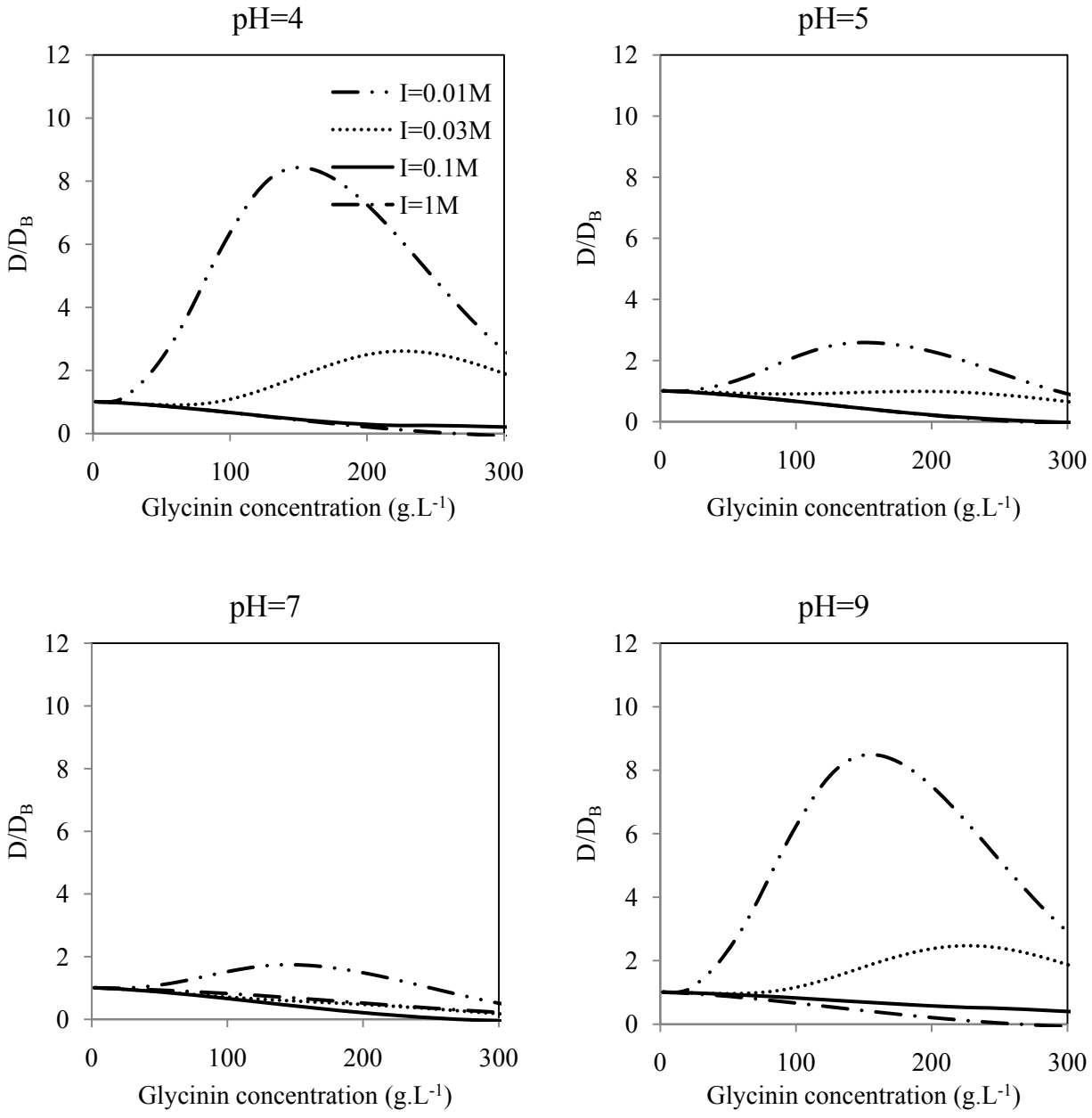

Figure 4.17 Dimensionless diffusion coefficient of glycinin according to pH and ionic strength (I(M))

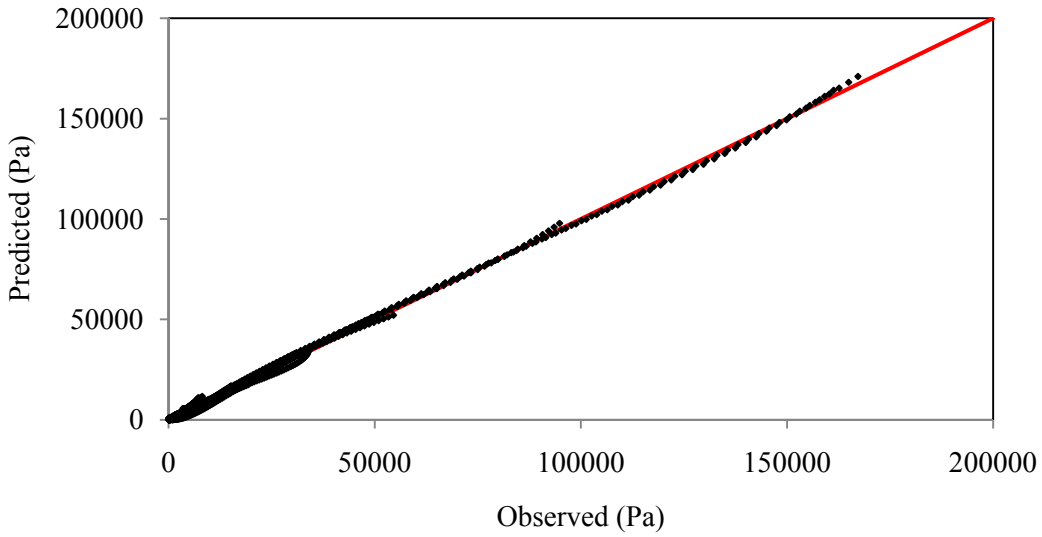

Figure 4.18 Predicted versus observed values for osmotic pressure of soy glycinin

Table 4.6 Weights corresponding to each neuron for ANN modeling of glycinin osmotic pressure

	IW			b1
Glycinin osmotic pressure	1.225056	-1.56657	-1.33273	-2.39397
	1.472594	-0.80382	1.707753	-1.19698
	-1.50868	0.189616	1.849052	0
	1.604499	1.775791	-0.05676	1.196983
	0.556837	1.955792	1.263284	2.393966
LW				
-0.71623	-0.15648	0.831471	0.584415	0.918985
b2				
0.311481				

4.7.3 Comparison between BSA and soy glycinin

The multi-scale modeling results obtained in this work provided new detailed information about the osmotic pressure and diffusion coefficient behaviors for BSA and soy glycinin; the major differences are summarized as follow:

1. The estimated isoelectic point of glycinin was found to be higher than that of BSA due mostly to the difference in the amino acids of the proteins. It was found that the isoelectric

point of BSA changes with the ionic strength of the solution. Isoelectric point of glycinin, however, was independent of ionic strength because the salt adsorption on the glycinin surface was neglected in the charge regulation model.

2. The absolute value of London-van der Waals attraction force between the glycinin proteins was found around 10 times more than that of BSA. The London-van der Waals force between the glycinin molecules was calculated based on a constant value for the Hamaker constant. The Hamaker constant for BSA, however, was evaluated from the experimental refractive index of the protein in solution and Lorenz-Lorentz equation which gave the power to consider the effect of BSA concentration and ionic strength.
3. Osmotic pressure of glycinin was found much lower than that of BSA. Depending on how much pH was far from the isoelectric point of the protein, osmotic pressure of BSA could be up to 3 times more than the glycinin's. These new results reveals that osmotic pressure is of less importance during the soy protein ultrafiltration process which could be neglected in the permeate flux calculation specially at low TMP and feed concentration.
4. Protein concentration corresponding to the maximum osmotic pressure was found lower for glycinin compared to BSA explaining that the transition of dispersion to solid state occurs at lower concentration for soy glycinin. This piece of information is of importance in selecting the right operating conditions for the ultrafiltration process. In order to decrease the membrane fouling during the ultrafiltration process, operating conditions such as TMP, feed concentration, and axial velocity should be selected to insure that the transition concentration of the protein on the membrane surface is not reached.
5. Similar behavior was found for diffusion coefficient of BSA and soy glycinin. Diffusion coefficient depends on how far the pH is from the isoelectric point of the protein and the ionic strength of the solution.

4.8 Conclusion

Osmotic pressure and diffusion coefficient of BSA and soy glycinin were estimated considering the particle-particle interactions; Electrostatics, London-van der Waals, and hydration forces as well as entropy pressure. No adjustable parameter was used in the multi-scale model. Very good agreement between experimental data and theoretical predictions for zeta potential, osmotic

pressure and diffusion coefficient of BSA was observed. It was shown that the electrostatic force has the most significant effect on the osmotic pressure when pH diverges from the isoelectric point of the protein. The hydration force was found to have a negligible effect on the osmotic pressure compared to other forces. Results showed that osmotic pressure increases as pH diverges from the protein isoelectric point. Increasing the ionic strength, however, tends to reverse the effect by shielding charges, causing molecular contraction and thereby decreasing the osmotic pressure. The maximum osmotic pressure corresponding to the concentration in which the transition from a dispersed to a solid state occurs was observed at concentrations lower than 300 $g.L^{-1}$ for soy glycinin. At this concentration, diffusion coefficient became zero. Two different trends were observed for diffusion coefficient at specified pH and ionic strength values; diffusion coefficient values that decrease with protein concentration and diffusion coefficient values that pass through a maximum. When zeta potential of the protein is low, either at high ionic strength or at pH close to the protein isoelectric point, diffusion coefficient decreases with protein concentration and no maximum is observed. At last, the Artificial Neural Network (ANN) modeling was performed to relate the osmotic pressure of protein to the concentration, pH, and Ionic strength. Despite the inherent nonlinearity of the problem, ANN was found to be highly precise in predicting the osmotic pressure in a wide range of pH, ionic strength, and protein concentration. The results obtained in this chapter can be used to develop a comprehensive model with the ability to relate the macroscopic behavior of the permeate flux to the molecular interactions through the transport properties such as diffusion coefficient and the thermodynamic properties such as osmotic pressure. Such a model, can easily address the complexity of the fouling phenomena during the ultrafiltration process by providing detailed information about the effect of environment on the thermodynamical and physical properties of the protein.

Chapter 5

Computational Fluid Dynamics Simulation of BSA Ultrafiltration in a Hollow Fiber Membrane Module-Colloidal Interaction Approach

Overview

This work presents computational fluid dynamics modeling of bovine serum albumin ultrafiltration in a hollow fiber membrane for a total recycle operation. To establish a more comprehensive model and thereby alleviate the shortcomings of the previous filtration models, this model considers all the possible phenomena causing the permeate flux decline during the BSA ultrafiltration: osmotic pressure, concentration polarization resistance, and protein adsorption resistance on the membrane surface.

Membrane permeate flux is generally modeled through Darcy equation applying an osmotic pressure model (equation 2.4) or a resistance-in-series model (equation 2.5). Protein-protein interaction is normally considered in the permeate flux modeling through the osmotic pressure term. Resistance-in-series model is typically used to macroscopically model the permeate flux through the various fouling layers forming on and inside the membrane. A combination model of resistance-in-series and osmotic pressure was used to consider the protein interactions and also the various fouling layers forming during the ultrafiltration. A novel mathematical approach was introduced to predict the concentration polarization resistance. This resistance was estimated based on the concentration and thickness profiles of the concentration polarization layer on the membrane obtained from the solution of the equations of motion and continuity at previous time step. This model had the ability to show how microscopic phenomena can affect the macroscopic behaviors by providing detailed information about the local characteristics on the membrane. Governing equations were solved using COMSOL Multiphysics. Very good agreement between the experimental permeate flux and the model predictions was observed. Results reveal that concentration polarization and osmotic pressure were negligible at low TMP for pH between 5 and 9 and ionic strength of 0.01M and 0.1M due to the low BSA accumulation on the membrane. The effects of concentration polarization and osmotic pressure on the permeate flux were more profound at high TMP and high BSA feed concentration. At pH 5, the permeate flux was limited by BSA adsorption on the membrane surface. Concentration polarization and osmotic pressure had negligible effect on the permeate flux decline even at high TMP. At pH 9, very low resistance due to the protein adsorption was observed. For the solution at pH 7, protein adsorption was the dominant factor for the permeate flux decline at low TMP but concentration

polarization and osmotic pressure became important at high TMP. The effect of constant viscosity and diffusion coefficient on the permeate flux showed that assuming a constant diffusion coefficient in the calculation can affect the permeate flux differently depending on pH and ionic strength. In addition, permeate flux was underestimated when a constant viscosity was used in the calculation.

5.1 Introduction

Cross-flow ultrafiltration (UF) is a viable low cost alternative technology for the concentration or separation of protein solutions. However, membrane fouling and solute build up in the vicinity of the membrane surface decrease the performance of the process by lowering the permeate flux. Extensive work has been accomplished to better understand and minimize fouling occurrence. The importance of the hydrodynamics and mass transfer conditions has been established, but simple mass transfer models such as the film theory model have limited capability mostly because concentration effects are not considered. In contrast, more complicated mass transfer models can be applied in a computational fluid dynamics (CFD) model in order to capture the contribution of concentration and improve the representation of fouling during membrane ultrafiltration operations.

The complexity of proteins and their sensitivity to the ionic conditions during filtration have also been recognized. The role of proteins in fouling for retentive membranes is generally classified as concentration polarization, gel layer, and membrane adsorption. Concentration polarization is the result of solutes brought to the membrane by convective flux and their back transport to the bulk by diffusion which produces an additional resistance to that of the membrane. A gel layer starts to form on the membrane once the solute concentration on the membrane reaches a limiting value i.e. the gel concentration of the solute. Solute adsorption on the membrane surface or within the membrane pores is a result of solute-membrane interactions. According to Marshall et al. [13], protein adsorption occurs predominantly on the membrane surface during ultrafiltration.

Extensive studies have been performed to model membrane fouling during ultrafiltration processes. Yee et al. [110] developed an empirical relation to predict the permeate flux decrease during the operation of long-term UF of whey through a spiral wound membrane module in a total recycle mode. The filtration was divided into three stages of concentration polarization and protein adsorption in the first few minutes, protein deposition for several hours, and long term fouling i.e. the consolidated deposits. The proposed model contained two parameters for each stage (six parameters in total i.e. the limitation of the work) obtained by regression analysis of the permeate flux. Juang et al. [111] simulated an UF of fermentation broth of Bacillus subtilis culture in a flat sheet membrane. Concentration polarization, cake deposition, and solute adsorption were introduced in the resistance in series model. The fitting parameters in the time dependent expression for the cake deposition on the membrane were obtained by comparing the simulated permeate flux to the experimental permeate flux data. However, fitting parameters were obtained at different TMP showing the weakness of the model. Sarkar et al. [32] investigated the flux decline during electric field-assisted UF of mosambi juice in a flat sheet membrane. Applying the resistance in series model, they considered the gel resistance and the intrinsic membrane resistance. They assumed that the solute concentration in the gel layer is constant and gel thickness increases with time. They added the electric force to the normal convection-diffusion transport equation of solute to consider the effect of the electric field on the gel thickness. They neglected the osmotic pressure and solute adsorption on the membrane but a good agreement between the experimental and the model data was observed. It seems that the gel layer was the dominant resistance to the permeate flux, and ignoring the other fouling terms did not affect the model prediction. In protein filtration, however, ignoring the osmotic pressure and membrane adsorption might result in error in the model prediction [43,112]. Steady state modeling of UF of Dextran T500 in a tubular membrane was performed by Chikhi et al. [33]. Resistance in series model was used to consider the pore blockage and the concentration polarization. Empirical relations for both resistances as a function of concentration and axial velocity were applied in the model. Finite volume method was used to solve the equations of motion and continuity. They observed that their model overestimates the permeate flux at higher cross-flow velocities. Cross-flow UF of BSA protein solution in a rectangular channel with one porous wall was modeled by Bowen and Williams [112]. Osmotic pressure model was used to simulate the permeate flux. They solved 2-dimensional steady state equations of motion and

continuity using the finite difference method. The osmotic pressure and diffusion coefficient were calculated based on colloidal interactions [21,22]. Theoretical prediction was compared with the experimental permeate flux for BSA and lactoferrin UF. They explained that the under/overestimations in the permeate flux could be due to some uncertainty in the theoretical viscosity calculation and suggested that a more sophisticated description of rheological properties would be needed for better prediction. The shortcoming, however, could be more due to the fact that concentration polarization is not the only reason for the flux decline. BSA ultrafiltration through a flat sheet membrane was simulated by Schausberger et al. [43] using CFD. A combination of resistance in series and osmotic pressure model was applied to define the permeate velocity. By ignoring the concentration polarization resistance, they considered a summation of irreversible fouling resistance and intrinsic membrane resistance. The irreversible fouling resistance was assumed to be a linear function of the amount of protein adsorbed on the membrane surface. The rate of change of protein adsorption on the membrane was then defined to be first order with respect to surface saturation (the difference of equilibrium adsorption and adsorption at time t) and of order k with respect to protein concentration. An ideally packed protein monolayer was assumed to estimate the equilibrium adsorption. Results showed an over-prediction of irreversible fouling and underestimation of concentration polarization showing the fact that the model needed to be treated.

In this study, a model was developed for BSA ultrafiltration with fully retentive membranes and total recycle operation in order to maintain a constant feed concentration. BSA was chosen as a model protein in this work because its physiochemical properties have been extensively investigated and it is a common protein in biotechnology applications. The motivation of the current work was to alleviate the shortcomings of the model predictions obtained by [43] and [112]. Neglecting the concentration polarization resistance in [43] and the combination of concentration polarization and protein adsorption on the membrane in [112] resulted in errors of the model predictions. The current work considers all the possible phenomena causing the permeate flux decline during the BSA ultrafiltration; osmotic pressure, concentration polarization, and membrane adsorption contrary to the previous filtration models that neglect one or more fouling terms. In this work the effect of pH and ionic strength on the membrane fouling, concentration polarization and adsorption behavior was investigated. Concentration polarization

resistance represents protein-protein interactions while protein adsorption resistance represents mainly protein-membrane interactions. This model also considers osmotic pressure. Osmotic pressure and diffusion coefficient of BSA were calculated as a function of protein concentration at a given pH and ionic strength based on the protein-protein interaction explained in details in chapter 4.

Concentration polarization resistance was calculated based on the thickness and concentration profile in the concentration polarization layer on the membrane obtained from the solution of the governing equations at previous time step. Gel layer formation occurs if and only if the local concentration in the concentration polarization layer exceeded the gel concentration (calculated from the osmotic pressure profile as described previously in chapter 4). Since the diffusion coefficient of BSA and the viscosity of the solution as well as the osmotic pressure are all concentration dependants and concentration changes locally on the membrane, simplified models are not sufficient to describe the complexity of the fouling phenomena.

5.2 Modeling

5.2.1 Geometry and governing equations

The system consisted of a hollow fiber cartridge of 45 fibers with 5.0×10^{-4} m radius and 0.3 m length. Each fiber was assumed to be identical and only one fiber was modeled. Computational domain and the mesh resolution were similar to those described in Rajabzadeh et al. [113]. Transient equations for conservation of mass, protein concentration, and momentum in 2D-cylindrical coordinates are mathematically given in equations 3.1 to 3.3. The laminar equation of motion was used because the Reynolds number was smaller than 1500. Similar boundary conditions to those introduced in chapter 3 (equations 3.4a-3.4f) were applied in this work except the feed concentration at the fiber inlet. Since the filtration was performed in a total recycle mode, the feed concentration at the fiber inlet was assumed constant.

5.2.2 Permeate flux modeling

Wall velocity (*Vw*) was defined by Darcy equation (equation 5.1), and was used as the boundary condition for the equation of motion.

$$v_w = \frac{\Delta P - \pi}{\mu (R_m + R_{cp} + R_{ad})} \tag{5.1}$$

ΔP, is the local pressure difference between the inside pressure P and the outside pressure of the membrane at a given position z along the fiber; ΔP varies along the membrane. The pressure on the outside of the membrane was assumed to be atmospheric pressure. π is the local osmotic pressure and is a function of protein concentration, pH and ionic strength as described previously in chapter 4. R_m, R_{cp}, and R_{ad} represent the clean membrane, concentration polarization and protein adsorption resistances, respectively. Figure 5.1 represents the concentration polarization and protein adsorption layers forming on the membrane surface.

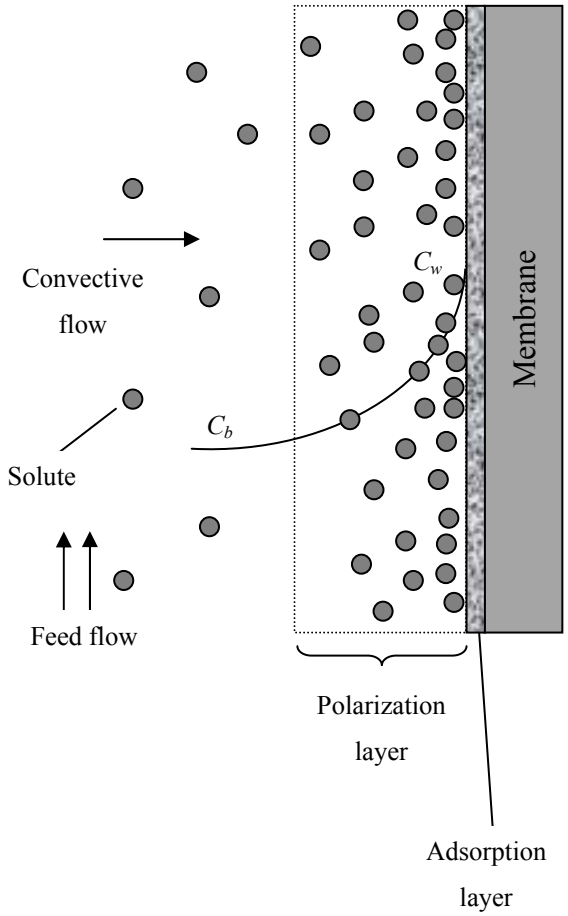

Figure 5.1 Schematic representation of concentration polarization and membrane adsorption (adapted from [15])

In the model developed in this study, the fouling layer was represented as two components, concentration polarization and protein adsorption. The concentration polarization layer represents the primary reason for the permeate flux decline at the beginning of any filtration operation [13]. The thickness and the concentration profile of the concentration polarization layer are controlled by the magnitude of the convection and the back transport diffusion terms. When the protein concentration in the concentration polarization layer reaches a critical concentration, $C_{\pi\,max}$, a gel layer forms as described in detail in chapter 4 and by Bacchin et al. for suspensions [14]. Bacchin et al. showed that osmotic pressure theoretically passes through a maximum that corresponds to $C_{\pi\,max}$ at which phase transition occurs. The concentration polarization resistance was estimated by integrating the specific resistance of the protein build-up in the concentration polarization layer (equation 5.2). The local thickness of the concentration

polarization layer, δ, was defined as the distance from the membrane surface where $\frac{C-C_b}{C_b} < 0.1$ [114]. The specific resistance was calculated using Happel equation which relates the specific resistance to the local protein concentration (equations 5.3 and 5.4) [115]. Using Happel equation to estimate the resistance of the concentration polarization layer of proteins instead of a bed of rigid spheres might result in prediction errors. This equation, however, was applied previously [22,23] to estimate the specific resistance of BSA cake on the membrane surface during a dead-end ultrafiltration process. The authors confirmed the suitability of the equation for a BSA filter cake. Since the concentration profile and δ vary along the membrane surface, a profile for concentration polarization resistance along the membrane was expected.

$$R_{cp}(z) = \int_0^{\delta(z)} \alpha(z,r)dr \tag{5.2}$$

$$\alpha = \left(\frac{9(1-\varepsilon)}{2a^2} \times \frac{3 + 2(1-\varepsilon)^{\frac{5}{3}}}{3 - 4.5(1-\varepsilon)^{\frac{1}{3}} + 4.5(1-\varepsilon)^{\frac{5}{3}} - 3(1-\varepsilon)^2} \right) \tag{5.3}$$

α(z,r) is the specific resistance (m^{-2}), and *ε(z,r)* is the local porosity. Vilker et al. [74] suggested an equation relating the porosity to the protein concentration (equation 5.4).

$$1 - \varepsilon = \phi = Cv\left(\frac{a+d}{a_{dry}}\right)^3 \tag{5.4}$$

C(z,r) is the local protein concentration (g/L) in the concentration polarization layer; a_{dry} is the dry hard sphere particle radius; *a* is the effective particle radius, *d is* distance to OHP (see chapter 4 for detail); *v* is the specific volume of BSA. These values were quantified and presented in depth by Bowen et al. [21].

The second resistance term considered was the BSA adsorption on the membrane surface. According to Le and Howell [16] protein adsorption takes place as a monolayer followed by further protein deposition due to hydrophobic interaction and intermolecular disulphide bond

formation during ovalbumin and cheese whey ultrafiltration in a tubular membrane. The monolayer adsorption on the membrane is usually represented by Langmuir or Freundlich equations [13,15,61]. The equations describe the amount of solutes statically adsorbed on the membrane surface or inside the membrane pores as a function of bulk concentration. However, using these equations to estimate the protein adsorption on the membrane during filtration would result in some errors. During a membrane filtration process, protein concentration on the membrane becomes higher than the bulk concentration due to the polarization layer. Therefore, membrane surface exposes the polarization layer with higher concentration than the bulk concentration. Therefore, it is of vital importance to relate the membrane adsorption to the solute concentration in the polarized layer and not the bulk concentration. Nikolova and Islam [116] found that adsorbed layer resistance varied linearly with dextran concentration at the ultrafiltration membrane surface. A similar equation to that of Nikolova and Islam was used in this work to estimate the protein adsorption resistance (equation 5.5). Equation 5.5 explains that protein adsorption resistance increases with the development of the concentration polarization layer. The parameter k_{ad} was obtained by minimizing the error between the prediction and the experimental permeate flux, and was assumed to be TMP independent.

$$R_{ad} = k_{ad} C_w \tag{5.5}$$

5.2.3 Diffusion coefficient and viscosity

Diffusion coefficient was considered as a function of BSA concentration for the given pH and ionic strength as discussed in chapter 4. Kozinski and Lightfoot [117] proposed a concentration dependant viscosity for BSA (equation 5.6), which has negligible dependency on pH and buffer type. A constant density of water was considered in the calculation. μ^0 and C are the water viscosity and protein concentration, respectively.

$$\mu = \mu^0 e^{0.00244(0.1C)^2} \tag{5.6}$$

5.2.4 Numerical algorithm

Figure 5.2 shows the numerical algorithm used to solve the governing equations. For a given pH and ionic strength, the osmotic pressure and its components were calculated as a function of BSA concentration as described in chapter 4. The estimated osmotic pressure, viscosity and diffusion coefficient as a function of BSA concentration were the input to the CFD model for the given pH and ionic strength. At the beginning of the filtration, protein adsorption resistance and concentration polarization resistance on the membrane were assumed zero. Permeate velocity was estimated from equation 5.1 and was used as the boundary condition for the equation of motion. The osmotic pressure was calculated with the bulk concentration since no concentration polarization had formed on the membrane at time zero. The thickness and concentration profile of the concentration polarization layer on the membrane were calculated from the solution of the governing equations. The resistance of the concentration polarization layer was estimated with equations 5.2-5.4 and was used for the next time step. Osmotic pressure was updated for the revised BSA concentration profile. For the next time step, concentration polarization resistance, adsorption resistance (equation 5.5), and osmotic pressure are considered in equation 5.1, and the governing equations were solved. The adjustable parameter, k_{ad}, in equation 5.5 was arbitrarily chosen for the given pH and ionic strength. The same algorithm was used for the subsequent time steps. At each TMP, calculation terminated when permeate flux didn't change with time. The calculated pemeate flux at various TMP were compared with the experimental data obtained in this work and k_{ad} was adjusted if $R^2<0.98$. The major difference between the current algorithm and other algorithms in the literature [62,100,118,119] is that the algorithm in this work calculated the local thickness of the concentration polarization layer and the associated protein concentration profile at each time step to calculate the fouling resistances and updated the permeate flux for the next time step. MATLAB software (The MathWorks™, 2008) was linked to the commercially available finite element package, COMSOL Multiphysics (COMSOL Multiphysics®, version 3.5) for this purpose. A Pentium 2.13 GHz with 2 GB of Ram was used for the numerical tests. The validity of COMSOL Multiphysics for filtration modeling has been confirmed [41,113].

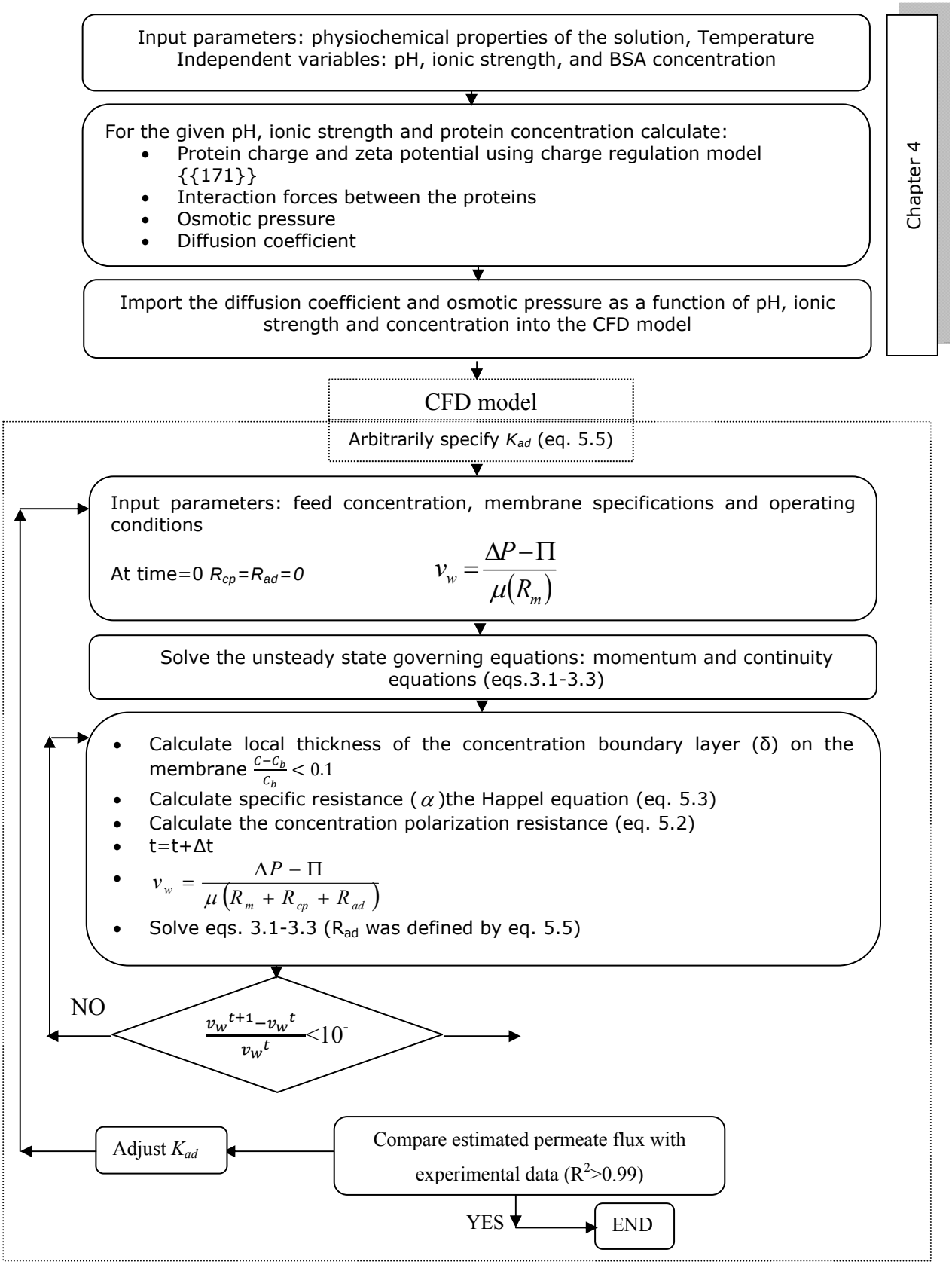

Figure 5.2 Flow diagram of the algorithm to estimate the permeate flux

5.3 Experimental

5.3.1 Reagents and solutions

Lyophilized BSA with 96% purity was purchased from Sigma-Aldrich (Oakville, ON, Canada, A3912). BSA solutions were prepared by adding a weighed amount of BSA to an aqueous solution of known ionic strength (I=0.01M-1M). Aqueous solutions were prepared by dissolving sodium chloride purchased from BDH (Mississauga, ON, Canada, BDH0286, 99%) in miliQ water (18.2 mΩ·cm at 25ºC, Synergy® Ultrapure water system, Milipore, Etobicoke, ON, Canada). The pH was then adjusted (±0.001, S80 SevenMulti™ pH meter, Mettler Toledo, OH, USA) to the desired value (pH=5-9) by drop-wise addition of HCl (0.1N) and NaOH (0.1N). BSA concentration in the feed solution was set to 5 $g.L^{-1}$ in all of the experiments.

5.3.2 Ultrafiltration experiments

Ultrafiltration of BSA solution was performed for a TMP range of 20-112 kPa using a 10 kDa asymmetric polysulfone hollow fiber membrane (membrane intrinsic resistance=6×10^{12} m^{-1}) purchased from GE Healthcare (UFP-10-EMA, Baie d'Urfe, QC, Canada). The module was 30 cm long with a 1 mm fiber inner diameter. The surface area available for filtration was 420 cm^2. The details of the experimental set-up are given in Rajabzadeh et al. [113]. Filtration was carried out in a total recycle mode (retentate and permeate were recycled to the feed tank) with a step-wise increase in TMP for 10 minutes at each step. Trans-membrane pressure, TMP, is the average value of ΔP at the entrance and at the exit of the fiber. Membrane resistance was measured before each experiment by performing water flux measurement (2-17 psi) at 25±1ºC (by maintaining the feed tank in a water bath). At each TMP, permeate velocity was calculated by measuring the mass of permeate flux collected with time (1-2 seconds) in a beaker suited on a balance (±0.01 g, Ohaus Corp., Pine Brooks, NJ, USA). The average cross-flow velocity inside each fiber was adjusted to 1 $m.s^{-1}$. At the end of filtration at TMP 112 kPa, the membrane was rinsed with 1L Nanopure water in both non-recycle (permeate and retentate are not recycled to the feed tank) and total recycle mode at the same operating conditions as the filtration. Water flux was then performed to estimate R_{ad} as was explained in Rajabzadeh et al. [113].

5.4 Results and discussion

5.4.1 Permeate flux

Permeate flux during BSA hollow fiber ultrafiltration in a total recycle operation mode was modeled. Microscopic phenomena, BSA-BSA interactions and ionic and pH effects were described through the osmotic pressure and diffusion coefficient calculation and incorporated into the macroscopic momentum and continuity equations. Figure 5.3 shows the effect of TMP based on experimental permeate flux data and simulated average permeate flux ($\frac{1}{L}\int_0^L v_W dz$) at different pH and ionic strength conditions for BSA ultrafiltration. The experimental data and the model predications were in good agreement indicating that the permeate flux increased with TMP and the rate of change of permeate flux decreased with TMP. The increase in permeate flux with TMP was more pronounced at pH 9 than at pH 7 and 5, closer to the isoelectric point of BSA, pH4.8 and conditions of zero net surface charge. At pH 9 and I=0.01M, permeate flux increased by 18 times when TMP was increased from 20kPa to 165kPa. At pH 5 and I=0.01M, permeate flux increased by only 4.8 times. At pH 7, increasing the salt concentration from 0.01M to 0.1M resulted in 20% increase in the permeate flux. In contrast, at pH 5, no significant difference in permeate flux was observed at different ionic strength. The interplay of pH, ionic strength, BSA surface charge, BSA interactions and osmotic pressure on the permeate flux and the associated fouling will be discussed in the subsequent sections. As pH increased, electrostatic repulsion between the membrane surface and BSA molecules increased resulting in less protein adsorption and consequently higher permeate flux. According to experimental evidence and also equation 5.1, permeate flux decline was not only caused by protein adsorption, but also by osmotic pressure and concentration polarization. Both osmotic pressure and concentration polarization depend on BSA concentration profile at the membrane surface, the magnitude of which is governed by diffusion coefficient (shown in chapter 4, Figure 4.12). Figure 4.12 showed that diffusion coefficient increased (or remains unchanged at high ionic strength, I=0.1M) when pH was increased resulting in less BSA concentration at the membrane surface due to the BSA back migration to the bulk and consequently a lower osmotic pressure. Therefore, it was expected to observe higher permeate flux at higher pH.

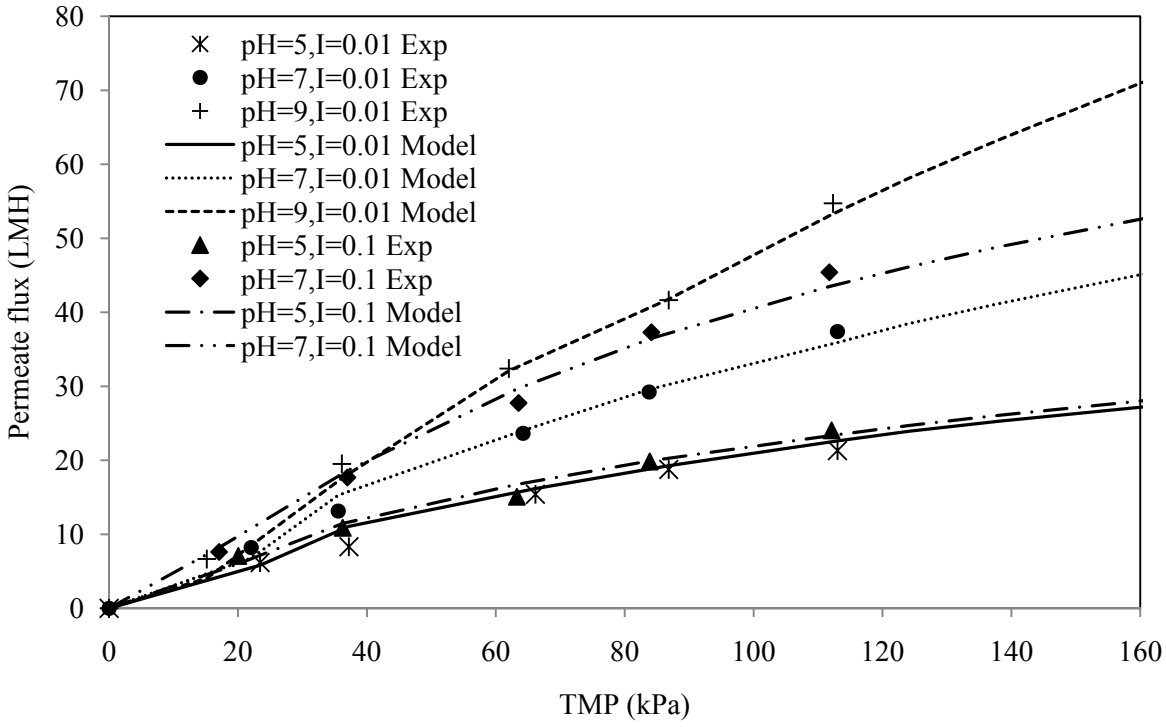

Figure 5.3 Effect of TMP on the average permeate flux

5.4.2 Concentration polarization resistance

The investigation of permeate flux and fouling at low TMP and total recycle operation gave information on the onset of fouling. In the proposed model of the fouling occurring during ultrafiltration, three components were considered that restricted permeate flux through the membrane, concentration polarization (R_{cp}), protein adsorption ($R_{ad,}$) and intrinsic membrane resistance. Concentration polarization results from protein-protein interactions and operating conditions while protein adsorption is predominantly governed by the physicochemical interactions between the membrane and protein. These two phenomena were modeled independently and will be discussed separately. Average concentration polarization resistance ($\frac{1}{L}\int_0^L R_{cp}dz$), calculated with equations 5.2-5.4, is presented in Figure 5.4 for different pH and ionic strength conditions. As expected, concentration polarization resistance increased with TMP for all pH and ionic strengths considered. The magnitude of R_{cp} remained relatively small, 0.1-0.9 $\times 10^{12}$ m^{-1} when compared to the intrinsic membrane resistance (6 $\times 10^{12}$ m^{-1}). At any given

TMP and low ionic strength (I=0.01M), estimated concentration polarization resistance was lowest at pH 5 and increased with increasing pH as did permeate flux which increased with increasing pH (Figure 5.3). The increase of R_{cp} and permeate flux with TMP at the same time is unexpected according to Darcy's relationship which shows an opposite relationship (equation 5.1). This can be explained by the small magnitude of R_{cp} and its negligible contribution to membrane fouling. The contribution of R_{cp} to the global resistance (R_g) is presented in Table 5.1 and Table 5.2. In Table 5.1, it was assumed that k_{ad}, adjustable parameter for adsorption resistance, depends only on pH and ionic strength (feed concentration independent). Therefore the same value of k_{ad} obtained by minimizing the error between the experimental and the model estimation for permeate flux at feed concentration of 5 $g.L^{-1}$ was used to model the permeate flux at feed concentration of 15 $g.L^{-1}$ and 30 $g.L^{-1}$.

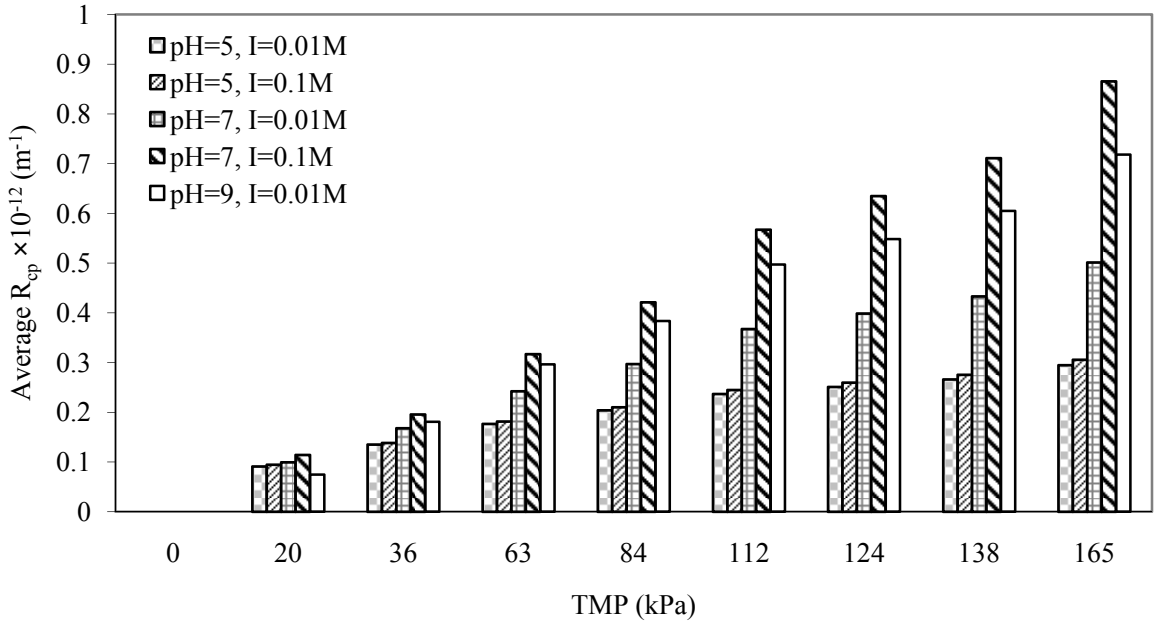

Figure 5.4 Estimated average concentration polarization resistance

According to TMP at pH7 and I=0.1M, the contribution of estimated R_{cp} increased with TMP but remained below 10% for 5 $g.L^{-1}$ BSA feed concentration but increased significantly when BSA feed concentration was increased to 15 and 30 $g.L^{-1}$ (Table 5.1). At 165 kPa TMP, estimated R_{cp} represented less than 10% for all pH and ionic strength considered in this study (Table 5.2). As expected (equations 5.2 and 5.3), the relative difference between the average reversible fouling,

R_{cp}, and wall concentration remained constant for each pH, ionic strength and TMP considered except pH 9 and I=0.01 M (Figure 5.4 and Figure 5.5). At TMP 165 kPa, for example, wall concentration at pH 7 and I=0.1M was about twice as large as the wall concentration at pH 9, I=0.01M and pH 7, I=0.01M. Estimated average concentration polarization resistance at pH 9, I=0.01M was 40% higher than the resistance at pH 7, I=0.01M. The behavior is due to the concentration profile inside the polarized layer. According to equations 5.2 and 5.3, concentration polarization resistance represents the thickness of the polarization layer and the associated BSA concentration profile. BSA concentration profile in the polarization layer at TMP 165 kPa is shown in Figure 5.6 (Note that the fiber radius is 5×10^{-4}m). Although pH 7 and 9 have similar BSA wall concentration, a thicker polarization layer with higher concentration profile was estimated at pH 9 explaining the higher R_{cp} observed at pH 9.

Table 5.1 Contribution of the individual components for the flux representation, equation 5.1 (model estimation) and BSA solution at pH 7, I= 0.1 M, and C_F=5 g.L^{-1} (feed concentration); * C_F=15 g.L^{-1}, ** C_F=30 g.L^{-1}

TMP (kPa)	Volume fraction (1-ε)	%Δπ/TMP	$R_G=(R_m+R_{cp}+R_{ad})$	% R_{cp}/ R_G	% R_{ad}/ R_G
20	0.01	1.9	6.6×10^{12}	1.8	5.4
63	0.04	2.2	7.6×10^{12}	4.2	17.0
112	0.08	3.0	9.2×10^{12}	6.2	28.6
138	0.10	3.4	10.1×10^{12}	7.1	33.4
165	0.13	3.9	11.0×10^{12}	7.9	37.4
200	0.16	4.8	12.3×10^{12}	9.3	41.8
200*	0.22	10.3	16.0×10^{12}	17.5	45.0
200**	0.26	16.1	19.3×10^{12}	25.2	43.6

Table 5.2 Effect of pH and ionic strength on the osmotic pressure and fouling resistance, TMP=165 kPa and C_F=5 g.L^{-1} (BSA feed concentration)

pH	I	C_w (g.L^{-1})	Volume fraction (1-ε)	%Δπ/TMP	$R_G=(R_m+R_{cp}+R_{ad})$	% R_{cp}/ R_G	% R_{ad}/ R_G
5	0.1	30.23	0.04	0.8	21.4×10^{12}	1.4	70.6
7	0.1	102.48	0.13	3.9	11.0×10^{12}	7.9	37.4
5	0.01	28.71	0.04	0.7	22.1×10^{12}	1.3	71.5
7	0.01	43.73	0.05	1.7	13.1×10^{12}	3.8	50.2
9	0.01	47.10	0.06	4.0	8.1×10^{12}	8.8	17.4

5.4.3 BSA concentration at the membrane surface

BSA concentration at the membrane surface (C_w) should reflect the TMP increase and the associated increasing convective flux to the membrane and the induced higher back transport by diffusion associated with the higher C_w. Estimated BSA wall concentration obtained is presented in Figure 5.5. At low ionic strength (I=0.01M) and for TMP higher than 20 kPa, C_w estimate was lowest at pH 5, increased at pH 7 and remained relatively constant at pH 9 (7% higher). At higher ionic strength (I=0.1M), a significant C_W increase was observed at pH 7 and TMP above 36 kPa which follows the highest concentration polarization resistance (at each TMP) estimated at similar pH and ionic strength. Estimated BSA concentration at the membrane surface did not change with ionic strength at pH 5 (Figure 5.5) because BSA is near its isoelectric point, has a zero net surface charge and will not involve ionic interactions resulting from the higher salt content. The pH effect at I=0.01M can be explained by the higher diffusion coefficient at pH 9 than at pH 7 (Figure 4.12). Estimates of C_w and the corresponding volume fraction presented in Table 5.2, summarize the effect of pH and ionic strength at 165kPa TMP.

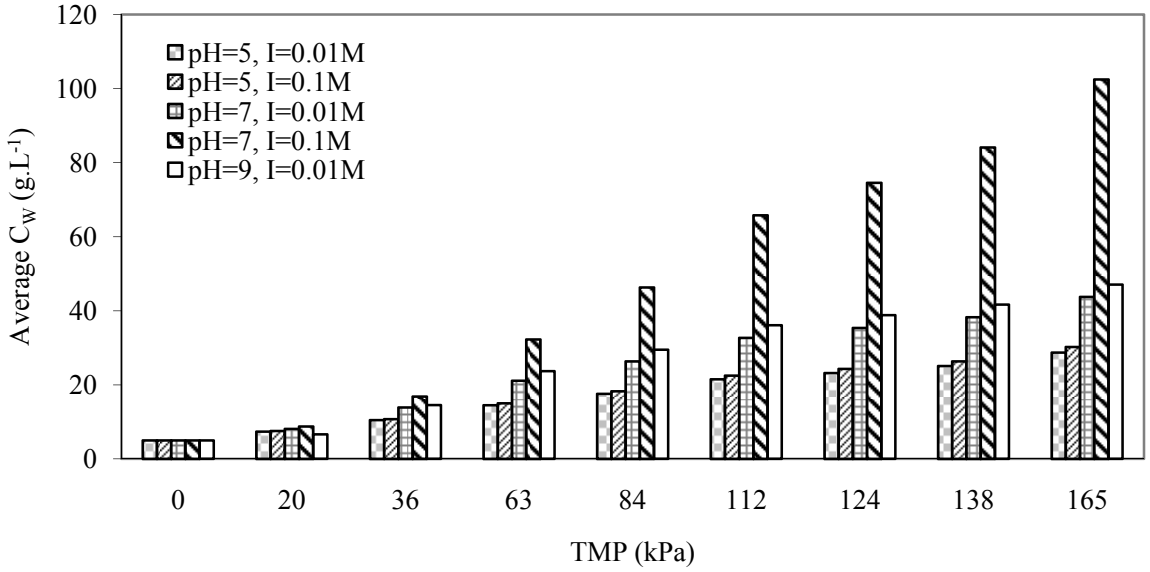

Figure 5.5 Estimated average BSA concentration at the membrane surface

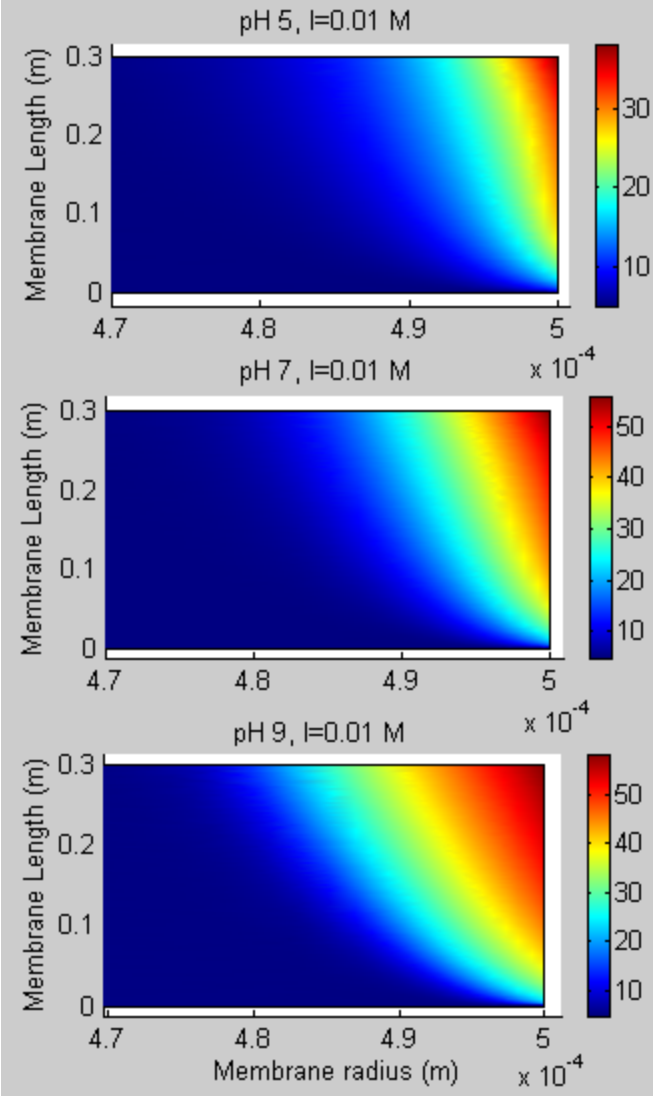

Figure 5.6 BSA concentration contour inside the hollow fiber

5.4.4 Protein adsorption resistance

Protein adsorption on the membrane surface is controlled by the interaction forces between the membrane and protein initially and protein-protein interactions once a protein monolayer has been formed. Due to the complexity of the adsorption phenomenon, an empirical relationship with one adjustable parameter (k_{ad}) was used in this work to describe BSA adsorption resistance (R_{ad}), equation 5.5. Figure 5.7 shows that R_{ad} increased with TMP, the highest increase is at pH 5 and relatively similar for both ionic strength and the lowest increase is at pH 9. The increase in R_{ad} with decreasing pH follows the permeate flux profile and suggests that BSA adsorption has a

significant contribution to fouling. This significant contribution to the total fouling was also seen in the relative magnitude of adsorption resistance compared to the concentration polarization resistance and the intrinsic membrane resistance (Table 5.1 and Table 5.2). For example, at low ionic strength (I=0.01M) and 165 kPa TMP, the estimated adsorption resistance represented 71% of the global resistance at pH 5 compared to 17% at pH 9. At 0.1M ionic strength, the estimated adsorption resistance represented also 71% compared to 37% at pH 7. The highest R_{ad} observed at pH 5 near the isoelectric point of BSA corresponded to zero net surface charge conditions would lead to BSA come close to a solid surface or with each other. Hydrophobic polyethersulphone (PES) membrane is negatively charged in a wide range of pH values (isoelectric point of 2.2-2.4 [120]), due to the anion adsorption from the solution or the ionization of the polar groups at the membrane surface [67]. Therefore, both protein and membrane are negatively charged above pH 5. The high resistance of the adsorbed protein layer on the membrane surface at pH 5 can also be explained by the structure and compactness of the layer(s). The adsorbed layers are densely packed at pH values close to the protein isoelectric point because of low intermolecular electrostatic repulsion [121,122]. Electrostatic repulsion between protein and membrane increases as pH increases resulting in lower protein adsorption. Maximum protein adsorption on the membrane at the protein isoelectic point is commonly reported [123-127]. Zeta potential and, consequently, electrical repulsion vary inversely with ionic strength due to charge shielding. Therefore, more adsorption is expected at higher ionic strength due to less repulsion between membrane and BSA. Ionic strength decreases not only the electrostatic force but also the van der Waals attractive force. The estimated Hamaker constant decreased by 80% with increasing the ionic strength from 0.01M to 0.1M (Figure 4.8). As was described in section 5.3.2, R_{ad} was measured experimentally at the end of BSA ultrafiltration at TMP 112kPa. Confirming the theoretical concepts, the measured R_{ad} decreased with ionic strength (Table 5. 3). Salgin et al. [128,129] also observed less BSA adsorption on the membrane surface at higher ionic strength. Similar results are found by Muramatsu and Kondo [130] for BSA adsorption on positively and negatively charged microcapsules. Less adsorption at higher ionic strength could be due to partial unfolding of BSA at the membrane surface during the adsorption. Less adsorption at higher ionic strength could also be explained by increasing protein stability that leads to less pronounced adsorption on the membrane surface. The parameter k_{ad} reflects the structure and compactness of the adsorbed protein layer as it represents the protein

tendency to be adsorbed on the membrane surface and was found to increase with decreasing pH and ionic strength (Table 5.4). Good agreement between the experimental and model prediction for adsorption resistance was observed (Table 5. 3).

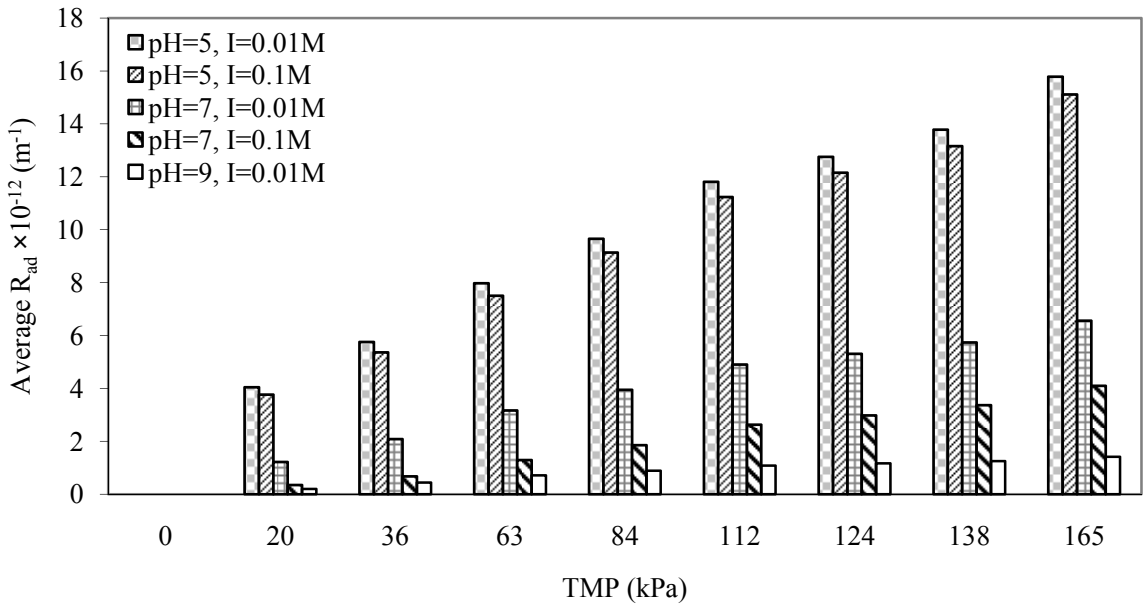

Figure 5.7 Estimated average protein adsorption resistance

Table 5.3 Experimental and theoretical protein adsorption resistance, R_{ad}, at 112 kPa

pH	Ionic strength (M)	Experimental $R_m \times 10^{-12}$ (m^{-1})	Experimental $R_{ad} \times 10^{-12}$ (m^{-1})	Estimated $R_{ad} \times 10^{-12}$ (m^{-1})
5	0.1	6.08± 0.01	11.0± 1.8	11.2
7	0.1	6.00± 0.02	4.0± 0.4	2.6
5	0.01	5.8	12.8	11.8
7	0.01	5.7	5.0	4.9
9	0.01	5.4	2.1	1.1

Table 5.4 Adjustable parameter for the protein adsorption model (equation 5.5)

pH	I (M)	$k_{ad} \times 10^{-10}$ ($m^2.kg^{-1}$)
5	0.1	50
7	0.1	4
5	0.01	55
7	0.01	15
9	0.01	3

5.4.5 Osmotic pressure

Osmotic pressure can also cause the flux to decline during UF by reducing the filtration driving force, the effective trans-membrane pressure (equation 5.1). Osmotic pressure is concentration dependant and can be calculated based on the protein concentration in the solution at the membrane surface (C_w). Osmotic pressure increased with TMP due to the increasing protein concentration at the membrane surface (Figure 5.8). The osmotic pressure increase was the highest at pH 9, I=0.01M and pH 7, I= 0.1M. The behavior was explained in detail earlier in section 5.4.3 (Figure 5.5). The contribution of osmotic pressure at various TMP presented in Table 5.1, showed a negligible contribution when compared to the TMP, at most 5% for 5 $g.L^{-1}$ BSA in the feed. It is also important to compare each resistance to the global resistance i.e. the combination of all the resistances to the permeate flux ($R_G=R_m+R_{cp}+R_{ad}$). Knowledge about the contribution of each factor to the permeate flux decline would offer different filtration operating conditions. Results (Table 5.1) show that at low TMP, R_{cp}, and R_{ad} are negligible compare to the membrane resistance; at TMP 20 kPa, R_{cp} and R_{ad} contributed only 7% of the global resistance, but as TMP increased, the contribution of R_{cp} and R_{ad} to the global resistance also increased. Concentration polarization resistance and osmotic pressure have a negligible effect on the permeate flux decline at pH 7, I=0.1M, and C_F=5$g.L^{-1}$ (feed concentration) and could have been ignored during the modeling. When feed concentration increased to 15$g.L^{-1}$, the effect of osmotic pressure and concentration polarization resistance on the permeate flux became more pronounced and neglecting them would result in large discrepancies in the permeate flux modeling. Increasing the feed concentration from 5 $g.L^{-1}$ to 30 $g.L^{-1}$ at TMP 200 kPa increased the osmotic pressure ratio and concentration polarization resistance from 4.81% and 9.3% to 16.15% and 25.23%, respectively (Table 5.1). These results become very important during filtration concentration operation where permeate would be withdrawn since protein

concentration increase during the process. Results also revealed how the dominant adsorption resistance becomes less important by changing TMP. The adsorption resistance was the limiting resistance at pH 5 at 0.01M and 0.1 M but osmotic pressure and concentration polarization are negligible factors to decrease the permeate flux (Table 5.2). The contribution of the adsorption resistance became less pronounced as pH increased. For example, at pH 9, the adsorption resistance was only twice as large as the concentration polarization resistance and the ratio decreases with increasing TMP.

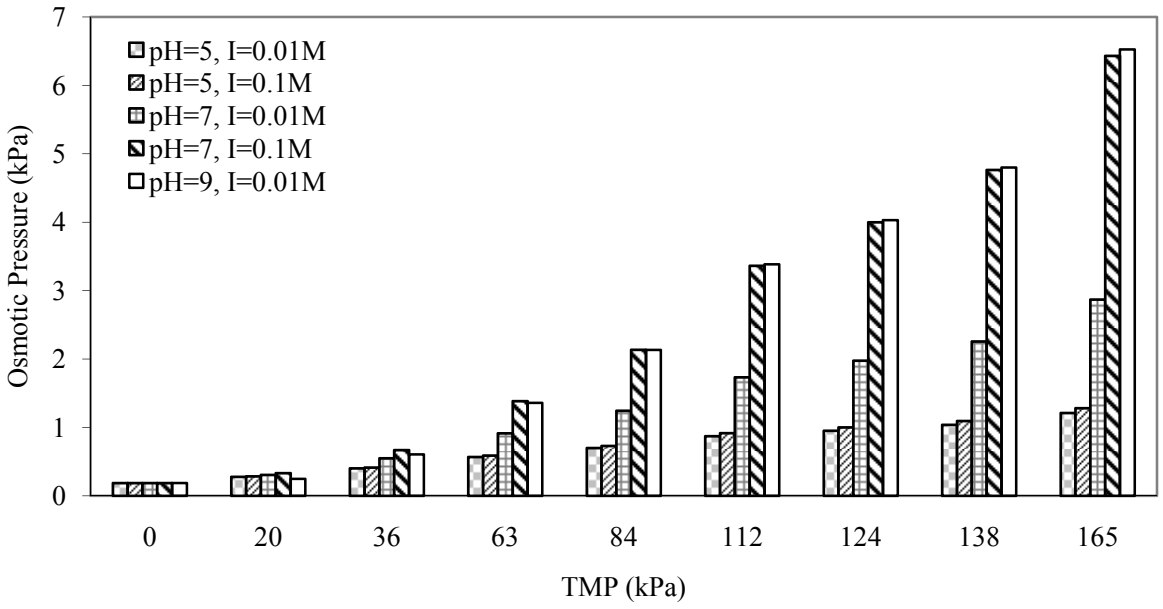

Figure 5.8 Estimated osmotic pressure at the membrane surface

5.4.6 Effect of TMP on the local characteristics in the membrane fiber

CFD modeling provided information on the spatial properties of the filtration operation. Permeate velocity, BSA wall concentration, polarization layer thickness and concentration polarization resistance estimated along the fiber length for BSA total recycle ultrafiltration at pH 7 and 0.1M ionic strength is presented in Figure 5.9-Figure 5.12. Permeate velocity decreased along the fiber regardless of TMP (Figure 5.9). Permeate velocity decreased linearly at low TMP mainly because osmotic pressure, concentration polarization resistance, and protein adsorption resistance (equation 5.1) were negligible and Δp (the significant driving force) decreased linearly

along the membrane due to the pressure drop. At high TMP, the axial variation of permeate velocity could be divided in two stages. In the upstream region close to the fiber inlet, the estimated permeate velocity decrease was very fast and the decrease slowed gradually in the downstream region due to the concentration profile along the membrane.

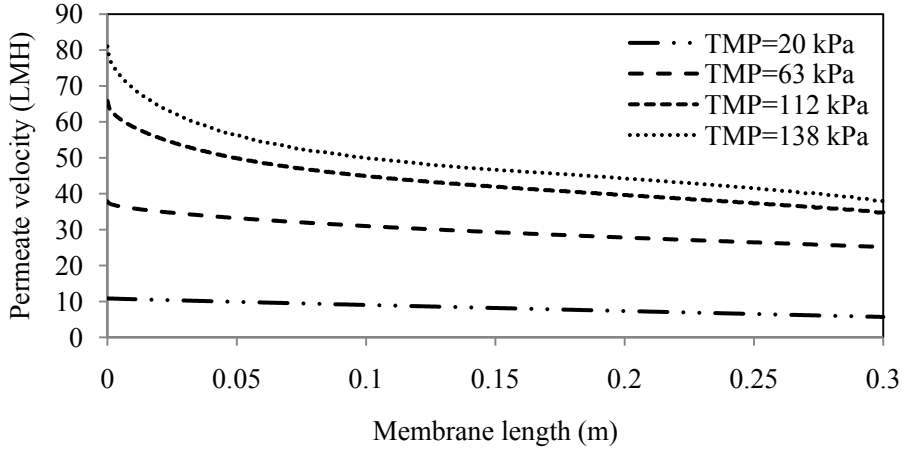

Figure 5.9 Estimated permeate velocity along the membrane at pH=7, I=0.1M

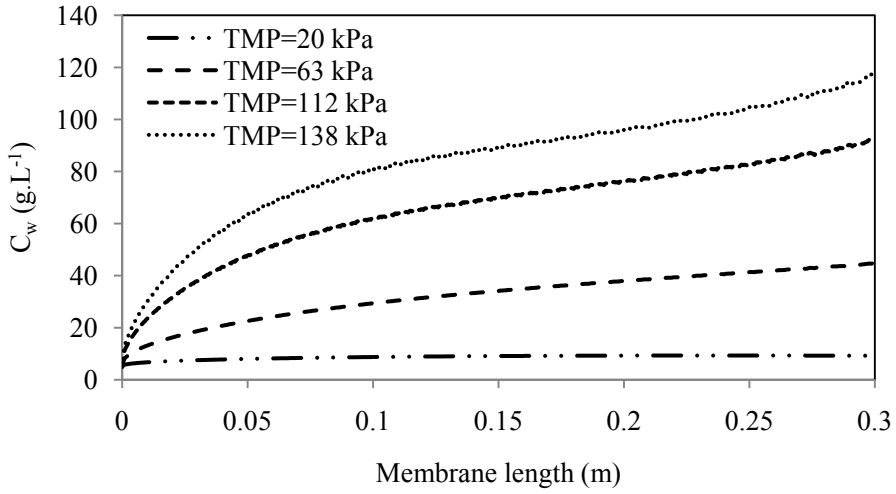

Figure 5.10 Estimated wall concentration along the membrane at pH=7, I=0.1 M

The protein concentration at the membrane surface, C_w, increased along the membrane regardless of TMP (Figure 5.10), and agrees with previous observations reported in literature [40,62,131,132]. As for the permeate velocity, the increasing protein concentration at the wall

along the membrane (at high TMP) could be divided into two stages, a sharp increase in the upstream region followed by a gradual increase in the downstream region. Estimated protein concentration at the wall at the fiber outlet (downstream) are 1.8 and 23 times higher than the inlet wall concentration estimates at TMP 20 kPa and 138 kPa respectively. For TMP 138 kPa at an arbitrary distance from the inlet, z=0.1m for example, wall protein concentration increased to 81 g.L^{-1} (70% of the wall concentration at the outlet) indicating that the rate of increase of protein wall concentration in the upstream region was much higher than in the downstream region. Decreasing TMP weakened such a variation pattern by lowering the rate of increase of protein wall concentration in the upstream region. Conversely, estimates of the polarization layer thickness (δ) were TMP independent for TMP higher than 63 kPa, and increased along the membrane (Figure 5.11). The estimated average polarization layer thickness ($\frac{1}{L}\int_0^L \delta dz$) at high TMP, 1.9×10^{-5} to 2.3×10^{-5} m for different pH and ionic strength conditions, showed negligible effects. The estimated thickness was about 25 times smaller than the fiber radius which agrees with literature [62]. Since both C_w and δ increased along the membrane and C_w increased with TMP (Figure 5.10 and Figure 5.11), the concentration polarization resistance, R_{cp}, would increase along the membrane and with TMP (Equations 5.2 and 5.3) as shown in Figure 5.12. In the upstream region, R_{cp} increased at a slower rate compared to the protein wall concentration (Figure 5.10). Protein adsorption resistance (Figure 5. 13) behavior was similar to the protein wall concentration but different magnitude according to equation 5.5.

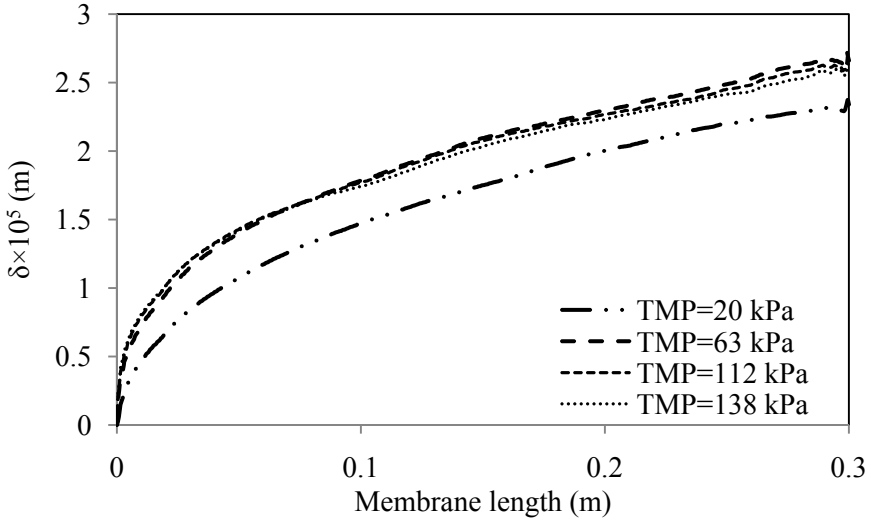

Figure 5.11 Estimated thickness of concentration boundary layer along the membrane at pH=7,

I=0.1 M

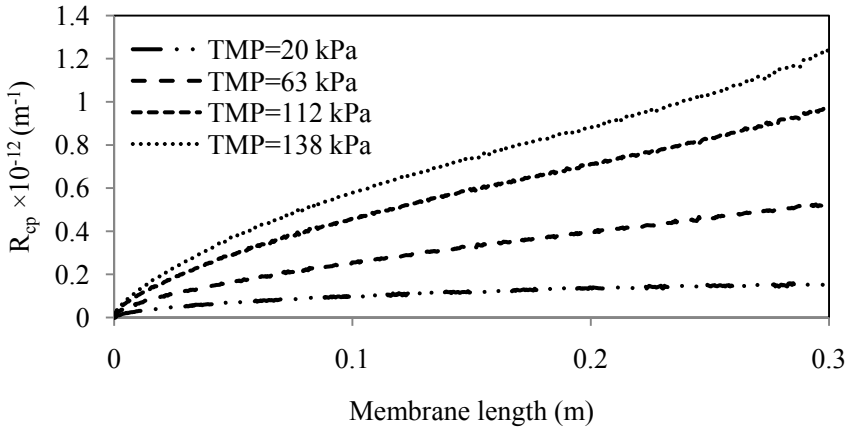

Figure 5.12 Estimated concentration polarization resistance along the membrane at pH=7, I=0.1 M

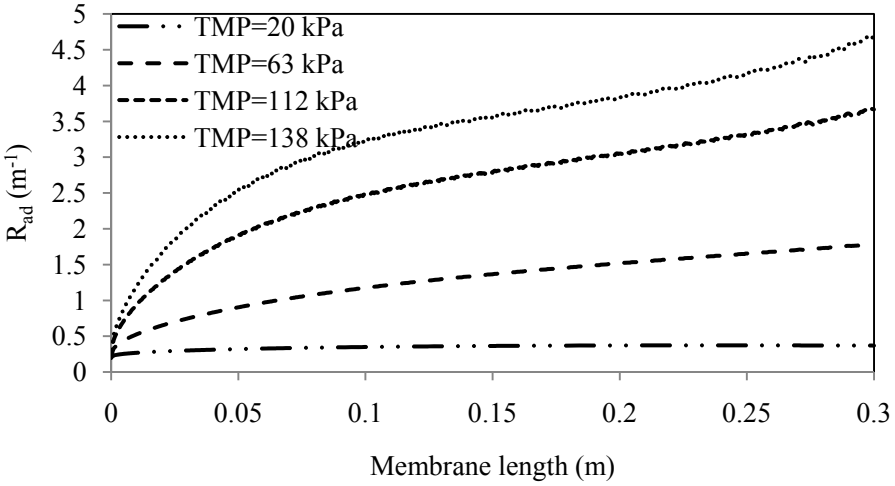

Figure 5.13Estimated protein adsorption resistance along the membrane at pH=7, I=0.1 M

5.4.7 Effect of constant viscosity and constant diffusion coefficient

Effects of constant viscosity and constant diffusion coefficient on the permeate flux were investigated at pH 7 and I=0.1M with constant viscosity of 0.001 Pa.s and diffusion coefficient

of 6.7×10^{-11} $m^2.s^{-1}$ (Brownian diffusion coefficient, D_B) (Figure 5.14). Overestimation less than 1% in permeate flux was obtained when constant diffusion coefficient was considered in the model. Calculation with constant diffusion coefficient was also performed for pH 7 and I=0.01M. Permeate flux was underestimated; at TMP 165kPa, the maximum underestimation was 12%. Diffusion coefficient estimates, presented in Figure 4.12, explain the difference observed at pH 7 and I=0.1M. At I=0.1M, diffusion coefficient decreases slightly with concentration causing the concentration to decrease at the membrane surface. Therefore, higher wall concentration and consequently lower permeate flux when the concentration dependant diffusion coefficient was considered are expected. Since diffusion coefficient decreases slightly with concentration at pH 7 and I=0.01M, assuming a constant value of Brownian diffusion coefficient did not cause any overestimation in the permeate flux. At pH 7 and I=0.01M, the estimated diffusion coefficient of BSA exhibited a maximum and then decreased sharply with concentration. For BSA concentration up to 276 $g.L^{-1}$ (polarization layer has a high protein concentration), the diffusion coefficient was greater than D_B, ($D/D_B>1$). Model prediction showed a maximum wall concentration of $43g.L^{-1}$ at TMP 165kPa (Figure 5.5). Therefore, estimated diffusion coefficient in the polarization layer was higher than D_B resulting in lower wall concentration and higher permeate flux. The permeate flux obtained with constant viscosity was under predicted (13%) for TMP higher than 60 kPa, and there was no difference in permeate flux observed up to TMP 60 kPa (Figure 5.14). Since wall concentration was small up to TMP 63 kPa (Figure 5.5), assuming a constant viscosity in the model did not cause a significant error in permeate flux estimates.

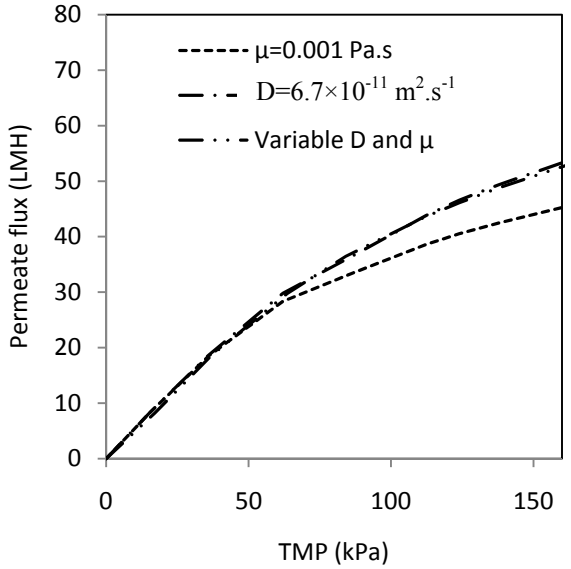

Figure 5.14 Estimated permeate flux applying constant diffusion coefficient and viscosity

5.5 Conclusions

A computational fluid dynamics (CFD) model was developed to investigate the local flow behavior, concentration profile, and membrane fouling during hollow fiber BSA ultrafiltration in total recycle mode. Microscopic characteristics such as protein interactions were coupled with the macroscopic equations such as equation of motion which govern the filtration process. Osmotic pressure, concentration polarization resistance and protein adsorption on the membrane surface were considered in the permeate flux modeling. Diffusion coefficient and osmotic pressure of the protein were considered as a function of BSA concentration based on pH and ionic strength conditions. The membrane was assumed to be fully retentive to BSA as the membrane pore size was much smaller than the protein size. A novel approach was applied to estimate the concentration polarization resistance based on the profile and the thickness of the concentration polarization layer. Good agreement between the experimental permeate flux data and the model prediction was obtained for pH between 5 and 9 and 0.01-0.1 M ionic strength. The model indicated that permeate flux at pH 5 was limited by protein adsorption on the membrane surface. At this pH, concentration polarization resistance and osmotic pressure had negligible effect on the permeate flux decline even at high TMP suggesting that computations of osmotic pressure and concentration polarization resistance are not necessary. The high protein adsorption resistance was caused by the densely packed adsorbed protein layers on the

membrane since intermolecular electrostatic repulsion was low at pH 5. In contrast, the model suggested very low resistance due to protein adsorption at pH 9. Osmotic pressure and concentration polarization were found to be as important as protein adsorption. At pH 7, protein adsorption was the dominant factor for the permeate flux decline at low TMP, but concentration polarization and osmotic pressure became important at high TMP. Increasing the ionic strength increased the permeate flux at pH 7, but no significant change in permeate flux was observed by increasing the ionic strength at pH 5. Effect of constant viscosity and diffusion coefficient on permeate flux showed that assuming a constant diffusion coefficient in the calculation affects the permeate flux differently depending on the pH and ionic strength. Assuming a constant value for viscosity resulted in 13% underestimation in permeate flux (at high TMP) justifying the necessity for concentration dependant viscosity and diffusion coefficient. The feed concentration strongly increased the contribution of osmotic pressure and concentration polarization on the permeate flux decline due to the high BSA accumulation on the membrane surface. Since membrane fouling mechanisms depend on hydrodynamic filtration conditions, solution properties, and membrane chemistry, different operating policies should be applied to improve the permeate flux. The fouling behavior at pH 5 suggests that module design and system hydrodynamics do not affect the filtration process. Performance of the filtration can be improved by modifying the surface chemistry of the membrane which is responsible for the membrane-solute interactions (i.e. low affinity membranes). Since a linear increase in permeate flux with TMP was observed for the solution at pH 9, cost optimization should be performed to obtain the optimum TMP. For the solution at pH 7, permeate flux could be improved by modifying the membrane surface chemistry followed by process optimization to find the optimum hydrodynamic filtration conditions.

Chapter 6

Major outcomes and recommendations

6.1 Major outcomes

This thesis presented the application of Computational Fluid Dynamics and multi-scale modeling for investigating the effect of hydrodynamic parameters and physicochemical properties of the solution and the membrane on the fouling behavior during ultrafiltration of protein solutions. This chapter summarizes the major findings of this study.

Effect of electroacidification pretreatment on the fouling behavior during soy protein hollow fiber ultrafiltration was modeled using a computational fluid modeling approach. Fouling behavior was found to be different between the electroacidifed (pH 6) and non-electroacidified (pH 9) soy protein extracts. The reduced negative charge for the electroacidified soy protein extract was associated with a more important protein adsorption and the more severe irreversible fouling. The model provided an accurate prediction of the experimental permeate flux, the protein concentration and the fouling dynamics during the concentration process. Transient reversible and irreversible fouling resistances were predicted accurately. The model showed a uniform bulk protein concentration along the fiber but spatially non-uniform protein concentration profile near the membrane surface where the protein concentration was high. The model estimates showed that increasing the average axial velocity would result a moderate increase in the permeate velocity. In contrast, increasing the TMP increased the permeate flux more substantially.

Experimental results showed that polarization layer was not the only phenomenon affecting the permeate flux decline at the beginning of the filtration; the irreversible fouling was an important factor to be considered for the concentration of soy protein extracts. The irreversible fouling at the beginning of the filtration contributed to 20% and 40% of the total fouling for non-electroacidified and electroacidified soy protein extracts, respectively. The model estimates suggested that the irreversible fouling is associated with the protein adsorption since a plateau is

estimated for both types of extracts. Therefore, the improvement of the concentration of soy protein extracts subjected to electroacidification will be achieved by manipulating the interactions leading to irreversible fouling, ie between the proteins and the membrane surface.

The model sensitivity analysis showed that transport properties such as viscosity and diffusion coefficient significantly affect the protein concentration profile at the membrane surface.

Chapter 4 was motivated by the desire to estimate the osmotic pressure and diffusion coefficient of protein molecules as a function of protein concentration, pH and ionic strength in order to improve the CFD model presented in chapter 3. A mathematical model was generated to estimate the osmotic pressure and diffusion coefficient of protein molecules, verified against experimental data for BSA, and was finally developed for soy glycinin, one of the major proteins in soy.

Electrostatic force and hydration force between proteins were found to have respectively considerable and negligible effects on the osmotic pressure of the proteins. Results also showed that osmotic pressure increased as pH diverged from the protein isoelectric point. Increasing the ionic strength, however, reversed the effect by shielding charges, causing molecular contraction and thereby decreasing the osmotic pressure.

Results showed that osmotic pressure of soy glycinin is much lower than that of BSA. The protein concentration corresponding to the maximum osmotic pressure was found to be lower for the soy glycinin compared to that of BSA explaining that the transition of dispersion to solid state occurs at lower concentration for soy glycinin. It confirmed the experimental results that BSA is highly soluble in water compared to soy glycinin. The maximum osmotic pressure at high ionic strength (1M) for example, was observed at protein concentrations around 550 $g.L^{-1}$ and 300 $g.L^{-1}$ for BSA and soy glycinin, respectively.

Two different trends for diffusion coefficient at specified pH and ionic strength were observed for both proteins; diffusion coefficient values that decreased with protein concentration and diffusion coefficient values that passed through a maximum. When zeta potential of the protein

was low, either at high ionic strength or at pH close to the protein isoelectric point, diffusion coefficient decreased with protein concentration and no maximum was observed.

Artificial Neural Network (ANN) was an efficient tool to relate the estimated osmotic pressure of the proteins to the protein concentration, pH, and Ionic strength. Despite the inherent nonlinearity of the problem, ANN was found to be highly precise in predicting the osmotic pressure in a wide range of pH, ionic strength, and protein concentration.

A rigorous CFD model based on a description of protein interactions was developed to predict membrane fouling during ultrafiltration of BSA. BSA UF was performed in a total recycle operation mode in order to maintain a constant feed concentration. To establish a more comprehensive model and thereby alleviate the shortcomings of previous filtration models in literature, this model considered three major phenomena causing the permeate flux decline during BSA ultrafiltration: osmotic pressure, concentration polarization, and protein adsorption on the membrane surface. A novel mathematical approach was introduced to predict the concentration polarization resistance on the membrane. The resistance was estimated based on the concentration and thickness profile of the polarization layer on the membrane obtained from the solution of the equation of motion and continuity equation at a previous time step. Permeate flux was updated at each time step according to the osmotic pressure, concentration polarization resistance, and protein adsorption resistance. This model had the ability to show how microscopic phenomena such as protein interactions can affect the macroscopic behaviors such as permeate flux and provided detailed information about the local characteristics on the membrane. The theoretical model along with the experimental data revealed that protein adsorption on the membrane surface limited the permeate flux at pH 5. Concentration polarization and osmotic pressure was found to have negligible effects on the permeate flux decline even at high TMP. Osmotic pressure and concentration polarization, however, were found to be as important as protein adsorption on the membrane surface during the filtration at pH 9. Protein adsorption resistance was the dominant factor to the permeate flux decline at pH 7 and low TMP; the contribution, however, decreased with TMP. Increasing the ionic strength increased the permeate flux at pH 7, but no significant change in permeate flux was observed by increasing the ionic strength at pH 5. The feed concentration strongly increased the contribution

of osmotic pressure and concentration polarization resistance to the permeate flux decline due to the high BSA accumulation on the membrane surface. Therefore, different strategies were recommended to improve the permeate flux depending on the hydrodynamic parameters and physicochemical properties of the solution.

6.2 Future works

Based on the studies carried out in this research, the following recommendations for future studies are proposed:

- Multi-component CFD modeling of the hollow fiber ultrafiltration process for soy protein concentration considering mineral and carbohydrate transport.
- Membrane surface modification to decrease the irreversible fouling during UF of soy protein solution at pH 6.
- Experimental validation of the estimated osmotic pressure and diffusion coefficient for soy glycinin.
- Quantification of membrane adsorption resistance considering membrane-protein interactions.

Permissions

Reprint License agreement

Rightslink® by Copyright Clearance Ce...

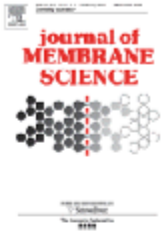

Title:	Fouling behavior of electroacidified soy protein extracts during cross-flow ultrafiltration using dynamic reversible–irreversible fouling resistances and CFD modeling
Author:	Amin Reza Rajabzadeh, Christine Moresoli, Bernard Marcos
Publication:	Journal of Membrane Science
Publisher:	Elsevier
Date:	30 September 2010

Order Completed

Thank you very much for your order.

This is a License Agreement between Amin Reza Rajabzadeh ("You") and Elsevier ("Elsevier"). The license consists of your order details, the terms and conditions provided by Elsevier, and the payment terms and conditions.

Get the printable license.

License Number	2600301377671
License date	Feb 01, 2011
Licensed content publisher	Elsevier
Licensed content publication	Journal of Membrane Science
Licensed content title	Fouling behavior of electroacidified soy protein extracts during cross-flow ultrafiltration using dynamic reversible–irreversible fouling resistances and CFD modeling
Licensed content author	Amin Reza Rajabzadeh, Christine Moresoli, Bernard Marcos
Licensed content date	30 September 2010
Licensed content volume number	361
Licensed content issue number	1-2
Number of pages	15
Type of Use	reuse in a thesis/dissertation
Portion	full article
Format	both print and electronic
Are you the author of this Elsevier article?	Yes
Will you be translating?	No
Order reference number	
Title of your thesis/dissertation	Membrane Fouling During Hollow Fiber Ultrafiltration of Protein Solutions: Computational Fluid Modeling and Physicochemical Properties
Expected completion date	Feb 2011
Estimated size (number of pages)	43
Elsevier VAT number	GB 494 6272 12
Permissions price	0.00 USD
VAT/Local Sales Tax	0.0 USD / 0.0 GBP
Total	0.00 USD

References

[1] P. Hannam, G. Penne, B. Allison, A. Wildeman, J. Weeler, E. DiEmanuele, D. Harrietha, L.Thaker. Soy 20/20 Project Annual Report. Ontario Soybean Growers, University of Guelph, Agriculture and Agri-Food Canada, Ontario Ministry of Agriculture. (2003) 1.

[2] Z. Alibhai, M. Mondor, C. Moresoli, D. Ippersiel, and F. Lamarche. Production of soy protein concentrates/isolates: traditional and membrane technologies. Desalination, 191 (2006) 351.

[3] L. KeShun, Soybeans: Chemistry, Technology, and Utilization, New York: Chapman&Hall, (1999) 532.

[4] M. Mondor, D. Ippersiel, F. Lamarche, and J.I. Boye. Effect of electro-acidification treatment and ionic environment on soy protein extract particle size distribution and ultrafiltration permeate flux. J.Membr.Sci., 231 (2004) 169.

[5] M. Mondor, D. Ippersiel, F. Lamarche, and J.I. Boye. Production of soy protein concentrates using a combination of electroacidification and ultrafiltration. J.Agric.Food Chem, 52 (2004) 6991.

[6] Raja Ghosh, Protein Bioseparation using ultrafiltration, Imperial college press (2003) 166.

[7] M. Cheryan, Ultrafiltration and microfiltration handbook, Lancaster, Pa., Technomic Pub. Co., 1998.

[8] http://www.spectrumlabs.com/filtration/Edge.html. SPECTRUM® LABORATORIES, (1995-2008).

[9] G.1. Bolton, D.1. LaCasse, and R.1. Kuriyel. Combined models of membrane fouling: Development and application to microfiltration and ultrafiltration of biological fluids. J.Membr.Sci., 277 (2006) 75.

[10] C.-C. Ho and A.L. Zydney. A Combined Pore Blockage and Cake Filtration Model for Protein Fouling during Microfiltration. J. Colloid Interface Sci, 232 (2000) 389.

[11] C. Ho, A.L. Zydney. Transmembrane pressure profiles during constant flux microfiltration of bovine serum albumin. J.Membr.Sci., 209 (2002) 363.

[12] W.R. Bowen, J.I. Calvo, and A. Hernandez. Steps of membrane blocking in flux decline during protein microfiltration. J.Membr.Sci., 101 (1995) 153.

[13] A.D. Marshall, P.A. Munro, and G. Tragardh. Effect of protein fouling in microfiltration and ultrafiltration on permeate flux, protein retention and selectivity: A literature review. Desalination, 91 (1993) 65.

[14] P. Bacchin, D. Si-Hassen, V. Starov, M.J. Clifton, and P. Aimar. A unifying model for concentration polarization, gel-layer formation and particle deposition in cross-flow membrane filtration of colloidal suspensions. Chemical Engineering Science, 57 (2002) 77.

[15] Handbook of membrane separations : chemical, pharmaceutical, food, and biotechnological applications, Boca Raton, Boca Raton : CRC Press, 2009.

[16] J.A. Howell. M.S. Le, Progress in Food Engineering: Solid Extraction Isolation and Purification, Texturization: Proceedings of A European Symposium of the Food Working Party of The E.F.C.E. / C. Cantarelli and C. Peri, Editors, Kuesnacht, Switzerland : Forster, C1983, Kuesnacht, Switzerland: Forster, C1983, 1983.

[17] J. A. Howell, V. Sanchez, R. W. Field, Membranes in Bioprocessing, Blackie Academic And Professional (1993) 336.

[18] M. CHERYAN. Mass transfer characteristics of hollow fiber ultrafiltration of soy protein systems. J.Food Process Eng., 1 (1977) 269.

[19] M. Porter. Handbook of separation techniques for chemical engineers. (1979).

[20] E.C. Eckstein, D.G. Bailey, and A.H. Shapiro. Self-diffusion of particles in shear flow of a suspension. J.Fluid Mech., 79 (1977) 191.

[21] W.R. Bowen, P.M. Williams. The Osmotic Pressure of Electrostatically Stabilized Colloidal Dispersions. J.Colloid Interface Sci., 184 (1996) 241.

[22] W.R. Bowen, F. Jenner. Dynamic ultrafiltration model for charged colloidal dispersions: a Wigner-Seitz cell approach. Chemical Engineering Science, 50 (1995) 1707.

[23] W.R. Bowen, P.M. Williams. Dynamic ultrafiltration model for proteins: A colloidal interaction approach. Biotechnol.Bioeng., 50 (1996) 125.

[24] W.R. Bowen, P.M. Williams. Quantitative predictive modelling of ultrafiltration processes: Colloidal science approaches. Adv.Colloid Interface Sci., 134-135 (2007) 3.

[25] W.R. Bowen, A. Mongruel. Calculation of the collective diffusion coefficient of electrostatically stabilised colloidal particles. Colloids Surf.Physicochem.Eng.Aspects, 138 (1998) 161.

[26] S. Ma, S.C. Kassinos, and D. Kassinos. Direct simulation of the limiting flux: I. Interpretation of the experimental results. J.Membr.Sci., 337 (2009) 81.

[27] Y. Bessiere, D.F. Fletcher, and P. Bacchin. Numerical simulation of colloid dead-end filtration: Effect of membrane characteristics and operating conditions on matter accumulation. J.Membr.Sci., 313 (2008) 52.

[28] P. Bacchin, B. Espinasse, Y. Bessiere, D.F. Fletcher, and P. Aimar. Numerical simulation of colloidal dispersion filtration: description of critical flux and comparison with experimental results. Desalination, 192 (2006) 74.

[29] W.R. Bowen, H.N.S. Yousef, and J.I. Calvo. Dynamic crossflow ultrafiltration of colloids: A deposition probability cake filtration approach. Separation and Purification Technology, 24 (2001) 207.

[30] H.M. Yeh, J.H. Dong, and M.Y. Shi. Momentum balance analysis of flux and pressure declines in membrane ultrafiltration along tubular modules. J.Membr.Sci., 241 (2004) 335.

[31] A.R. Secchi, K. Wada, and I.C. Tessaro. Simulation of an ultrafiltration process of bovine serum albumin in hollow-fiber membranes. J.Membr.Sci., 160 (1999) 255.

[32] B. Sarkar, S. DasGupta, and S. De. Flux decline during electric field-assisted cross-flow ultrafiltration of mosambi (Citrus sinensis (L.) Osbeck) juice. J.Membr.Sci., 331 (2009) 75.

[33] M. Chikhi, A. Meniai, F. Balaska, and M. Bencheikh-Lehocine. Modeling of the ultrafiltration of a Dextran T500 solution in a tubular membrane module. Chemical Engineering and Technology, 31 (2008) 501.

[34] R.J. Hunter, Introduction to modern colloid science, Oxford ; New York, Oxford ; New York : Oxford University Press, 1993.

[35] H. Ohshima, K. Furusawa, Electrical phenomena at interfaces : fundamentals, measurements, and applications. New York, M. Dekker, 1998.

[36] H.C. Hamaker. London-van der Waals attraction between spherical particles. Physica, 4 (1937) 1058.

[37] A. Subramani, S. Kim, and E.M.V. Hoek. Pressure, flow, and concentration profiles in open and spacer-filled membrane channels. J.Membr.Sci., 277 (2006) 7.

[38] A. Pak, T. Mohammadi, S.M. Hosseinalipour, and V. Allahdini. CFD modeling of porous membranes. Desalination, 222 (2008) 482.

[39] L. Huang, M.T. Morrissey. Finite element analysis as a tool for crossflow membrane filter simulation. J.Membr.Sci., 155 (1999) 19.

[40] D.E.1. Wiley, D.F. Fletcher. Techniques for computational fluid dynamics modelling of flow in membrane channels. J.Membr.Sci., 211 (2003) 127.

[41] B. Marcos, C. Moresoli, J. Skorepova, and B. Vaughan. CFD modeling of a transient hollow fiber ultrafiltration system for protein concentration. J.Membr.Sci., 337 (2009) 136.

[42] R. Ghidossi, J.V. Daurelle, D. Veyret, and P. Moulin. Simplified CFD approach of a hollow fiber ultrafiltration system. Chem.Eng.J., 123 (2006) 117.

[43] P. Schausberger, N. Norazman, H. Li, V. Chen, and A. Friedl. Simulation of protein ultrafiltration using CFD: Comparison of concentration polarisation and fouling effects with filtration and protein adsorption experiments. J.Membr.Sci., 337 (2009) 1.

[44] A. Berman. Laminar Flow in Channels with porous walls. Journal of Applied Physics, 24 (1953).

[45] J. Granger, J. Dodds, and N. Midoux. Laminar flow in channels with porous walls. Chemical Engineering Journal and the Biochemical Engineering Journal, 42 (1989) 193.

[46] S. Tu, V. Ravindran, and M. Pirbazari. A pore diffusion transport model for forecasting the performance of membrane processes. J.Membr.Sci., 265 (2005) 29.

[47] N.S.K. Kumar, M.K. Yea, and M. Cheryan. Ultrafiltration of soy protein concentrate: performance and modelling of spiral and tubular polymeric modules. J.Membr.Sci., 244 (2004) 235.

[48] J. Skorepova, and C. Moresoli, Carbohydrate and Mineral Removal during the Production of Low-Phytate Soy Protein Isolate by Combined Electroacidification and High Shear Tangential Flow Ultrafiltration. Journal of Agricultural and Food Chemistry, 55 (2007) 5645.

[49] J. Skorepová, Effect of electroacidification on ultrafiltration performance and physicochemical properties of soy protein extracts, PhD Thesis, Waterloo, ON., University of Waterloo, 2008.

[50] T. Furukawa, K. Kokubo, K. Nakamura, and K. Matsumoto. Modeling of the permeate flux decline during MF and UF cross-flow filtration of soy sauce lees. J.Membr.Sci., 322 (2008) 491.

[51] K. Damak, A. Ayadi, B. Zeghmati, and P. Schmitz. A new Navier-Stokes and Darcy's law combined model for fluid flow in crossflow filtration tubular membranes. Desalination, 161 (2004) 67.

[52] P. Schmitz, M. Prat. 3-D laminar stationary flow over a porous surface with suction: description at pore level. AICHE J., 41 (1995) 2212.

[53] T.R. Noordman, K. Kooiker, W. Bel, M. Dekker, and J.A. Wesselingh. Concentration of aqueous extracts of defatted soy flour by ultrafiltration - Effect of suspended particles on the filtration flux. J.Food Eng., 58 (2003) 135.

[54] C. Ho, A.L. Zydney. A Combined Pore Blockage and Cake Filtration Model for Protein Fouling during Microfiltration . Journal of Colloid and Interface Science, 232 389.

[55] J.E. Kilduff, S. Mattaraj, and G. Belfort. Flux decline during nanofiltration of naturally-occurring dissolved organic matter: effects of osmotic pressure, membrane permeability, and cake formation. J.Membr.Sci., 239 (2004) 39.

[56] H. Choi, K. Zhang, D.D. Dionysiou, D.B. Oerther, and G.A. Sorial. Influence of cross-flow velocity on membrane performance during filtration of biological suspension. J.Membr.Sci., 248 (2005) 189.

[57] M. Li, Y. Zhao, S. Zhou, W. Xing, and F.S. Wong. Resistance analysis for ceramic membrane microfiltration of raw soy sauce. J.Membr.Sci., 299 (2007) 122.

[58] P. Aimar, C. Taddei, J. Lafaille, and V. Sanchez. Mass transfer limitations during ultrafiltration of cheese whey with inorganic membranes. J.Membr.Sci., 38 (1988) 203.

[59] K.W.K. Yee, D.E. Wiley, and J. Bao. A unified model of the time dependence of flux decline for the long-term ultrafiltration of whey. J.Membr.Sci., 332 (2009) 69.

[60] E. Matthiasson. Role of Macromolecular Adsorption in Fouling of Ultrafiltration Membranes. J.Membr.Sci., 16 (1982) 23.

[61] M. Turker, J. Hubble. Membrane Fouling in A Constant-Flux Ultrafiltration Cell. J.Membr.Sci., 34 (1987) 269.

[62] A.L.1. Ahmad, K.K.1. Lau, M.Z.A.1. Bakar, and S.R.A.1. Shukor. Integrated CFD simulation of concentration polarization in narrow membrane channel. Comput.Chem.Eng., 29 (2005) 2087.

[63] K.H. Keller, E.R. Canales, and S.I. Yum. Tracer and mutual diffusion coefficients of proteins. J.Phys.Chem., 75 (1971) 379.

[64] D.H.(.H. Everett, Basic principles of colloid science, London, Royal Society of Chemistry, 1988.

[65] W.R. Bowen, F. Jenner. Theoretical descriptions of membrane filtration of colloids and fine particles. An assessment and review. Adv.Colloid Interface Sci., 56 (1995) 141.

[66] G. Cao, Nanostructures & nanomaterials : synthesis, properties & applications, London, Imperial College Press, 2004.

[67] M. Pontie, X. Chasseray, D. Lemordant, and J.M. Laine. The streaming potential method for the characterization of ultrafiltration organic membranes and the control of cleaning treatments. J.Membr.Sci., 129 (1997) 125.

[68] X.M. He, D.C. Carter. Atomic structure and chemistry of human serum albumin. (1992).

[69] D.C. Carter, J.X. Ho, Structure of Serum Albumin, in C.B. Anfinsen, John T. Edsall,Frederic M.Richards and David S.Eisenberg (Ed.), Advances in Protein Chemistry, Academic Press, 1994.

[70] M. Adachi, Y. Takenaka, A.B. Gidamis, B. Mikami, and S. Utsumi. Crystal structure of soybean proglycinin A1aB1b homotrimer. J.Mol.Biol., 305 (2001) 291.

[71] J. Brooks, C. Morr. Current aspects of soy protein fractionation and nomenclature. J.Am.Oil Chem.Soc., 62 (1985) 1347.

[72] R. Badley, D. Atkinson, H. Hauser, D. Oldani, J. Green, and J. Stubbs. The structure, physical and chemical properties of the soy bean protein glycinin. Biochimica et Biophysica Acta (BBA)-Protein Structure, 412 (1975) 214.

[73] P. Schausberger, N. Norazman, H. Li, V. Chen, and A. Friedl. Simulation of protein ultrafiltration using CFD: Comparison of concentration polarisation and fouling effects with filtration and protein adsorption experiments. J.Membr.Sci., 337 (2009) 1.

[74] V.L. Vilker, C.K. Colton, K.A. Smith, and D.L. Green. The osmotic pressure of concentrated protein and lipoprotein solutions and its significance to ultrafiltration. J.Membr.Sci., 20 (1984) 63.

[75] A. Achouri, J.I. Boye, V.A. Yaylayan, and F.K. Yeboah. Functional properties of glycated soy 11S glycinin. J.Food Sci., 70 (2005) C269.

[76] M. Adachi, J. Kanamori, T. Masuda, K. Yagasaki, K. Kitamura, B. Mikami, et al. Crystal structure of soybean 11S globulin: glycinin A3B4 homohexamer. Proceedings of the National Academy of Sciences, 100 (2003) 7395.

[77] Y. Moon, C. Anderson, H. Blanch, and J. Prausnitz. Osmotic pressures and second virial coefficients for aqueous saline solutions of lysozyme. Fluid Phase Equilib., 168 (2000) 229.

[78] T. Ahamed, M. Ottens, G.W.K. van Dedem, and L.A.M. van der Wielen. Design of self-interaction chromatography as an analytical tool for predicting protein phase behavior. Journal of Chromatography A, 1089 (2005) 111.

[79] M. Placidi, S. Cannistraro. A dynamic light scattering study on mutual diffusion coefficient of BSA in concentrated aqueous solutions. Europhys.Lett., 43 (1998) 476.

[80] S. Saksena, A.L. Zydney. Influence of protein-protein interactions on bulk mass transport during ultrafiltration. J.Membr.Sci., 125 (1997) 93.

[81] W.R. Bowen, Y. Liang, and P.M. Williams. Gradient diffusion coefficients-theory and experiment. Chemical Engineering Science, 55 (2000) 2359.

[82] R. Parsons. The electrical double layer: recent experimental and theoretical developments. Chem.Rev., 90 (1990) 813.

[83] K.B. Oldham. A Gouy-Chapman-Stern model of the double layer at a (metal)/(ionic liquid) interface. J Electroanal Chem, 613 (2008) 131.

[84] C.M.A. Brett, Electrochemistry : principles, methods, and applications, Oxford ; New York, Oxford ; New York : Oxford University Press, 1993.

[85] R.J. Hunter, Foundations of colloid science, Oxford ; New York, Oxford ; New York : Oxford University Press, 2001.

[86] B. Chu, Molecular forces; based on the Baker lectures of Peter J. W. Debye, New York, Interscience Publishers, 1967, New York, Interscience Publishers, 1967.

[87] J.O.(. Bockris, Modern electrochemistry, New York, New York : Plenum Press, 2000.

[88] P.M. Biesheuvel. Implications of the charge regulation model for the interaction of hydrophilic surfaces in water. Langmuir, 17 (2001) 3553.

[89] W.B.S. de Lint, P.M. Biesheuvel, and H. Verweij. Application of the Charge Regulation Model to Transport of Ions through Hydrophilic Membranes: One-Dimensional Transport Model for Narrow Pores (Nanofiltration). J.Colloid Interface Sci., 251 (2002) 131.

[90] D.B. Hough, L.R. White. Calculation of Hamaker Constants From Lifshitz Theory With Applications To Wetting Phenomena. Adv.Colloid Interface Sci., 14 (1980) 3.

[91] W.R. Bowen, F. Jenner. The calculation of dispersion forces for engineering applications. Adv.Colloid Interface Sci., 56 (1995) 201.

[92] S. Nir. Van der Waals interactions between surfaces of biological interest. Prog Surf Sci, 8 (1977) 1.

[93] A. Grabbe, R.G. Horn. Double-layer and hydration forces measured between silica sheets subjected to various surface treatments. J.Colloid Interface Sci., 157 (1993) 375.

[94] K.R. Hall. Another hard-sphere equation of state. J.Chem.Phys., 57 (1972) 2252.

[95] J. Kolafa, S. Labík, and A. Malijevský. Accurate equation of state of the hard sphere fluid in stable and metastable regions. Physical Chemistry Chemical Physics, 6 (2004) 2335.

[96] R.L. Harvey, Neural network principles, Englewood Cliffs, NJ, Prentice Hall, 1994.

[97] G. Scatchard, E.S. Black. The Effect of Salts on the Isoionic and Isoelectric Points of Proteins. J.Phys.Chem., 53 (1949) 88.

[98] G. Scatchard, I.H. Scheinberg, and S.H. Armstrong. Physical Chemistry of Protein Solutions. IV. The Combination of Human Serum Albumin with Chloride Ion1. J.Am.Chem.Soc., 72 (1950) 535.

[99] H. Shen, D.D. Frey. Charge regulation in protein ion-exchange chromatography: Development and experimental evaluation of a theory based on hydrogen ion Donnan equilibrium. Journal of Chromatography A, 1034 (2004) 55.

[100] D. Mignard, D.H. Glass. Fouling during the cross-flow ultrafiltration of proteins: A mass-transfer model. J.Membr.Sci., 186 (2001) 133.

[101] G.D.J. Phillies, G.B. Benedek, and N.A. Mazer. Diffusion in protein solutions at high concentrations: A study by quasielastic light scattering spectroscopy. J.Chem.Phys., 65 (1976) 1883.

[102] D.B. Van, C.A. Smolders. Concentration polarization phenomena during dead-end ultrafiltration of protein mixtures. The influence of solute-solute interactions. J.Membr.Sci., 47 (1989) 1.

[103] S.R. Bellara, Z. Cui. A Maxwell-Stefan approach to modelling the cross-flow ultrafiltration of protein solutions in tubular membranes. Chemical Engineering Science, 53 (1998) 2153.

[104] A. Afonso, J.M. Miranda, and J.B.L.M. Campos. Numerical study of BSA ultrafiltration in the limiting flux regime — Effect of variable physical properties. Desalination, 249 (2009) 1139.

[105] M. Lund, B. Jönsson. A mesoscopic model for protein-protein interactions in solution. Biophys.J., 85 (2003) 2940.

[106] Y. Moon, R. Curtis, C. Anderson, H. Blanch, and J. Prausnitz. Protein—Protein Interactions in Aqueous Ammonium Sulfate Solutions. Lysozyme and Bovine Serum Albumin (BSA). Journal of Solution Chemistry, 29 (2000) 699.

[107] C. Berli, J. Deiber, and M. Anon. Connection between rheological parameters and colloidal interactions of a soy protein suspension. Food Hydrocoll., 13 (1999) 507.

[108] D. Petsev, V. Starov, and I. Ivanov. Concentrated dispersions of charged colloidal particles: sedimentation, ultrafiltration and diffusion. Colloids Surf.Physicochem.Eng.Aspects, 81 (1993) 65.

[109] A.S. Jönsson, B. Jönsson. Ultrafiltration of Colloidal Dispersions--A Theoretical Model of the Concentration Polarization Phenomena. J.Colloid Interface Sci., 180 (1996) 504.

[110] K.W.K. Yee, D.E. Wiley, and J. Bao. A unified model of the time dependence of flux decline for the long-term ultrafiltration of whey. Journal of Membrane Science, 332 (2009) 69.

[111] R. Juang, H. Chen, and Y. Chen. Resistance-in-series analysis in cross-flow ultrafiltration of fermentation broths of Bacillus subtilis culture. J.Membr.Sci., 323 (2008) 193.

[112] W. Richard Bowen, P.M. Williams. Prediction of the rate of cross-flow ultrafiltration of colloids with concentration-dependent diffusion coefficient and viscosity - theory and experiment. Chemical Engineering Science, 56 (2001) 3083.

[113] A.R. Rajabzadeh, C. Moresoli, and B. Marcos. Fouling Behavior of Electroacidified Soy Protein Extracts during Cross-Flow Ultrafiltration Using Dynamic Reversible-Irreversible Fouling Resistances and CFD Modeling. J.Membr.Sci., (2010).

[114] B.Bird, W. E. Stewart, E.N. Lightfoot R. Transport Phenomena, New York, Wiley, 2nd Edition, 2002

[115] John Happel. Viscous flow in multiparticle systems: Slow motion of fluids relative to beds of spherical particles. AIChE Journal, 4 (1958) 197.

[116] J. Nikolova, M. Islam. Contribution of adsorbed layer resistance to the flux-decline in an ultrafiltration process. J.Membr.Sci., 146 (1998) 105.

[117] A. A. Kozinski, E. N. Lightfoot. Protein ultrafiltration: A general example of boundary layer filtration. AIChE Journal, 18 (2004) 1030.

[118] A.L. Ahmad, M.F. Chong, and S. Bhatia. Ultrafiltration modeling of multiple solutes system for continuous cross-flow process. Chemical Engineering Science, 61 (2006) 5057.

[119] E.M.V. Hoek, S. Kim, M. Marion, and Byeong-Heon Jeong. Crossflow membrane filtration of interacting nanoparticle suspensions. J.Membr.Sci., 284 (2006) 361.

[120] L. Ricq, A. Pierre, S. Bayle, and J. Reggiani. Electrokinetic characterization of polyethersulfone UF membranes. Desalination, 109 (1997) 253.

[121] E. Iritani, S. Tachi, and T. Murase. Influence of protein adsorption on flow resistance of microfiltration membrane. Colloids Surf.Physicochem.Eng.Aspects, 89 (1994) 15.

[122] E. Iritani, T. Watanabe, and T. Murase. Effects of pH and solvent density on dead-end upward ultrafiltration. J.Membr.Sci., 69 (1992) 87.

[123] D. Mockel, E. Staude, and M.D. Guiver. Static protein adsorption, ultrafiltration behavior and cleanability of hydrophilized polysulfone membranes. J.Membr.Sci., 158 (1999) 63.

[124] H. Reihanian, C.R. Robertson, and A.S. Michaels. Mechanisms of Polarization and Fouling of Ultrafiltration Membranes by Proteins. J.Membr.Sci., 16 (1982) 237.

[125] W.R. Bowen, D.T. Hughes. Properties of microfiltration membranes. Part 2. Adsorption of bovine serum albumin at aluminium oxide membranes. J.Membr.Sci., 51 (1990) 189.

[126] A.G. Fane, C.J.D. Fell, and A. Suki. Effect of pH And Ionic Environment on The Ultrafiltration of Protein Solutions with Retentive Membranes. J.Membr.Sci., 16 (1982) 195.

[127] W.M. Clark, A. Bansal, M. Sontakke, and Y.H. Ma. Protein adsorption and fouling in ceramic ultrafiltration membranes. J.Membr.Sci., 55 (1991) 21.

[128] S. Salgin, S. Takac, and T.H. Ozdamar. Adsorption of bovine serum albumin on polyether sulfone ultrafiltration membranes: Determination of interfacial interaction energy and effective diffusion coefficient. J.Membr.Sci., 278 (2006) 251.

[129] S. Salgin, S. Takac, and T.H. Ozdamar. A parametric study on protein-membrane-ionic environment interactions for membrane fouling. Sep.Sci.Technol., 40 (2005) 1191.

[130] N. Muramatsu, T. Kondo. Adsorption of bovine serum albumin on positively and negatively charged microcapsules. J.Colloid Interface Sci., 153 (1992) 23.

[131] M.N. De Pinho, V. Semiao, and V. Geraldes. Integrated modeling of transport processes in fluid/nanofiltration membrane systems. J.Membr.Sci., 206 (2002) 189.

[132] D. Bhattacharyya, S.L. Back, R.I. Kermode, and M.C. Roco. Prediction of concentration polarization and flux behavior in reverse osmosis by numerical analysis. J.Membr.Sci., 48 (1990) 231.

Appendices

A.1. Rinsing method for ultrafiltration hollow fiber membrane (after storage in 30 % Ethanol)

1. Recirculate clean water in "total recycle" for 5 min at ~ 2.4 L/min (with manual pinch valve fully open).
2. Drain solution.
3. Repeat steps 1 & 2 two more times.
4. Recirculate 100 ppm NaClO (~ 50 ºC / 2.8 mL Javex in 700 mL) for ~30 min in "total recycle" at 1.2 L/min, with 5 psi outlet pressure.
5. After the ~30 min of cleaning, start cooling the system by placing the flask with the NaClO solution into a water bath. The temperature change should be gradual (1ºC/min). Keep adding ice into the water bath until the temperature in the flask with the NaClO solution reaches the room temperature (25 ºC).
6. Drain solution.
7. Recirculate clean water in "total recycle" for 5 min at 2.4 L/min, with 5 psi outlet pressure.
8. Drain solution.
9. Repeat steps 7 & 8 two more times.
10. Flush both the retentate and the permeate side in a non-circulating mode by setting the flow rate to 1.2 L/min and the TMP to 20 psi (i.e. both the retentate and the permeate line are drained).
11. Remove any bubbles from the permeate side. Start the pump at low flow rate (1.2 L/min). Close the permeate side slowly. Then start closing the manual pinch valve on the retentate line until the TMP is 20 psi (max!). Keep the pressure for ~ 5 min and then open slowly the permeate side (bubbles should be coming out at this point).
12. Measure the water flux (follow section A.2.).

A.2. Membrane resistance estimation procedure (water flux measurement)

1. Circulate nano-pure water in a recycle mode (retentate is returned to the feed tank).
2. Set flow rate to 2.2 L/min.
3. Keep feed solution at a constant temperature of 25ºC.
4. Measure 1-3 grams of permeate over a measured amount of time (g/s) at the lowest possible TMP.
5. Using the valve on the retentate line, increase TMP and repeat step 4. Measure permeate rate (g/s) at six different TMP (TMP is varied from 2-17 psi).
6. Divide the permeate rate (g/s) by the membrane surface area and solution density to calculate permeate velocity (v_w).
7. Plot permeate velocity versus TMP.
8. Membrane resistance (R_m) is calculated by multiplying the slope of the permeate velocity *vs.* TMP curve by the solution viscosity.
9. $$v_w = \frac{TMP}{\mu \cdot R_m}$$

Sample calculation:

$$\text{Flow Rate} = m_{permeate}/t$$
$$= 1g/4.13s$$
$$= 0.24g/s$$
$$= 2.4\times10^{-4} kg/s$$

$$v_w = (2.4\times10^{-4}\frac{kg}{s}) \times (\frac{m^3}{1000kg}) \times (\frac{1}{0.0418\,m^2}) = 5.74\times10^{-6} \text{ m/s}$$

Membrane resistance for one data point can be estimated

$$R_m = \frac{TMP}{\mu \cdot v_w} = \frac{18961\,Pa}{(8.91\times10^{-4}\,Pa.s)(5.74\times10^{-6}\,m/s)} = 3.71\times10^{12}\ m^{-1}$$

See next page for another sample calculation

	TMP	TMP (pa)	Perm mass (g)	Time (s)	Flow Rate (mL/min)	Flow rate (m^3/s)	Flow rate (kg/s)	Permeate Flux (kg/m^2s)	Permeate flux (LMH-l/m^2h)	Rm (m^2/kg)	Rm (m^{-1})
1	3.19	21994	1	1.85	32.526	5.421E-07	5.405E-04	1.293E-02	46.681	1.91E+09	1.90E+12
2	3.16	21787	1	2.00	30.086	5.014E-07	5.000E-04	1.196E-02	43.180	2.04E+09	2.04E+12
3	3.11	21443	1	1.91	31.504	5.251E-07	5.236E-04	1.252E-02	45.214	1.92E+09	1.92E+12
4	3.08	21236	1	1.85	32.526	5.421E-07	5.405E-04	1.293E-02	46.681	1.84E+09	1.84E+12
5	5.25	36197	1	1.00	60.173	1.003E-06	1.000E-03	2.392E-02	86.359	1.70E+09	1.69E+12
6	5.24	36129	1	1.13	53.250	8.875E-07	8.850E-04	2.117E-02	76.424	1.92E+09	1.91E+12
7	5.27	36335	1	1.04	57.858	9.643E-07	9.615E-04	2.300E-02	83.038	1.77E+09	1.77E+12
8	6.78	46746	1	0.82	73.381	1.223E-06	1.220E-03	2.917E-02	105.316	1.80E+09	1.79E+12
9	7.04	48539	1	0.82	73.381	1.223E-06	1.220E-03	2.917E-02	105.316	1.87E+09	1.86E+12
10	6.91	47643	1	0.78	77.144	1.286E-06	1.282E-03	3.067E-02	110.717	1.74E+09	1.74E+12
11	10.03	69154	2	1.09	110.409	1.840E-06	1.835E-03	4.389E-02	158.457	1.77E+09	1.76E+12
12	9.97	68741	2	1.07	112.472	1.875E-06	1.869E-03	4.471E-02	161.419	1.73E+09	1.72E+12
13	10.13	69844	2	1.13	106.500	1.775E-06	1.770E-03	4.234E-02	152.848	1.85E+09	1.85E+12
14	12.90	88942	5	2.22	135.524	2.259E-06	2.252E-03	5.387E-02	194.503	1.85E+09	1.85E+12
15	13.03	89839	5	2.37	126.947	2.116E-06	2.110E-03	5.046E-02	182.192	2.00E+09	1.99E+12
16	12.90	88942	5	2.19	137.381	2.290E-06	2.283E-03	5.461E-02	197.167	1.83E+09	1.82E+12
17	17.80	1E+05	5	1.53	196.643	3.277E-06	3.268E-03	7.817E-02	282.219	1.76E+09	1.76E+12
18	17.92	1E+05	5	1.57	191.633	3.194E-06	3.185E-03	7.618E-02	275.029	1.82E+09	1.82E+12
19	17.90	1E+05	5	1.69	178.026	2.967E-06	2.959E-03	7.077E-02	255.500	1.96E+09	1.95E+12

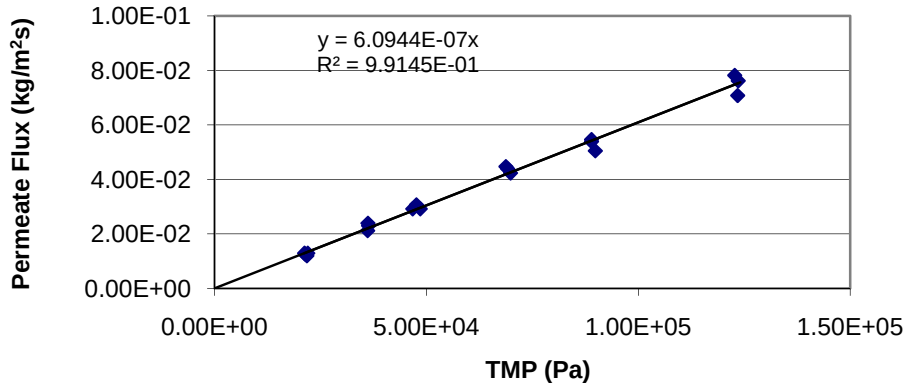

Slope	6.094E-07
Rm (m^{-1})	**1.836E+12**

A.3. Initial resistance estimation procedure of soy protein ultrafiltration

1. Circulate nano-pure water in the filtration system (retentate is returned to the feed tank); adjust TMP and feed flow rate to desired operating conditions. Make sure no bubble exists in the membrane module.
2. Without stopping filtration, switch feed solution from water to soy protein using a valve installed on the feed line. The whole experiment fails when bubbles are observed in the membrane module during filtration.
3. Readjust TMP and feed flow rate.
4. Keep feed solution at a constant temperature of 25º*C*.
5. Measure 1-3 grams of permeate over a measured amount of time (g/s) after 2 minutes.
6. Stop filtration after 2 minutes.
7. Similar to A.2 calculate permeate velocity.
8. Estimate global fouling resistance using

   $$v_w = \frac{TMP}{\mu^0 . R_G}$$

   Global fouling resistance, R_G, consists of membrane resistance, reversible fouling resistance (water removal) and irreversible fouling resistance (chemical removal).

   $$R_G = R_m + R_R + R_I$$
9. Estimate reversible and irreversible fouling (follow section A.5.)
10. Clean the membrane (chemical wash).

A.4. Soy protein ultrafiltration concentration procedure

1. Pump soy protein feed solution through the system at low flow rate (~ 1.2 L/min) with the retentate line in a beaker to collect the system holdup (~ 200 mL). Permeate line in beaker on a scale to measure the permeate flux.
2. Set TMP and feed flow rate to desired operating conditions.
3. Keep feed solution at a constant temperature of 25ºC.
4. Record permeate mass with time (Labview 7.1 data acquisition system).
5. Take a sample (~2.5 mL) every 15 min of operation to measure protein concentration.
6. Stop filtration at around VCR 4.
7. Calculate global fouling resistance similar to A.3 (step 8).
8. Estimate reversible and irreversible fouling (follow section A.5.)
9. Clean the membrane (chemical wash).

A.5. Estimation of reversible/irreversible fouling

1. Flush the fouled membrane in a non-circulating mode with 1L of clean water at TMP and flow rate at which the prior experiment has been run.

   Note: To avoid bubbles, do not drain the membrane module at any step. Bubbles in the module affect the membrane fouling. The whole experiment fails when bubbles are observed in membrane module during filtration or washing.
2. Recirculate additional 1L of clean water in "total recycle" for 5 min.
3. Perform the water flux (follow section A.2.) to estimate the summation resistances of the irreversible fouling and the membrane.

$$v_w = \frac{TMP}{\mu^0.(R_m + R_I)}$$

4. Irreversible fouling resistance, R_I, can be calculated with the known value of membrane resistance calculated in A.2. (water flux measurement before the filtration).
5. Reversible fouling resistance, R_R, is calculated by subtracting the irreversible fouling resistance (R_I) and the membrane resistance (R_m) from the global fouling resistance calculated in section A.3 (step 8) or A.4 (step 7).

A.6. Soy protein solution preparation:

1. Prepare feed solution at 2 (w/w) % (for 1.7 L weigh 34 g of SPE and 1666 mL of nano-pure water.
2. Rehydrate for 1h at ~ 300-600 rpm (2-liter beaker with a 1 inch magnetic stirrer).
3. In the meantime, measure water flux of the clean membrane (follow section A.2) at a constant temperature of 25 ºC.
4. After 1 h of rehydration, centrifuge feed solution (250 ml tube) at 10000 rpm for 17 min at 23˚C (Beckman Coulter L7-35 ultracentrifuge (Mississauga, ON, Canada)).
5. Take samples of supernatant (3x15 mL centrifuge tubes if possible and at least 2.5 mL to estimate total solid (optional) and protein concentration.
6. Measure pH and conductivity of feed solution.
7. Weigh feed solution before filtration start.

A.7. BSA ultrafiltration in a total recycle mode

1. Perform water flux before protein solution filtration to estimate membrane resistance (follow section A.2).
2. Pump BSA feed solution through the system at low flow rate (~ 1.2 L/min) with the retentate line in a beaker to collect the system holdup (~ 200 mL).
3. Set TMP and feed flow rate to desired operating conditions.
4. Keep feed solution at a constant temperature of 25ºC.
5. Measure 1-3 grams of permeate over a measured amount of time (g/s) after 10 minutes filtration at the lowest possible TMP.
6. Increase TMP using the valve on the retentate line, wait for 10 minutes and repeat step 5.
7. Repeat last step (step 6) 4 more times. Measure permeate rate (g/s) at five different TMP (TMP is varied from 2-17 psi).
8. Plot permeate velocity versus TMP (similar to A.2).
9. Estimate global fouling resistance at each TMP.
10. Follow A.5 to estimate the reversible and irreversible fouling
11. Clean the membrane (chemical wash).

A.8. Cleaning procedure (chemical wash) for UF hollow fiber membrane (after experiment)

1. Recirculate clean warm water (50-60 ºC / ~700 mL) for 10 min in "total recycle" at 2.4 L/min, with 5 psi outlet pressure.
2. Drain solution.
3. Recirculate 0.2 % Tergazyme (50-60 ºC / 1.4 g in 700 mL) for 30-60 min in "total recycle" at 1.2 L/min, with 5 psi outlet pressure.
4. Drain solution.
5. Flush membrane in a non-circulating mode (flush/rinse water is withdrawn from the system, i.e. retentate line drained) with ~ 500 mL of clean warm water (50-60 ºC). Keep 1.2 L/min flow rate and 5 psi outlet pressure.
6. Continue rinsing in "total recycle" with additional ~ 500 mL of clean warm water (50-60 ºC).
7. Drain solution.
8. Recirculate 100 ppm NaClO (50-60 ºC / 2.8 Javex in 700 mL) for 30-60 min in "total recycle" at 1.2 L/min, with 5 psi outlet pressure.
9. After 30-60 min of cleaning, start cooling the system by placing the flask with the NaClO solution into a water bath. The temperature change should be gradual (1ºC/min). Keep adding ice into the water bath until the temperature in the flask with the NaClO solution reaches the room temperature (25 ºC).
10. Drain solution.
11. Recirculate clean water in "total recycle" for 5 min at 2.4 L/min, with 5 psi outlet pressure.
12. Drain solution.
13. Repeat steps 9 & 10 two more times.
14. Flush both the retentate and the permeate side in a no-circulating mode by setting the flow rate to 1.2 L/min and the TMP to 20 psi (i.e. both the retentate and the permeate line are drained).
15. Measure the water flux (follow section A.2).
16. Repeat steps 1-15 if membrane resistance obtained in step 15 is different by more than ±10% of the membrane resistance before protein filtration.

A.9. Summary of experimental operating conditions

	Initial fouling resistance estimation (section 3.3.3)	Soy protein ultrafiltration (section 3.3.4)	BSA ultrafiltration (section 5.3)
Filtration mode	Concentration operation	Concentration operation	Total recycle
TMP (kpa)	27.5-55	27.5-41.5	15-112
Feed solution	Soy protein	Soy protein	BSA
pH	6 and 9	6 and 9	5-9
Ionic strength (M)	----------	----------	0.01-0.1
Initial protein concentration in the feed tank ($g.L^{-1}$)	10	10	5
Temperature	25°*C*	25°*C*	25°*C*
Axial velocity ($m.s^{-1}$)	1	1	1

A.10. Structure of the amino acid groups[2]

Amino acids with hydrophobic side groups

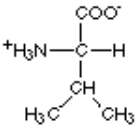

Valine
(val)

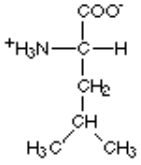

Leucine
(leu)

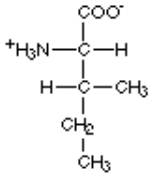

Isoleucine
(ile)

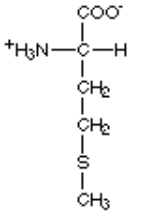

Methionine
(met)

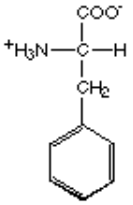

Phenylalanine
(phe)

Amino acids with hydrophilic side groups

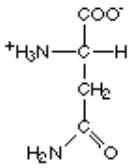

Asparagine
(asn)

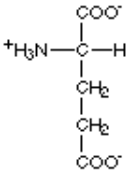

Glutamic acid
(glu)

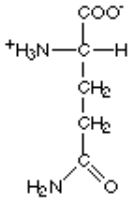

Glutamine
(gln)

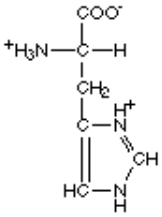

Histidine
(his)

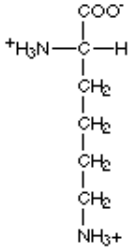

Lysine
(lys)

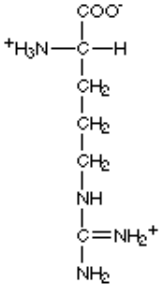

Arginine
(arg)

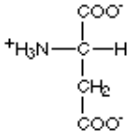

Aspartic acid
(asp)

Amino acids that are in between

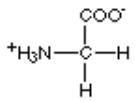

Glycine
(gly)

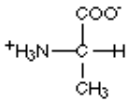

Alanine
(ala)

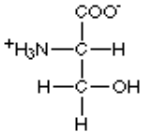

Serine
(ser)

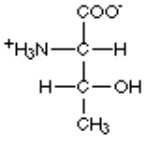

Threonine
(thr)

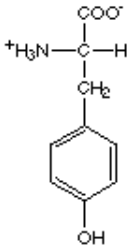

Tyrosine
(tyr)

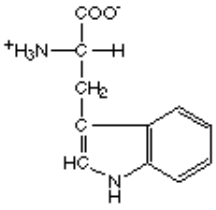

Tryptophan
(trp)

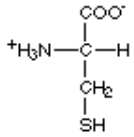

Cysteine
(cys)

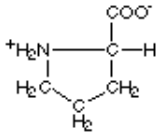

Proline
(pro)

[2] Adapted from http://www.mansfield.ohio-state.edu/~sabedon/biochem511.htm